

DISSERTATION ZUR ERLANGUNG DES DOKTORGRADES
DER FAKULTÄT FÜR CHEMIE UND PHARMAZIE
DER LUDWIG-MAXIMILIANS-UNIVERSITÄT MÜNCHEN

ORIENTED NANOCANNELS FOR NANOWIRE SYNTHESIS

vorgelegt von

ANDREAS KEILBACH

AUS

MÜNCHEN

2010

ERKLÄRUNG:

Diese Dissertation wurde im Sinne von §13 Abs. 3 der Promotionsordnung vom 29. Januar 1998 von Herrn Prof. Dr. Thomas Bein betreut.

EHRENWÖRTLICHE VERSICHERUNG:

Diese Arbeit wurde selbstständig und ohne unerlaubte Hilfe erarbeitet.

Ort, Datum

Unterschrift

Datum der Einreichung: 07. Mai 2010

1. Gutachter: Prof. Dr. Thomas Bein

2. Gutachter: Prof. Dr. Christina Scheu

Tag der mündlichen Prüfung: 10. Juni 2010

DANKSAGUNG.

Vor allen Dingen möchte ich mich bei meinem Doktorvater **Prof. Thomas Bein** bedanken. Ohne seine großzügige finanzielle Unterstützung, die vielen interessanten Diskussionen und das Vertrauen in meine Arbeit wäre diese Arbeit nicht möglich gewesen.

Bei **Prof. Tina Scheu** möchte ich mich herzlich für die Übernahme des Zweitgutachtens bedanken.

Ich möchte mich bei **Dr. Anna Fontcuberta i Morral** und **Dr. Ying Xiang** für die erfolgreiche Zusammenarbeit in dem Projekt 'Multiple Nanowire Species Synthesized on a Single Chip' sowie den Einblick in das CVD Wachstum von Nanodrähten danken. Bei Ying möchte ich mich weiterhin auch noch für die Unterstützung beim Setup des des Anodisierungsprozesses bedanken.

Ein ganz besonderer Dank gilt natürlich auch **Dr. Ralf Köhn**, dessen aufopfernde Betreuungsarbeit schon mit meiner Diplomarbeit begann und dessen Rat mir bis heute sehr wichtig ist. Mindestens genauso wie für seine wissenschaftliche Betreuung möchte ich mich bei ihm aber auch noch für die vielen Stammtische, Fussballabende und Weißwurstfrühstücke bedanken.

Bedanken möchte ich mich natürlich auch noch natürlich bei **Markus** für seine Hilfe an den Mikroskopen und bei der Interpretation unmöglicher Beugungsbilder und auch bei **Steffen** für die viele Zeit an SEM, TEM und FIB. Danke an **Regina** (dafür, dass sie Ordnung in das manchmal riesige Verwaltungschaos bringt), **Tina** (dafür, dass sie Ordnung in unser ebenso großes Laborchaos bringt), bei **Mirjam**,

Axel, Jörg und allen anderen, die den manchmal aufkommenden Laborfrust ganz schnell wieder verfliegen lassen. Ein Dank auch an meine ehemalige Bürokollegin **Camilla** für ihre Motivation und die reibungslose Übergabe des AMS. Bei **Yan** bedanke ich mich dafür, dass sie mein Thema mit großem Einsatz weiterführt. Danke auch an alle meine Praktikanten **James, Hans, Eva, Rainer, Susanne** und **Cate** für ihre großartige Unterstützung meiner Forschung. Natürlich gilt mein Dank aber auch all den hier aus Platzgründen nicht erwähnten Mitarbeitern, Diplomanden und Studenten des ganzen **AK Bein**, die mein Leben nicht nur wissenschaftlich sondern mit den unzähligen Kaffeepausen, Stammtischen, Grillabenden etc. ganz klar auch jenseits der Wissenschaft bereichert haben.

Der größte Dank geht am Ende aber natürlich an **Huihong** und **meine Familie**, ohne deren fortwährende Unterstützung ich nicht das wäre, was ich heute bin.

ABSTRACT.

This thesis aims at the synthesis of oriented nanochannel systems for the synthesis of metallic or semiconducting nanowires. Three different synthesis strategies have been developed.

First, horizontal macro- to mesoporous anodic aluminum oxide (AAO) structures with individually addressable channel systems were fabricated in collaboration with the group of Dr. Anna Fontcuberta at TU München. For this purpose, a multi-contact design of aluminum finger structures on silicon wafers was developed. Each finger structure can be individually contacted and between 2 - 5 contacts were generated on a single silicon wafer. The aluminum contacts were electrically isolated from each other, thus each contact can be individually anodized. This way it is possible to synthesize different pore diameters, pore densities, and channel lengths on a single chip. After the anodization, these channels were successfully filled by electro-deposition and thermal chemical vapor deposition. The resulting metal (Au, Cu, Ni, Co) and semiconductor (Te, Si) nanowires embedded within the AAO mold were characterized by SEM and EDX measurements.

The second strategy deals with hierarchical channel structures formed from columnar silica mesophases inside AAO membranes. These channels were then used for the fabrication of high-aspect ratio copper, silver, and tellurium nanowires. The resulting wires were structurally and spectroscopically characterized within the host matrix, in the partially dissolved matrix, and completely removed from the matrix

with electron microscopy methods. Plan-view images of wires featuring 10 nm diameter within the intact matrix showed the successful replication of the hexagonal arrangement of the columnar mesoporous system.

The concept of hierarchical structures within PAA templates was again utilized for the third strategy, where the structural behavior of periodic mesoporous organosilica (PMO) mesophases within the AAO pores was studied. PMO mesophases with different orientations with respect to the alumina pores were obtained; one of the observed mesophases (cubic $Im\bar{3}m$) has not been reported before. After successful template removal, the hexagonal circular mesophase could be used for the synthesis of nanowires by electrodeposition.

Contents

1	Nanotechnology & Nanomaterials	1
2	Introduction to Nanoporous Materials	7
2.1	Introduction	7
2.2	Porous Anodic Alumina	9
2.2.1	Barrier-type and porous-type anodization of aluminum	10
2.2.2	Synthesis of PAA	11
2.2.3	Applications of anodic alumina	17
2.3	Mesoporous structures in confined environments	19
2.3.1	Introduction to periodic mesoporous materials	19
2.3.2	Synthesis of mesostructures within AAO membranes	26
2.3.2.1	Sol-gel processes	28
2.3.2.2	Synthesis <i>via</i> EISA	33
2.3.2.3	Vapor-phase synthesis	46
2.3.3	PMO and carbon mesophases	48
2.3.4	Inclusion chemistry	59

2.3.5	Separation/release	63
2.3.6	Summary	70
3	One-dimensional Nanostructures	73
3.1	Introduction	73
3.2	Nanowire synthesis	74
3.2.1	Spontaneous growth	75
3.2.2	Template-based synthesis	80
3.2.3	Electrospinning and lithography	84
3.3	General Properties of Nanowires	85
4	Characterization of Nanomaterials	89
4.1	Introduction	90
4.2	X-Ray diffraction (XRD)	90
4.2.1	Small angle X-ray scattering	91
4.2.2	Wide angle XRD	95
4.3	Electron microscopy	96
4.3.1	Scanning electron microscopy	97
4.3.2	Transmission electron microscopy	98
4.3.3	Elemental analysis	101
4.4	Sorption measurements	102
4.5	Other characterization techniques	107
4.5.1	Infrared and Raman Spectroscopy	107
4.5.2	Thermogravimetric analysis	107
4.5.3	Nuclear magnetic resonance	108

5	Multiple Nanowire Species Synthesized on a Single Chip by Selectively Addressable Horizontal Nanochannels	111
5.1	Introduction	111
5.2	Experimental	114
5.3	Results and discussion	117
5.4	Conclusion	125
6	Synthesis of Nanowires by Electrodeposition within Columnar Silica/Alumina Composites	127
6.1	Introduction	128
6.2	Experimental	131
6.3	Results and discussion	133
6.3.1	Optimization of the composite membrane synthesis	133
6.3.2	Influence of the electrolyte concentration and the deposition potential	135
6.3.3	Plan view TEM micrographs	136
6.3.4	TEM of filaments	139
6.3.5	TEM of free standing wires	143
6.4	Conclusion	147
6.5	Outlook	148
7	Periodic Mesoporous Organosilicas in Confined Environments	157
7.1	Introduction	158
7.2	Experimental	160
7.3	Results and discussion	162
7.3.1	CTAB-template	162

7.3.2	Brij 56-template	163
7.3.3	Removal of the template	166
7.3.4	Replication of the porous system	169
7.3.5	Additional details	171
7.4	Conclusions and perspectives	177
8	General Conclusions	179
9	Bibliography	183
	Appendices	205
	List of abbreviations	207
	Curriculum vitae	209
	List of publications and presentations	210
	Publications	210
	Oral presentations	211
	Poster presentations	212

Introduction to Nanotechnology & Nanomaterials

The use and manufacture of materials with critical sizes at the nanometer scale can already be traced back for centuries. Gold nanoparticles have been used by the Chinese to color ceramics already over 1000 years ago.^[1] Faraday described the preparation of colloidal gold solutions in 1857. Colloidal gold solutions were – and are – used for the treatment of arthritis.^[2] There are many other examples; but even if nanoscale materials are not really “new”, what is new is that we are now able to see, manipulate, and – at least partially – understand materials on the nanometer scale.

In 1959, Richard Feynman gave the famous lecture titled “There’s plenty of room at the bottom”.^[3] At a time when most scientist were focused on the science at the very large scale, such as astrophysics, he gave a vision of extreme miniaturization years before the first computer chip was developed. By addressing the problems of manipulating and controlling matter on the extremely small scale, he encouraged scientists all over the world to start thinking for solutions of the tremendous challenges. Since then, progress a lot of progress has been made; in fact, nowadays the word “nano” became a buzzword of the modern age. The prefix ‘nano’ can be

found in paints, which contain very small pigments; clothes, into which nanoparticles are incorporated to protect them from dirt; and of course, the modern computer age would not be possible without highly integrated circuits at the nanometer scale, assembled on a chip.

The prefix “nano” is derived from the greek word “nanos” meaning “dwarf”. In the metric system it is used to denote a factor of 10^{-9} (0.000 000 001). Thus, one nanometer equals one billionth of a meter. Looking at this scale from an atom’s point of view, 1 nm equals the distance of, e. g., about 5 silicon atoms in a row.

While materials sized 1 μm and above usually exhibit properties of the bulk material, materials with sizes on the nanometer scale might have distinctively different properties than their bulk form. The number of atoms located on the surface of a crystal becomes a significant fraction of the total number of atoms. As the surface energy is significant for the thermal stability of crystals, nano-sized crystals can have dramatically lower melting points than the bulk material (with melting point differences as large as 1000 °C) and reduced lattice constants.^[2] Materials with semiconducting properties in their bulk form might become insulating when being synthesized on the nanometer scale. Nano-sized gold droplets show excellent low-temperature catalytic properties not known from bulk gold.

There is general agreement that the term “nanotechnology” was introduced by Norio Taniguchi at a meeting of the Japan Society of Precision Engineering in 1974:^[4-6]

“Nano-technology mainly consists of the processing, separation, consolidation, and deformation of materials by one atom or by one molecule.”

Nowadays, the term nanotechnology has been slightly expanded and generally means any technology performed on a nanoscale that has applications in the real

world. Thereby it encompasses the production and application of physical, chemical, and biological systems at scales ranging from individual atoms or molecules to submicrometer dimensions, as well as the integration of the resulting nanostructures into larger systems.^[7] Because of this very general terminology, many people working in nanotechnology are using this term to define their field of research. Some people consider a bottom up approach in materials synthesis, such as biomineralization of mussel shells or the self-assembly of molecules as nanotechnology. Others claim that the study of microstructures by electron microscopy is nanotechnology. Lab-on-a-chip design and synthesis is also considered as nanotechnology. There are many other examples; they all reflect the fact that nanotechnology covers a broad spectrum of research areas and that is a highly interdisciplinary field of science.^[2]

Over the recent years two main strategies – “top-down” and “bottom-up” – have been established for the manufacture of nanostructures (Figure 1.1). Both strategies have their own advantages and disadvantages.

As implied by the name, top-down strategies seek to assemble small, nanoscopic structures by directing larger ones. It has its foundations in solid-state physics and the methods used have their source in classical microsystems technology. Techniques such as photolithography, ion milling, and others are used to shape materials into their desired form. It is extensively used in modern semiconductor fabrication. These methods have been constantly improving over the last decades; nevertheless, top-down approaches have limitations that become harder and harder to overcome. Among others, the imperfection of surfaces structures manufactured by top-down techniques are considered as a main drawback. Nanowires prepared by photolithography may suffer from crystallographic damage on their surface and

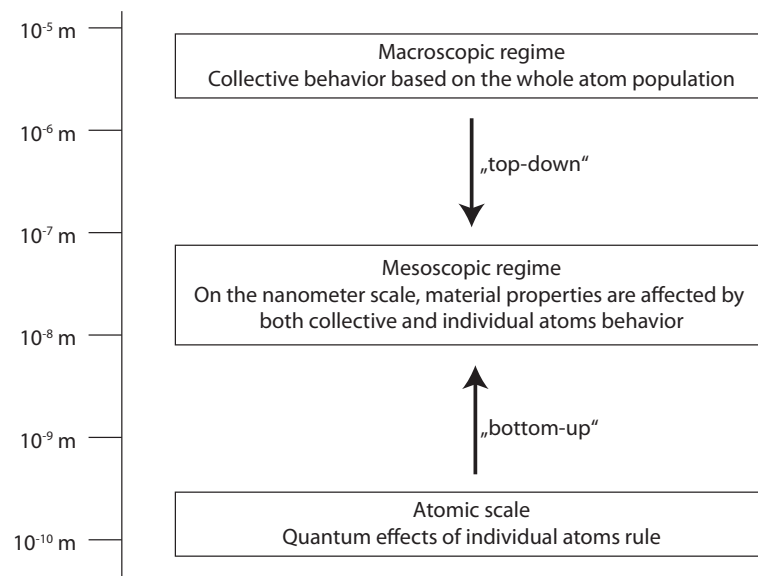


Figure 1.1 — Schematic representation of the principles of top-down and bottom-up approaches. In principle, the bottom-up approach could also be used to create macroscopic objects. Figure adapted from [8].

contain impurities.^[2] This can result in a reduced conductivity, leading to the generation of excessive heat that might cause further damage to either the wire itself or, even worse, to the whole device that is built around it.

Bottom-up approaches are somewhat opposite to top-down, as here the aim is to manufacture structures through the assembly of small building blocks (atoms, molecules) into larger structures. The bottom-up principle is nothing really new and has been used industrially since a long time. Polymers are synthesized from smaller monomers to form molecules of tremendous sizes; crystals grow by the arrangement of small growth species (atoms, ions, or clusters) on a growth surface. Still, bottom-up is playing an important role in the synthesis of nanostructures and nanomaterials. One of the drawbacks of top-down techniques, such as surface defects and contaminations, can be overcome by starting on the atomic or molecular level. This is possible because bottom-up processes are driven mainly by the reduc-

tion of the Gibbs free energy. That way, nanostructures and nanomaterials can be produced in a state that is very close to the thermodynamic equilibrium state.^[2]

Creating an arsenal of molecular and nanoscale devices by self-assembly is just the first step in the organization of components for e. g. nanoelectronics. Interconnecting and integrating these devices is likely to be even more challenging. To date, molecular switches or inorganic solids that can as transistors have been hooked to conventional wires created by lithography. In many cases, the molecular “glue” is represented by thiol-terminated organic molecules attached to gold electrodes forming self-assembled monolayers. Such strategies can be seen as a combination of both top-down and bottom up; the lithographic creation of the gold electrodes meets the self-assembly of molecules.

Nanomaterials are often categorized according to their dimensionality. Zero-dimensional (0-d) objects are dots; all kinds of spherically shaped nanoparticles – such as colloidal crystals or quantum dots – fall into this category. Nanowires and nanorods are one-dimensional nanoobjects. Thin films represent two-dimensionality. All other objects that cannot be easily grouped into one of these categories, such as micro- or mesoporous bulk materials, fullerenes, etc. would make up a special category.

Introduction to Nanoporous Materials

Contents

2.1	Introduction	7
2.2	Porous Anodic Alumina	9
2.2.1	Barrier-type and porous-type anodization of aluminum . . .	10
2.2.2	Synthesis of PAA	11
2.2.3	Applications of anodic alumina	17
2.3	Mesoporous structures in confined environments	19
2.3.1	Introduction to periodic mesoporous materials	19
2.3.2	Synthesis of mesostructures within AAO membranes	26
2.3.3	PMO and carbon mesophases	48
2.3.4	Inclusion chemistry	59
2.3.5	Separation/release	63
2.3.6	Summary	70

2.1 Introduction

Porous solids of all kinds are of high interest both from a scientific and technological point of view.^[9-12] Due to their porous nature, they can interact with atoms,

ions, and molecules not only on a limited external surface, but also on the far larger internal surface of their pore walls. Classical applications in fields such as adsorption, ion exchange and catalysis all take advantage of the large accessible surface area. Besides the large surface area, these solids can be synthesized with highly ordered pore systems, such as for example in classical zeolite materials. Nanoporous compounds are usually classified into three sub-classes according to their pore size (table 2.1).^[13] To perform the desired functions, the arrangement of the empty voids (geometry of the pore system, pore size distribution, pore volume) within the solid is a key factor. Materials with uniform pore sizes have the ability to separate molecules according to their size, thus narrow pore size distributions are usually desired.

Table 2.1 — Definitions of porous materials with respect to the pore size according to IUPAC.

Pore diameter	Pore type
$< 2 \text{ nm}$	Micropores
$2 \text{ nm} < \varnothing < 50 \text{ nm}$	Mesopores
$> 50 \text{ nm}$	Macropores

2.2 Porous Anodic Alumina

Anodic oxidation describes a process in which an electrochemically active species (in this case aluminum) is oxidized in an electric field using appropriate electrolytes. The process of aluminum anodization is already known for several decades; early reports date back as long as 1905.^[14] Anodic alumina films have widespread applications in modern industry, such as dielectrics in aluminum capacitors, keying layers for organic coatings and protection layers for aluminum substrates.^[15] Besides these commercial aspects there is great scientific interest in these materials for applications as filter membranes and as a template material for the synthesis of nanostructures.

During anodic oxidation of aluminum, the aluminum serves as the anode and a chemically stable metal such as platinum, copper etc. serves as the cathode. Possible electrolytes include phosphoric, chromic, oxalic, malonic, citric, and sulfuric acid. In general, aluminum can be anodized either using direct current (dc) or alternating current (ac). During ac anodization, only the anodic half-cycle is effective.^[16] The anodization is usually carried out at a constant temperature.

Aluminum anodization is widely used in industry both to increase corrosion resistance and to allow dyeing. When exposed to the atmosphere, aluminum forms a passive oxide layer which provides moderate protection against corrosion. In its pure form aluminum self-passivates very effectively, but its alloys are far more prone to atmospheric corrosion and therefore benefit from the protective quality of anodizing. Aluminum alloy parts are therefore anodized to increase the thickness of this oxide layer for corrosion resistance.

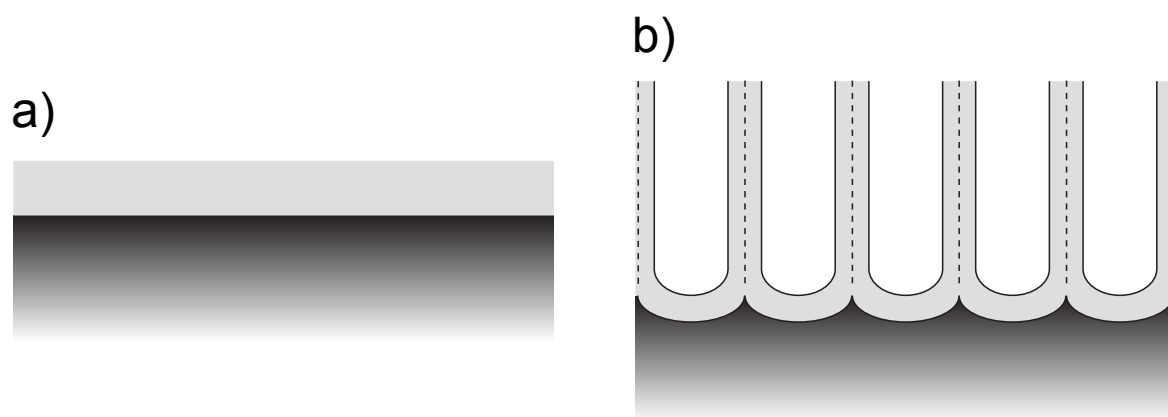


Figure 2.1 — Scheme illustrating a section of (a) barrier-type film and (b) porous-type film on aluminum; after [17]

2.2.1 Barrier-type and porous-type anodization of aluminum

The morphology, physical and structural properties of the anodic oxide films as well as the kinetics of the oxide growth depend on the applied voltage or current, temperature and most importantly, the type of the electrolyte. Generally, two types of alumina films, barrier-type and porous-type, can be obtained by anodization. A schematic depicting both types can be seen in Fig. 2.1.

“Barrier-type aluminas” are compact and dense oxides. Almost all of the electrochemically available aluminum is converted to alumina with – as general rule – no dissolution of the oxide formed. The thickness of the film is strongly dependent on the electric field applied during the anodization process. An average value of 1.3 nm/V was experimentally found as a growth ratio (also referred to as anodizing ratio).^[15,16,18] Thus, an anodization voltage of 100 V will produce a dense barrier-type film of 130 nm thickness. Commonly used electrolytes are boric acid, ammonium borate, and some organic electrolytes such as glycolic or maleic acid.

“Porous-type films” are formed in mild acidic or selected alkaline electrolytes, in which the oxide is slightly soluble. As already implied by the name, the formed films have a porous structure with pore diameters in the range of approximately 10 nm to 400 nm. The thickness of the porous layer is dependent on the anodization time, current density, electric field and temperature. The achievable film thickness is mainly limited by the solubility of the oxide in the respective electrolyte; porous alumina can be grown to 100 μm thickness and higher. Commonly used electrolytes are aqueous solutions of sulfuric acid, oxalic acid, and phosphoric acid. Porous anodic alumina (PAA) or anodic aluminum oxide (AAO) is widely used in industry due to various properties. It shows excellent corrosion and abrasion resistance after sealing the pore system; hence it can be used as a protection layer for metal surfaces. By filling the pores with dyes highly decorative metallic surfaces can be produced. Furthermore, due to the porous nature of this material, research labs all over the world use PAA as a template material for the synthesis of various nanostructures.^[19–21]

2.2.2 Synthesis of porous anodic alumina

Porous anodic alumina can be synthesized either by Faraday oxidation or plasma-chemical oxidation of aluminum surfaces.^[16] While the latter one is feasible for a number of elements (Al, Si, Ti, and others), it always produces highly irregular porous structures. In comparison, highly ordered, regular structures can be obtained by electrochemical Faradaic oxidation of aluminum. In this work, only AAO structures made by electrochemical oxidation have been used; hence the plasma-chemical oxidation will not be further discussed in this introduction.

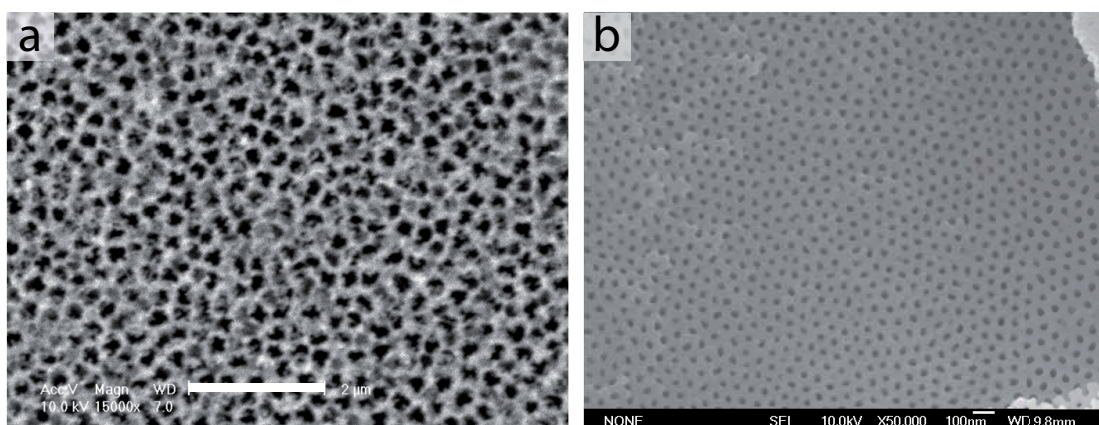
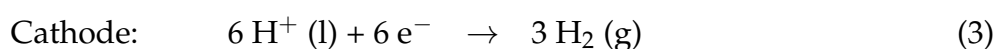
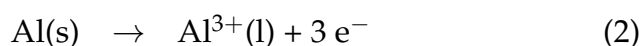
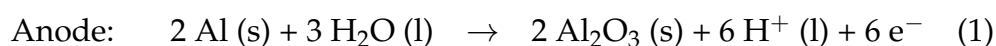


Figure 2.2 — SEM micrographs of porous anodic alumina films. a) Commercial membrane (Whatman Anodisc, nominal pore diameter 0.2 μm). The scale-bar of the image is 2 μm . b) PAA film anodized in the laboratory using aqueous H_2SO_4 as the electrolyte for the anodization. The pore size is about 30 nm.

Because of the high affinity between aluminum and oxygen, aluminum surfaces are always covered with a thin, native layer of aluminum oxide when exposed to oxygen-containing atmospheres or solutions. The thickness of this layer is approximately 15 nm. It can easily be removed by washing the aluminum substrates with alkaline solutions such as sodium hydroxide.

The voltages and current densities used for electrochemical anodization have to be in a range at which no discharging or burning occurs. The overall electrochemical reactions that occur during electrochemical oxidation of aluminum can be written as follows:



For porous alumina films, a combination of reaction (1) and (2) occurs and their individual rates are given by the electrode kinetics, the pH, the temperature of the electrolyte and the applied potential/current density. The real chemical reactions are rather complex. The resulting oxide film consists of two regions: next to the aluminum there is a thin, dense and compact layer of alumina, the barrier layer. Oxide dissolution and formation rate are in dynamic equilibrium at the barrier layer during the anodization process, which means that it has a constant thickness. Above this layer, facing the electrolyte, there is a thick porous alumina layer.

The porous aluminum oxide layer has a structure composed of hexagonal cells, each of which contains a pore at its center (see Fig. 2.4). Those pores are oriented perpendicular to the surface and parallel to each other. Two mechanisms play a role in the formation of these nanoscopic holes. On the one hand the growth of aluminum oxide at the interface between the aluminum metal and the already present alumina due to the transport of Al^{3+} , OH^- and O^{2-} ions within the alumina film and on the other hand the dissolution and deposition of aluminum oxide at the interface between the alumina and the electrolyte.^[17]

Pore formation. Several models have been developed for the pore formation and growth of porous anodic alumina films. The – to date – most widely accepted one is a hypothetical model proposed by K. Heber.^[22] The basic principle is depicted in Figure 2.3. In the first stage, prior to the anodization process itself, the bare aluminum is covered only by a thin layer of its native oxide. When the electric field is applied, the current is increasing and colloidal $\text{Al}(\text{OH})_3$ is formed. This thin layer is very fragile and its stability depends on a variety of factors. It represents the precursor for the alumina and is growing linearly over time according to Faraday's

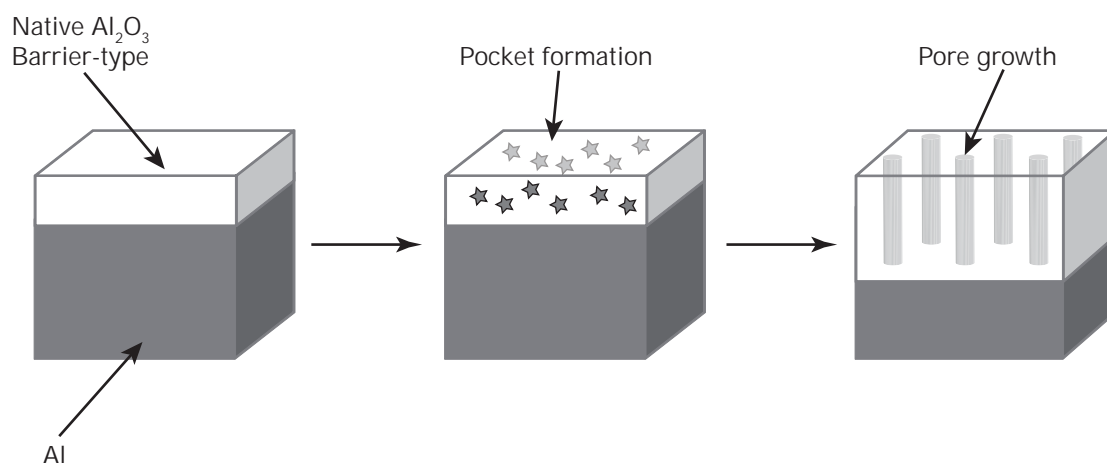


Figure 2.3 — Mechanism for anopore growth according to the Heber model.^[22] Under the influence of an electric field, pockets are formed within the native oxide layer. During the anodization process, these pockets open up; thus they act as the nucleation sites for the pore growth.

law. Within this colloidal boundary layer, small “pockets” – or better described as bubbles – in the range of several nanometers are formed. Incoming OH^- ions from the electrolyte produce an “electrolyte stream” in which the hydroxyl ions can react with the boundary layer. The pockets, which are densely packed inside the colloidal layer, contain Al^{3+} , OH^- , and the ions of the electrolyte (e.g. HC_2O_4^- , HSO_4^- , etc.). This results in an inner pressure from osmotic or electro hydrodynamic forces; thus, the pockets open up. At the same time, the surrounding colloid coagulates to yield solid aluminum oxide. From now on, both the thickness of the alumina and the length of the pores are increasing and an equilibrium growth is achieved. Over the whole anodization process, the barrier layer is moving deeper into the aluminum as the porous layer grows. The overall growth rate is controlled by Faraday’s law.

The most important parameters that affect the textural properties of the oxide film (pore diameter, pore density, wall thickness, etc.) are the applied voltage and current density, the pH, the type of the electrolyte, and the temperature. The model of

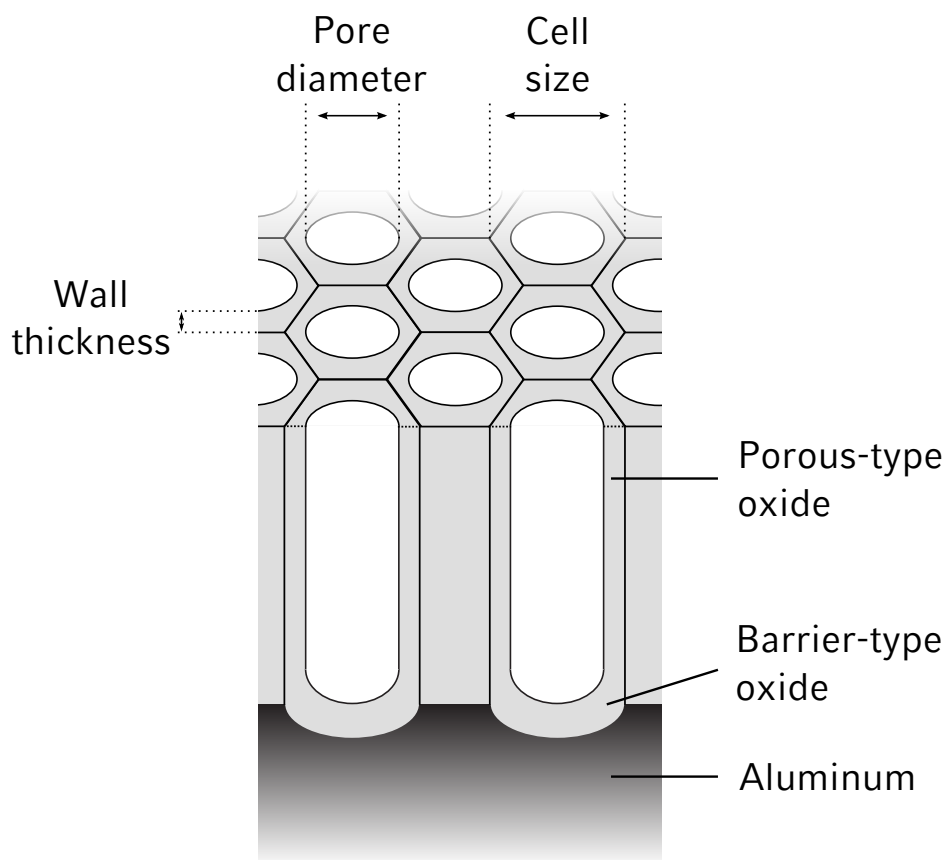


Figure 2.4 — Scheme illustrating a section through a porous anodic alumina film and the most important textural parameters. The thick porous-type alumina layer is separated from the unanodized aluminum by a thin, non-porous barrier-type film of aluminum oxide. Adapted from [23].

an alumina membrane showing the most important textural parameters is shown in Fig. 2.4.

Effect of the electrolyte. The different electrolytes determine the possible pore size ranges; however, the mechanism is still unclear at this point. The experimental data for the three most commonly used acids are given in Table 2.2. The data show that H_3PO_4 has the tendency to form the largest pore sizes and unit cells of these three; while the use of H_2SO_4 as electrolyte will result in small pore diameters.

Effect of the pH. At a constant current density, increasing the pH will decrease the dissolution rate and hence increase the barrier layer thickness. In turn this increases the equilibrium voltage. As the interpore spacing is strongly dependent on the voltage, a strong effect of pH on pore spacing is observed. This also leads to an increase in pore size, but with a weaker dependence on pH. The result of these effects is a decrease in porosity due to a stronger increase in pore spacing than pore diameter. At a constant voltage, increasing the pH decreases the dissolution current density. However, to maintain a constant voltage, the oxidation current density must also decrease. Thus the total equilibrium current density will decrease with pH.

Acid	Voltage	Pore diameter [nm]	Cell diameter [nm]
H ₂ SO ₄	25-27 V	> 13	50-60
(COOH) ₂	40 V	> 25	90
H ₃ PO ₄	195 V	> 200	500

Table 2.2 — Typical anodization voltages, anopore diameters and cell sizes obtained by standard anodization conditions using different acids.^[17]

Effect of the applied voltage/current density. In general, the applied electrical field (voltage) and the current density depend on each other; thus one of both can be neglected. The equilibrium total current density and the total aluminum reacted increases with increasing voltage as both the oxidation and dissolution rates increase with increasing voltage. However, the oxidation increases at a faster rate than the dissolution and hence the ionic current efficiency is increased with increasing voltage. Thus, the porosity decreases with increasing the voltage.^[24] This implies a

weaker than linear dependence of the pore diameter on the applied voltage. Only at high voltage the observed porosities are independent of the applied voltage. As the pore spacing increases linearly with voltage, the density of pores is inversely proportional to the square of the applied voltage. Since the dependence of current efficiency for oxidation on the applied voltage is stronger than the porosity dependence especially at higher voltages, the increase in total volume of alumina is accompanied by an increase in the thickness of the porous alumina layer.

2.2.3 Applications of anodic alumina

Application of anodic alumina in industry

Because of its low density combined with good mechanical properties, aluminum is a widely used metal in architecture, engineering, aircraft construction, etc. Unfortunately, pure aluminum is rather reactive; thus aluminum surfaces very often have to be protected with coatings. In industry, anodic alumina coatings have widespread use due to their diverse properties. Some of these properties include an excellent corrosion resistance, a decorative appearance (including the possibility to include dyes to produce colored surfaces), and high mechanical strength.^[16] Furthermore, aluminum oxide is not reported to present any toxicological risks.

For the use as protective coatings, so-called hard anodization processes have been developed in addition to the standard anodization processes. Hard anodization is carried out at comparably high anodization currents and voltages.^[25] This leads to the formation of films with up to 100 μm thickness and excellent mechanical

strength. Thus, typical applications of hard anodized films are coatings for mechanically and thermally stressed aluminum or aluminum alloy components.^[16,26]

Another highly important application of anodized alumina surfaces is the fabrication of colored and decorative metal surfaces. AAO films, synthesized using the standard procedures, are colorless. By the incorporation of dyes into the porous system of the AAO film, highly attractive surfaces can be produced.

Application of anodic alumina in nanoscience

Nowadays, scientific interest in porous anodic alumina membranes is mainly focused on their use for the template synthesis of 1-D nanostructures, such as nanowires and nanorods. Anodic alumina membranes offer a number of attractive features, for example::

- Adjustable pore sizes (between 10 to 400 nm)
- High pore densities (up to 10^{11} pores/cm²)
- High aspect ratios of the anopore channel system
- The ability to produce ordered systems over large areas
- A fast and well-documented process; no clean room is necessary during the synthesis

The template synthesis of 1-D nanostructures is discussed later on in the thesis (see Section 2.3 for mesoporous nanofibers and Chapter 3 for nanowires).

2.3 Mesoporous structures in confined environments

This section is based on the review article “Mesoporous structures in confined environments” submitted to *Advanced Materials*.^[21]

2.3.1 Introduction to periodic mesoporous materials

According to IUPAC, materials with diameters in the range of 2-50 nm are classified as mesoporous and are distinguished from macroporous or microporous materials that have larger or smaller pore diameters, respectively.^[27] Amongst them, inorganic periodic mesoporous materials have attracted considerable attention as a basis for designing nanoscale architectures by applying bottom-up strategies since their discovery in 1992.^[28] These materials are chemically, mechanically, and thermally quite stable due to their inorganic framework^[29] and exhibit not only high specific surface areas but also monomodal pore size distributions and regular pore arrangements. Highly ordered powder materials have been produced in basic or acidic media,^[28,30] and worm-like phases have been prepared under neutral conditions,^[31] always exhibiting a uniform pore size and Bragg-reflections at small angles in the corresponding diffraction patterns. The synthesis of periodic mesoporous material is based on the use of surfactant molecules acting as structure directing agents (SDAs). Surfactants (surface active agents) are molecules with hydrophobic and hydrophilic parts that self-organize in solution into micelles and eventually assemble into liquid crystal phases, depending on stoichiometry.^[32,33] Inorganic precursors are added to a solution of a surfactant and are condensed us-

ing appropriate conditions, such as basic or acidic catalysis. Condensation takes place at the surfactant/water interface and finally leads to the formation of an inorganic/organic composite material.^[34,35] The remarkable ability to tune structural order, pore size, and pore topology has resulted in periodic materials with different cubic,^[35–38] hexagonal,^[28,35] and lamellar^[35] structures, based on spherical, elongated, rod- or sheet-like micellar structures, respectively (Fig. 2.5).

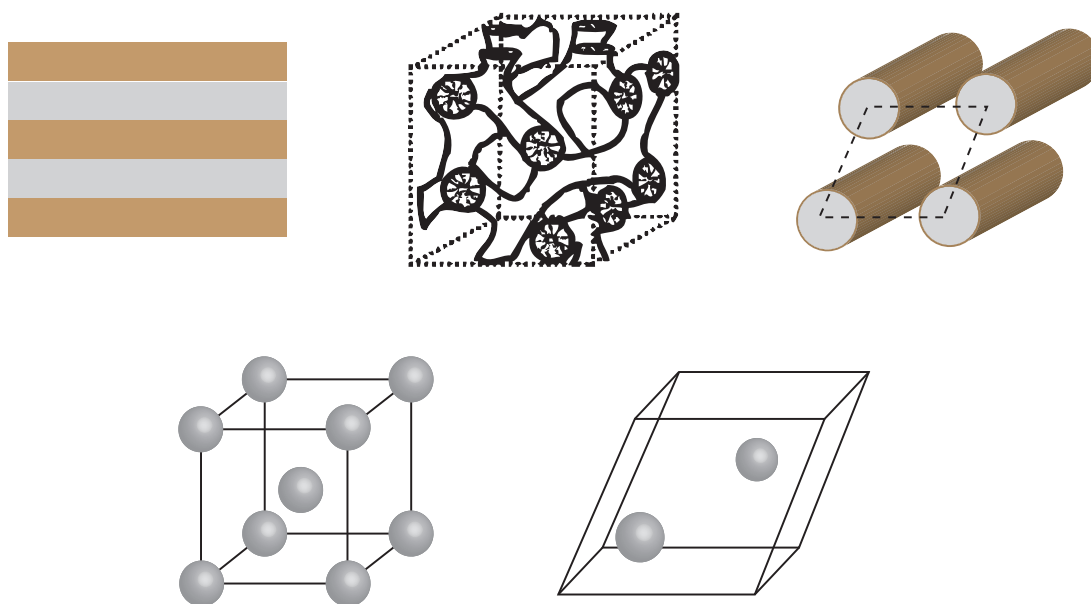


Figure 2.5 — Schematic illustration of different lamellar, hexagonal, and cubic structures formed with sheet-like, cylindrical, or spherical micellar structures. Differently colored micelles in the sketch of the cubic $Pm\bar{3}n$ structure are used to clarify the structure. The blue micelles are arranged in a cubic body-centered manner, two yellow micelles each are positioned on each plane of the cube.

While mesoporous silica materials have been most widely studied, other framework compositions could be realized as well, e.g., with the oxides of titanium, aluminum, zirconium, tin, or multimetal oxides, respectively.^[39,40] Even non-oxide materials such as metal sulfides,^[41] selenides,^[42] or phosphates,^[43] or pure mesoporous metals^[44] have been synthesized. Inorganic mesoporous materials were

2.3. MESOPOROUS STRUCTURES IN CONFINED ENVIRONMENTS

also used as template for the synthesis of porous carbon replicas (exo-templating)^[45] or nanoporous polymer-carbon composites.^[46] Organically functionalized periodic mesoporous materials have been synthesized via post-synthesis grafting, co-condensation, or as organic-inorganic hybrid materials, often motivated by their high potential for applications in heterogeneous catalysis.^[10]

Mesopore systems have been used as optical waveguides,^[47] as hosts for numerous molecular and cluster-based catalysts,^[48] for selective sequestration of contaminants,^[49] chromatography,^[50] and for novel drug delivery systems.^[51,52] Periodic mesoporous organosilica coatings were reported to have low dielectric constants, suggesting potential utility as low-k layers in microelectronics.^[53] Living cells were immobilized in biocompatible silica mesostructures and used as a model eukaryotic sensor.^[54] Individual bacteria of *Staphylococcus aureus* were immobilized within mesoporous silica nanospheres by Brinker and coworkers.^[55] That way, it was possible to study the quorum sensing of individual, isolated *S. aureus* bacteria.

Many of the envisioned applications, such as separation membranes, sensors or optoelectronic devices would benefit from growing mesoporous materials as films at surfaces or interfaces. Thin mesostructured silica films have been prepared on a variety of substrates by coating of conventional synthesis solutions,^[56,57] or via the evaporation-induced self-assembly method (EISA).^[58] The EISA approach employs homogeneous coating-solutions with volatile solvent (e.g. ethanol) and surfactant concentrations below the critical micelle concentration (see Fig. 2.6). Silica precursors are typically obtained by acid-catalyzed hydrolysis of tetraethyl orthosilicate (TEOS) or related precursors. The synthesis-solutions are spin- or dip-coated or cast on various substrates. Rapid solvent evaporation drives the self-assembly process towards the critical micelle concentration and the formation of the liquid-

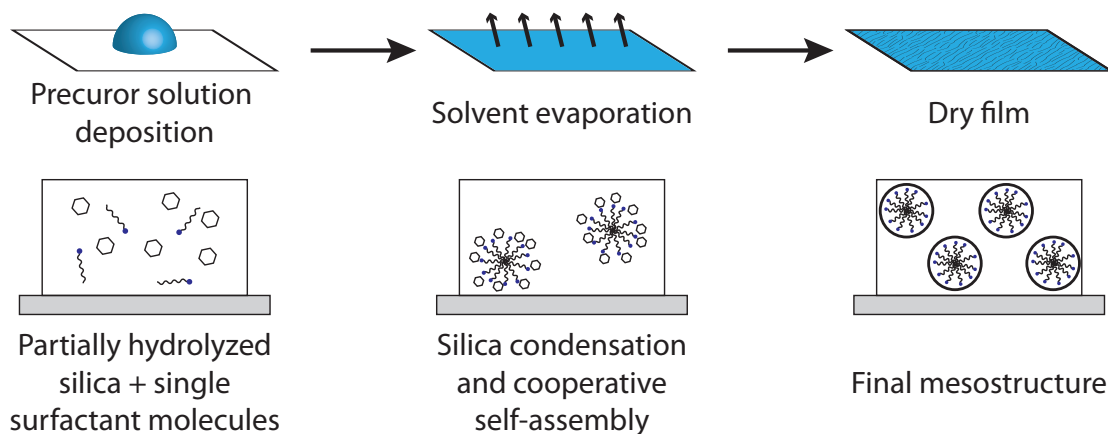
Evaporation induced self-assembly (EISA)

Figure 2.6 — Scheme of the EISA process. The synthesis procedure is shown on the top, the bottom line illustrates the cooperative self-assembly and silica condensation towards the final mesophase film.

crystal mesophase. Simultaneously, the silica-condensation is induced by increasing the concentration of acid. The dynamic, liquid crystalline character of the as-deposited films is indicated by self-healing processes or the possibility of phase transformations prior to solidification by, e.g., thermal treatment of the as-synthesized films.^[58,59] Different phases were found to form even after completion of the EISA process depending on the humidity during aging, thus the presence of a modifiable steady state was postulated.^[60] An 'EISA adapted diagram of textures' was established for mesoporous silica films prepared with CTAB as structure directing agent.^[61]

The mesoporous domains in thin films on flat supports often exhibit preferred orientation with respect to the substrate surface. However, for most systems, the domains are randomly rotated against each other on the substrate plane (Figure 2.7).^[62] For some of the potential applications of these systems, for example in nanoscale electrical or optical devices, further control over the mesopore orienta-

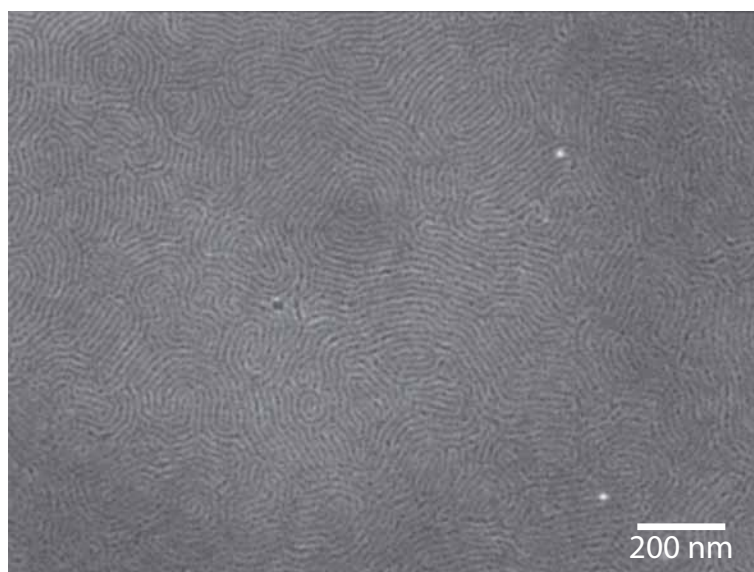


Figure 2.7 — HR-SEM image of a mesoporous silica thin film prepared by spin-coating with 2D hexagonal channel systems. The individual domains are rotated against each other leading to the formation of multiple phase boundaries.

tion would be highly desirable.^[63–65] Thus, there have been great efforts during the last years to control the domain size and orientation, particularly for mesoporous films with 2D hexagonal structure on flat substrates. These efforts include the application of external forces such as electric^[66–68] or magnetic^[69,70] fields, synthesis within a flow,^[71] or use of chemically^[72,73] or lithographically^[65] treated substrates.

Among the different possible orientations of 2D hexagonal mesoporous structures, a vertical alignment of the mesopores relative to a flat substrate appears to be the most difficult to achieve. Recently, a promising approach towards such films was developed, employing chemically modified substrates that exhibit no preferential interaction with either part of the surfactants employed. The lack of preferential interactions between substrate and organic template apparently promotes the desired

structural alignment.^[74-76] Following this principle, the synthesis of films with vertically aligned pores that are optimal as potential templates for nanowire growth was reported.^[77] In that publication, films with vertical pore alignment in the film center have been prepared. Nevertheless, the films still feature a mesopore alignment parallel with respect to the substrate at the film-substrate and film-air interfaces. The authors focused their attention on preventing the parallel mesopore alignment at the interfaces by substrate modification and ageing the films under controlled atmosphere for several days. There was no further comment on the unusual pore-alignment observed in the film center. Another interesting approach to obtain a perpendicular orientation is pore alignment driven by applying an electric field.^[78,79] By using a conductive substrate and applying voltages in the range of -1.7 V (against Ag/AgCl) on ITO substrates and -2.2 V (against Ag/AgCl) on glassy carbon substrates, the authors were able to synthesize mesostructured silica thin films. Depending on the synthesis conditions, they could obtain films with a 2D hexagonal mesostructure perpendicular to the substrate surface. Perpendicularly oriented thin films can also be obtained by utilizing a “nanometer-scale epitaxy” approach.^[80] By matching the lattice parameters of a cubic Titania film in (111) orientation to the lattice parameter of a subsequently synthesized 2D hexagonal silica film on top, a mesoporous thin film with mesopore channels running perpendicular to the original substrate orientation was obtained.

This review focuses on another feasible, recently developed method to control the orientation of the mesopore system, which is the synthesis of mesoporous materials within regular, larger channels of anodic aluminum oxide membranes (AAO membranes, also named AAM for anodic alumina membranes or PAA for porous anodic alumina).^[81,82] The latter membranes are produced by electrochemical oxidation of

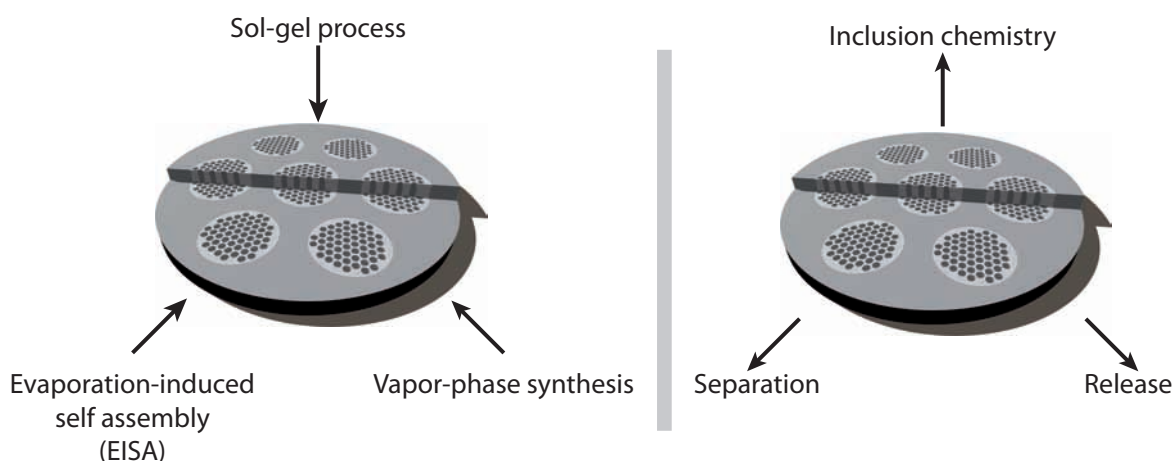


Figure 2.8 — Synthesis pathways and applications of ordered mesostructured materials confined within the pores of anodic alumina.

aluminum, with the metal directly acting as the anode (anodization).^[15,83–85] Dissolution and redeposition processes during anodization lead to the formation of porous films exhibiting monomodal sized and vertically oriented channels with diameters between about 10-500 nm. In a related context, these membranes were found to induce the orientation of various types of crystals such as apatite.^[86–89] As we discuss in the following, these high aspect ratio channels can also induce orientation in mesoporous phases.

2.3.2 Synthesis of inorganic mesostructured materials within the vertical channels of aluminum oxide membranes

In general, three different synthesis routes have been followed to include mesostructured systems in the AAO matrix. The first approach is based on the sol-gel synthesis of mesostructured powders and involves the immersion of the porous membranes in a synthesis solution throughout the gelation process.^[90-94] Typical solutions for such a process contain relatively low amounts of solvent and high surfactant concentrations. The gelation process is often induced by hydrothermal treatment and takes from several hours up to days. The second approach follows the EISA process^[58] conventionally used in thin film synthesis. It involves soaking the alumina substrate with small amounts of precursor solutions and subsequent solvent evaporation-induced gelation and structure formation.^[95-103] Synthesis solutions used for this approach contain comparatively high amounts of volatile solvent and low surfactant concentrations. This is done in order to obtain cooperative micelle formation and self-assembly of the condensing silica species. The rate of the synthesis in this case is limited by the rate of solvent evaporation, which usually takes a few minutes. A third approach reported recently is based on a vapor-phase synthesis of the mesophase within the alumina channels.^[104] In a first synthesis step, the alumina template is soaked in a solution of the surfactant at a concentration already above the critical micelle concentration (cmc). Then, in second step, the membrane is transferred into a closed vessel, which contains tetraethoxy silane (TEOS) vapor. The TEOS molecules then can diffuse into the pre-ordered micelles and the final mesophase is formed. An overview of the different approaches reported in the literature for the synthesis of mesostructured materials inside AAO-

2.3. MESOPOROUS STRUCTURES IN CONFINED ENVIRONMENTS

channels and the observed mesophases and their morphology is given in Table 2.3.

Table 2.3 — Summary of reported procedures for synthesis of mesophases within AAO membrane channels and overview on the reported mesophases.

Lit.	SDA	Initial sol-gel composition ^a [SiO ₂ : SDA : H ⁺]	Method	Structure, Morphology
[90]	F127	1 : 0.005 : 0.01	Sol-gel	Circular hexagonal tubes in unmodified, rods in modified AAO membranes
[91]	P123	1 : 0.017 : 0.02	Sol-gel	Columnar hexagonal rods
[92]	P123	1 : 0.012-0.023 : 0.009	Sol-gel	Mixture of circular hexagonal and columnar hexagonal phase, with increasing surfactant content formation of lamellar phase rods
[93]	P123	1 : 0.017 : 0.02	Sol-gel	Circular hexagonal or columnar hexagonal depending on water vapor present during ageing tubes (aged outside AAO), rods (aged inside AAO)
[94]	P123	1 : 0.017 : 0.02	Sol-gel	Circular hexagonal or Mixture of columnar hexagonal and lamellar phase depending on water vapor present during ageing rods (aged inside AAO)
[95]	P123	1 : 0.0096 : 0.001	EISA (dip-coating)	Circular phases ^c , rods
[96]	CTAB	1 : 0.075 : 0.004	EISA (casting)	Disordered columnar hexagonal rods
[97]	CTAC	No detailed composition given		Circular hexagonal phase with P123 and CTAC, cubic phase with F127 (not further classified) rods
[98]	F127	1 : 0.006 : 0.065	EISA (sequential casting)	Cubic Im3m structure with F127 according to powder XRD (higher order in silica material according to TEM) rods

continued on next page

continued from previous page

Lit.	SDA	Initial sol-gel composition ^a [SiO ₂ : SDA : H ⁺]	Method	Structure, Morphology
[99]	Brij 56	1 : 0.135 : 0.0035	EISA (dip-coating)	Mixture of circular hexagonal and cubic Ia3d phases (according to powder XRD) rods
[100–101]	CTAB P123 Brij 56	1 : 0.177 – 0.26 : 0.06 1 : 0.013 – 0.017 : 0.06 1 : 0.133 – 0.181 : 0.6	EISA (casting)	Columnar hexagonal structure with ionic CTAB, pure circular hexagonal or mixtures of circular/columnar hexagonal or columnar hexagonal/tubular lamellar phases with non-ionic P123 or Brij56 rods
[103]	P123 Brij 56	1 : 0.013 : 0.06 1 : 0.133 : 0.06	EISA (casting)	Columnar hexagonal structures with non-ionic P123 or Brij56 and inorganic salt additives rods
[104]	DeTAB DTAB TTAB CTAB	n. a.	Vapor-Phase	Columnar hexagonal structures with CTAB; with decreasing length of the alkyl chain of the surfactant the structure is tilted more and more towards a circular phase.

[a] all amounts were re-calculated corresponding to 0.01 mol silica precursor for comparison

[b] room temperature (RT)

[c] Due to synthesis in very small AAO-channels, unusual circular phases were observed, leading to the formation of chains of spherical micelles in channels with diameters smaller than 30 nm.

2.3.2.1 Sol-gel processes

In a first approach using a sol-gel method (scheme depicted in Figure 2.9) the triblock copolymer Pluronic F-127 (PEO₁₀₀PPO₆₅PEO₁₀₀) was used as structure directing agent.^[90] The anodic alumina membranes were used either as-purchased or after hydrophobization of the alumina surface with octyltrichlorosilane. They were immersed in a surfactant and TEOS-containing synthesis sol for 12 hours. After complete infiltration, the AAO membranes were taken out, the residual sol was scratched away from the membrane surface and the silica condensation was

2.3. MESOPOROUS STRUCTURES IN CONFINED ENVIRONMENTS

performed by exposing the composite membranes to air for 2 hours, followed by ageing at 60 °C for one hour and template removal at 450 °C for 3 hours. In unmodified AAO, the silica material was observed to form nanotubes, while nanofibers were formed when hydrophobized membranes were used as substrate. The tubes or fibers were found to have a 2D-hexagonal mesostructure with circular orientation. Similar (free standing) unusual mesophase structures are known from CTAB-templated fibers prepared by solvothermal methods and were named “circulites” or circular crystals.^[105,106] Silica-titania core-shell nanofibers were produced by immersing the silica nanotube-containing alumina membrane in tetrabutyltitanate for 12 hours and then inducing the sol-gel process by ageing in moist atmosphere for 48 hours (Figure 2.10).

When the surfactant concentration was increased, a mixture of circularly oriented mesopores and mesopores that were aligned along the long axes of the AAO-channels (columnar orientation) was observed in TEM images. A pure columnar orientation of mesoporous silica nanofibers was reported elsewhere using Pluronic P123 (PEO₂₀PPO₇₀PEO₂₀) as template and a sol-gel approach.^[91] The porous alumina membrane was placed inside the synthesis sol for 20 hours followed by additional ageing within the sol at 60 °C for 20 hours. On the contrary, silica fibers comprising a phase mixture of circular and columnar orientations were produced with the same recipe but different immersion time of the AAO within the synthesis sol (2-4 hours) and ageing outside the sol for 12 hours at ambient condition.^[92] Palladium replicas of the circular silica mesostructure were obtained, leading to the assumption of a helical extension of the pore system instead of the formation of a closed donut-shaped circular phase. A concentric, tubular lamellar phase was postulated to form at higher surfactant concentrations. It is difficult to confirm this phase as

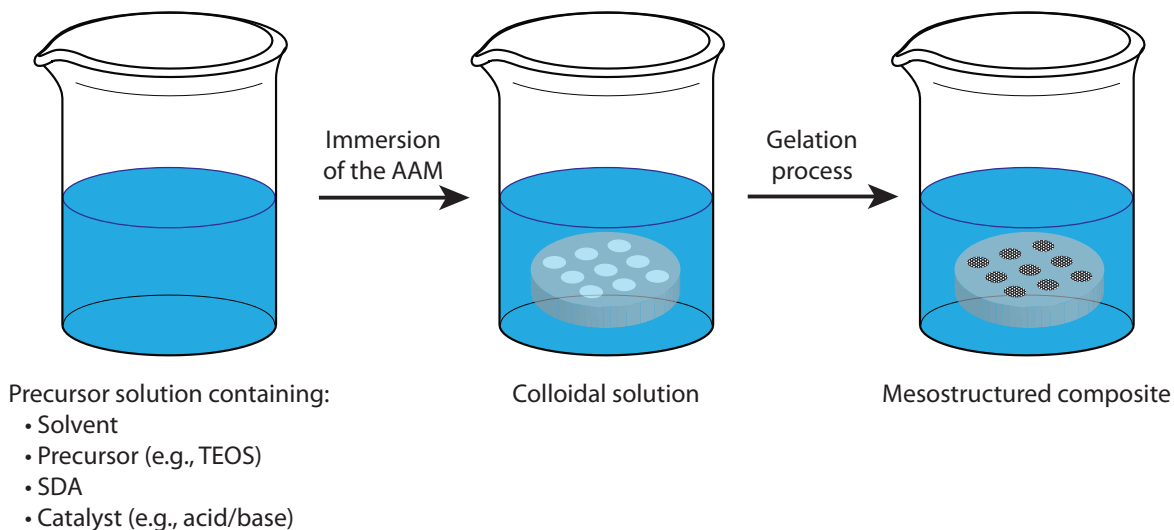


Figure 2.9 — Scheme of the synthesis of mesostructured material within AAO pores by a sol-gel/immersion method.

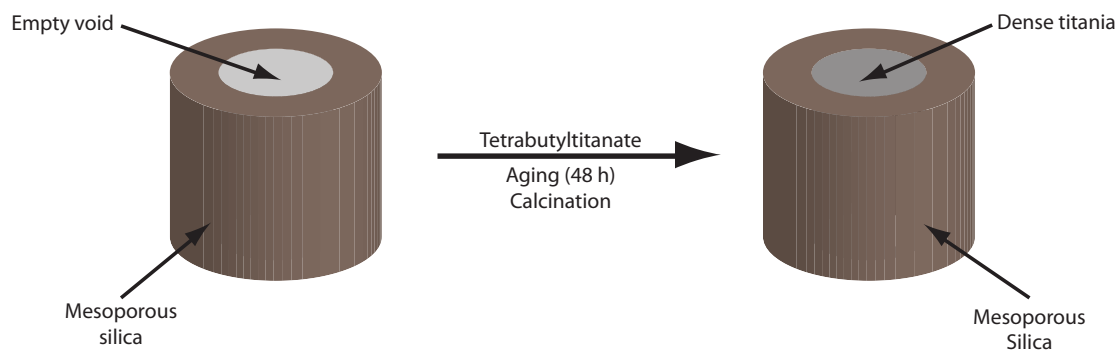


Figure 2.10 — Preparation of silica-titania core-shell material.

the side-view TEM images presented show the same stripe-pattern as the columnar hexagonal orientation. An overview over the structures and mesopore orientations within the channels of porous alumina membranes is given in Figure 2.11. Note that cubic phases were synthesized inside anodic alumina membranes,^[97,98,107] but so far no details regarding their orientation with respect to the channel wall have been discussed.

In a more systematic investigation of the influence of synthesis conditions on the final silica mesostructure, AAO membranes were immersed in a synthesis sol containing Pluronic P123 at the same surfactant: silica ratio as in the studies discussed above.^[93] After 30 minutes immersion time, one membrane was removed from the sol and aged at 60 °C for 12 hours. A second and third membrane were kept in the sol and aged at 60 °C for 12 hours with and without the presence of water vapor, respectively. While the formation of silica nanotubes was observed for the sample aged outside the sol, dense silica fibers were formed when the membrane was kept within the sol throughout the synthesis. It was suggested that during ageing within the sol material is constantly incorporated into the alumina channels, while ageing outside the sol limits the amount of included material. During gelation the volume of the sol decreases and the material is deposited only at the channel

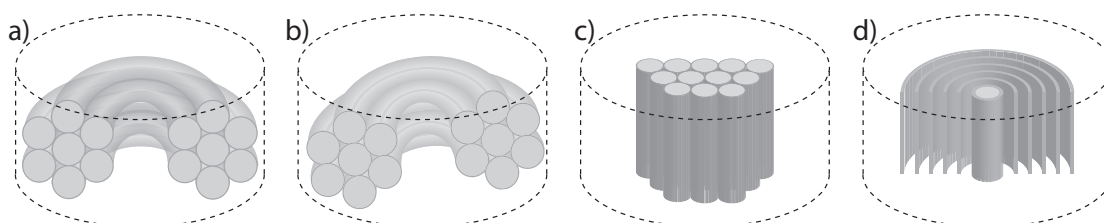


Figure 2.11 — Overview over observed mesostructures within AAO channels. The hexagonal phase is observed with two different orientations, either circular (helical or donut-like) or columnar.

walls, thus forming tubular arrays of mesostructured silica. Ageing within the sol in the presence of water vapor resulted in silica rods with a circular hexagonal arrangement of mesopores, while ageing without water vapor lead to the formation of silica rods with columnar hexagonal mesostructure. In a later publication, the silica fibers were reported to consist of a tubular lamellar structure surrounding a columnar hexagonal phase.^[94] It was suggested that the water vapor influences the rate of silica-hydrolysis (water vapor enhances condensation rate) and therefore has a strong impact on the structure formed. Thus, the circular hexagonal phase was presumed to be kinetically favored over the columnar hexagonal structure.

2.3.2.2 Synthesis *via* EISA

One can also take advantage of the efficient EISA method^[58] for the preparation of AAO-mesoporous composite materials, by applying coating solutions typically used for the deposition of mesoporous silica films. In one of the first studies, various porous alumina membranes with distinct channel diameters from 18 nm to 80 nm were employed as substrates and dip-coated with a synthesis solution containing Pluronic P123, which was used as structure directing agent.^[95] The composite membranes were aged at 25 °C and 65-70 % relative humidity for 24 hours and then calcined at 500 °C. Different mesostructures were found depending on the confinement conditions imposed by the different diameters of the alumina nanochannels, ranging from single chains of spherical mesopores to concentric or chiral helical mesopores (Fig. 2.12). These systems were compared to structures simulated by self-consistent field theory. Domain sizes of the isolated structures imaged by TEM were found to be quite large. Thus, a formation mechanism was proposed invoking an evaporation-induced solvent gradient within the AAO-channels, and subsequent structure formation at the disorder-to-order interface moving through the channel height. Although the formation of mesostructures inside membranes with different channel diameters is an interesting subject, to date not many studies have addressed this subject. This may be due to the limited availability of different channel diameters; commercially available membranes are limited at around 200 nm channel diameter and the synthesis of porous alumina membranes having small channel diameters and highly ordered patterns requires precise control of processing parameters.^[84,95,108]

Replicas of the above structures were obtained by electrochemically filling the meso-

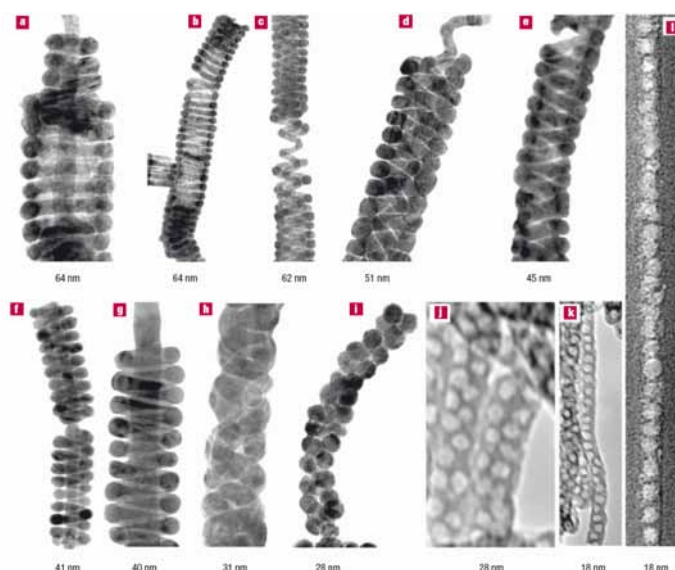


Figure 2.12 — Representative TEM images of mesostructures formed inside alumina nanochannels with differing confinement dimensions. The confining nanochannel diameter is indicated underneath each image. Reprint from [95].

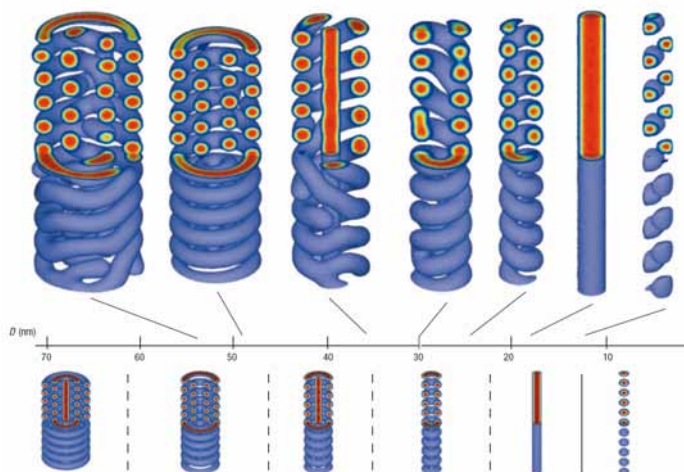


Figure 2.13 — Simulated structures of the confined self-assembly in cylindrical confinement with varying cylinder diameter (D). Calculations were made using selfconsistent field theory. Reprint from [95].

2.3. MESOPOROUS STRUCTURES IN CONFINED ENVIRONMENTS

pores of the calcined samples with silver^[95,109] as well as with nickel and copper oxide.^[109] After dissolving the silica/alumina matrix, a TEM investigation revealed the formation of dense and hollow nanowires, including even coaxial multilayered metal structures.^[109] Surface enhanced Raman spectroscopy was performed on a bundle of silver mesostructured nanowires with Rhodamine G6 molecules adsorbed. Surprisingly, even replicas from concentric circular mesopores (donut-like) were obtained by the electrochemical deposition method. These stacked circular structures were reported to break into individual rings upon sonication. Thus, a connection between the mesopores through micropores similar to those observed in bulk mesoporous SBA-15 was discussed.

A very similar phase behavior as discussed above was confirmed in another publication Lai et al.^[110] Here, the confinement effect of silica filaments was studied in AAO and EPC (track-etched polycarbonate) membranes with diameters in the range between 10 to 200 nm by scanning transmission electron microscopy (STEM).

Cationic CTAB was also used as a surfactant template for the synthesis of mesostructured silica - alumina composite membranes.^[96] A typical EISA solution was dropped onto a commercially available AAO membrane and sucked into the alumina channels by careful aspiration, followed by drying under ambient conditions. The resulting silica material showed some level of columnar mesopore alignment in the vicinity of the alumina walls while little order was observed in the remaining volume of the silica fibers. It was suggested that adsorption of CTAB at the alumina induces the growth of mesostructured material at the channel walls leading to decreased concentration of surfactant and silica deeper inside the alumina channels. Thus, the nanocomposite is supposed to form only near the front surface of the

membrane. This is contrary to the observations discussed above, showing that the mesostructured material tends to shrink in radial direction rather than along the alumina channels. Adsorption-desorption isotherms of the composite membranes were obtained after calcination at 400 °C showing type-IV isotherms typical for mesoporous materials. The composite membranes showed promising behavior for molecular separation, specifically when uncalcined. Comparatively small molecules such as Rhodamine B and vitamin B 12 could pass through the mesopores, while larger molecules such as myoglobin or bovine serum albumin could not.

First comprehensive diffraction experiments on the formation of mesophases inside the AAO channels were published in a combined two-dimensional small-angle X-ray scattering (2D SAXS) and TEM study.^[100] Composite membranes of mesostructured silica in AAO substrates were produced with three of the most often used surfactants CTAB, Brij56, and P123, respectively. The AAO membranes were loaded with precursor solutions having different surfactant-to-silica ratios, and left to dry under ambient condition (temperature, pressure) and controlled humidity. Diffraction patterns from the as-synthesized intact composite membranes provided semi-quantitative information about the volume distribution between the different phases even in phase-mixtures (Figure 2.14). While circular hexagonal phases exhibit two 01_r -reflections (in q_x -direction, denoted as in-plane (ip)-reflections) and additional 10_r reflections (out-of-plane (op)-reflections), the columnar hexagonal structure shows exclusively the two reflections in q_x -direction ($01, 0-1$, see Figure 2.14). The ratio of the intensity of the 10_r -reflections and the intensity of the reflections in q_x -direction gives the semi-quantitative information about the distribution between the phases. A ratio of about 1 represents a pure circular hexagonal phase, a ratio of 0 a pure

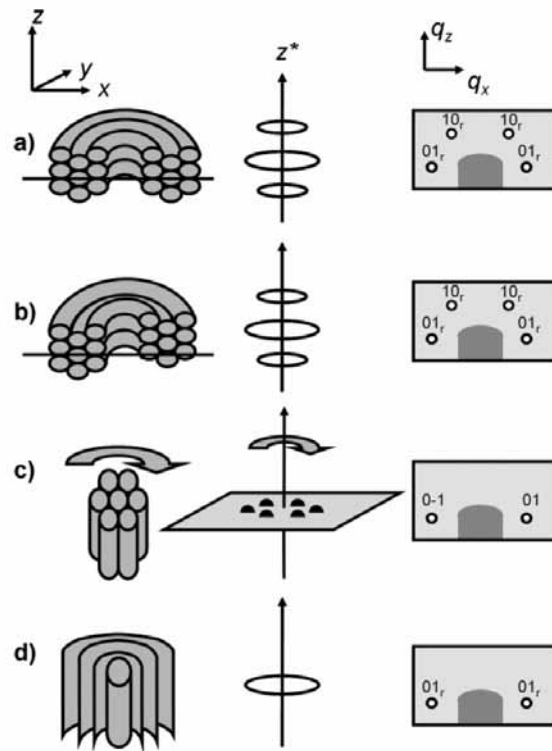


Figure 2.14 — Sketch of the observed structures within the AAO-channels and description of their intensity-maxima in reciprocal space and their respective diffraction patterns corresponding to the 10 reflection of a normal hexagonal (a-c) or lamellar (d) lattice. The circular hexagonal structure forming rings (a) or spirals (b) results in two 01_r -, and two visible 10_r -reflections (the other two -10_r -reflections are obscured by the sample holder). The index “r” denominates “ring” for reflections from ring-shaped intensity maxima, indexation is referring to a normal hexagonal lattice. The columnar hexagonal structure (c) and the tubular lamellar phase (d) both result in two reflections in the horizontal plane of the primary beam. Reprint from [101].

columnar hexagonal structure. In this study, ionic CTAB was found to exclusively lead to pure columnar hexagonal structures, the non-ionic surfactants Brij56 and P123 were observed to either lead to the formation of a pure circular, or mixtures of circular and columnar phases. The formation of the circular phase was enhanced by low silica-to-surfactant ratios and low humidity, respectively. The preferred formation of a columnar phase was observed at higher silica-to-surfactant ratios, or high humidity.

In a later study employing in-situ GISAXS with synchrotron radiation, the authors identified a third, tubular lamellar phase that sometimes was even the main phase in the mesoporous composites made with high silica-to-surfactant ratios.^[101] Figure 2.14 shows that the tubular lamellar structure exhibits two reflections in q_x -direction (01_r -reflections) just like the columnar hexagonal phase. Both phases can only be distinguished because the d-spacing of the hexagonal phase is smaller than the d-spacing of the lamellar phase by a factor of $\sin(120^\circ)$ (Figure 2.15).

As mentioned earlier, the identification of the tubular lamellar structure is critical not only in diffraction but also when imaged with TEM. When the lamellar fibers are viewed from the side, they show a similar stripe-pattern as the columnar hexagonal phase. When the fibers are imaged in cross-section, they exhibit a circular pattern similar to the circular hexagonal structure. However, the lamellar phase was found to collapse in the electron beam when the plane perpendicular to the fiber axis is imaged, most probably due to a lack of a three dimensional network when thinned for TEM imaging. In this case, the collapsed lamellar phase can be distinguished from the regular circular pattern of a circular hexagonal structure. In any case, high resolution diffraction, a combination of diffraction and TEM, or TEM-imaging of the fibers in side- and plan-views will allow the detection of a tubular

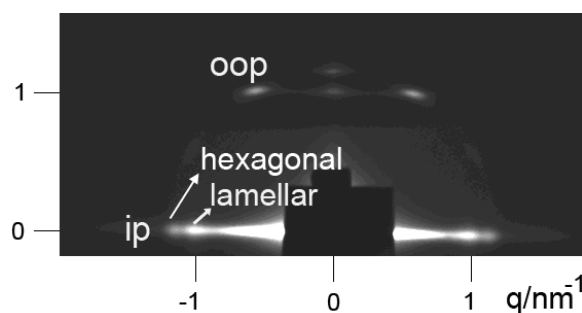


Figure 2.15 — Diffraction pattern collected with synchrotron radiation during an in-situ experiment while all three phases are present in the sample, the circular and columnar hexagonal structure as well as the tubular lamellar phase. The label oop denotes the out-of-plane reflection (10_r), ip the in-plane reflections (the 01_r , $0-1$ and 01 -reflections of the circular and the columnar hexagonal structures, and the 01_r -reflections of the tubular lamellar phase).

lamellar phase.^[101]

The above in-situ investigation of the structure formation also showed that using the ionic surfactant CTAB, the columnar hexagonal phase was formed directly from the beginning. When non-ionic surfactants (Brij 56, P123) were used, the circular hexagonal phase was found to form first, followed by a direct, partial transformation towards the columnar hexagonal structure (P123-sample), or complete transformation towards a columnar hexagonal / tubular lamellar phase mixture (Brij56-sample). Thus, the circular hexagonal structure was concluded to be kinetically favored and eventually transformed into more stable phases (compare [93]). The phase transformations were found to start after complete solvent evaporation in a period comparable to the modulable steady state found in thin film synthesis.^[60]

In a subsequent study, the phase formation and transformations were investigated in more detail, and a formation mechanism was proposed.^[102] The focus was on samples synthesized with non-ionic surfactants (Brij56, P123) at different relative

humidity (compare [100]). Again, the formation of ordered phases was found to start directly (no formation of intermediate wormlike phases) and quite late during synthesis, when almost all solvent is evaporated. Strikingly, phase transformations occur even after complete solvent evaporation. These transformations, depending on their type, were supposed to proceed from the channel wall towards the center of the fiber or from the fiber center towards the channel wall. For example, the tubular lamellar structure is preferentially formed at the channel wall, avoiding formation of highly curved lamellae directly in the fiber-center. The columnar hexagonal phase evolves from the circular phase preferentially at the fiber center, where the difference in energy between the strongly curved circular structure and the straight columnar channels is high. Moreover, several interfaces between domains with different structures were found along the fiber axis. Based on these observations, a formation mechanism was proposed (Figure 2.16), invoking fairly homogeneous removal of solvent by evaporation and formation of a disordered gel, followed by nucleation of structured domains at the channel walls at various nucleation sites distributed all over the height of the membrane-channels. During the last period, growth of the ordered domains and transformations between the different phases take place.

The content of solvent (water, since the volatile solvent ethanol has already evaporated) at the time of first structure formation and after complete solvent evaporation was compared for samples synthesized with the same precursor solution but at different relative humidities. The ratio of the sample weight after the respective synthesis times divided by the initial weight in percent was used as representative for the water content. Surprisingly, the results were found to differ for samples synthesized with Brij 56 and P123 as the SDA. The time at which the first structure

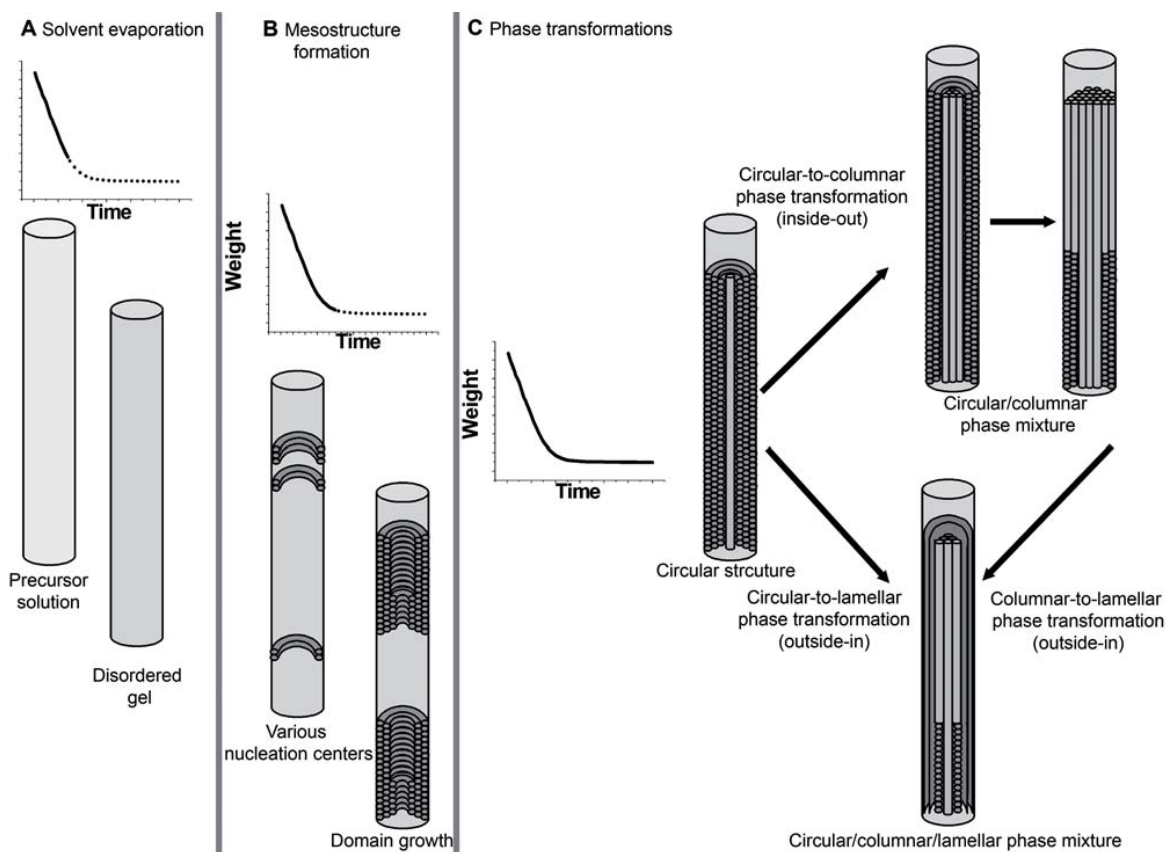


Figure 2.16 — Proposed mechanism for the structure formation within the confined space of AAO channels. The authors distinguish three major time periods. Period A is dominated by solvent evaporation and the formation of a disordered gel. During period B the final sample weight is reached, accompanied by the formation of ordered mesostructure. The sample weight is constant during period C, corresponding to the completion of the EISA process. Various phase transformations are observed during this time period, as shown in the figure. Reprint from [102].

formation could be observed varied with the humidity for the Brij 56 templated samples and was constant with P123 as the SDA. After completion of the EISA process, the relative sample weight was found to be constant for the Brij samples, regardless of the humidity during EISA, while the P123 samples were found to be dependent on the humidity. The authors concluded that the structure formation in samples synthesized with Brij56 is kinetically controlled (different ways towards a similar final chemical composition depending on the humidity), while structure formation in samples synthesized using P123 is more equilibrium controlled (similar way towards a different final chemical composition depending on the humidity). In this publication it was reported that under kinetic control (Brij56-samples), the kinetically favored circular hexagonal phase is formed at low humidity. At high humidity, when the flexibility of the system is maintained for longer time, transformation towards the columnar hexagonal phase takes place (compare [100]). In contrast, in equilibrium-controlled samples (P123) transformation towards the columnar hexagonal structure is more pronounced at low humidity than at high humidity. This is because under equilibrium control the final sample contains less water at low humidity. Thus, the head-group area of the surfactant is decreased and the formation of less curved phases is favored (e.g., the columnar orientation).^[61,111]

These mechanistic studies can explain why the production of samples with phase-pure circular hexagonal structure using non-ionic surfactants and EISA was easily achieved,^[100–102] while synthesis of the interesting columnar hexagonal phase is challenging. Higher surfactant-to-silica ratios lead to a higher volume fraction of columnar hexagonal structure,^[100] but formation of the tubular lamellar phase starts before phase-pure systems can be reached.^[101,102] Slow synthesis at high humidity leaves the system enough flexibility to transform from the kinetically fa-

2.3. MESOPOROUS STRUCTURES IN CONFINED ENVIRONMENTS

vored circular towards the columnar orientation, but high water content at high humidity enhances the stability of structures with higher curvature (the circular orientation).

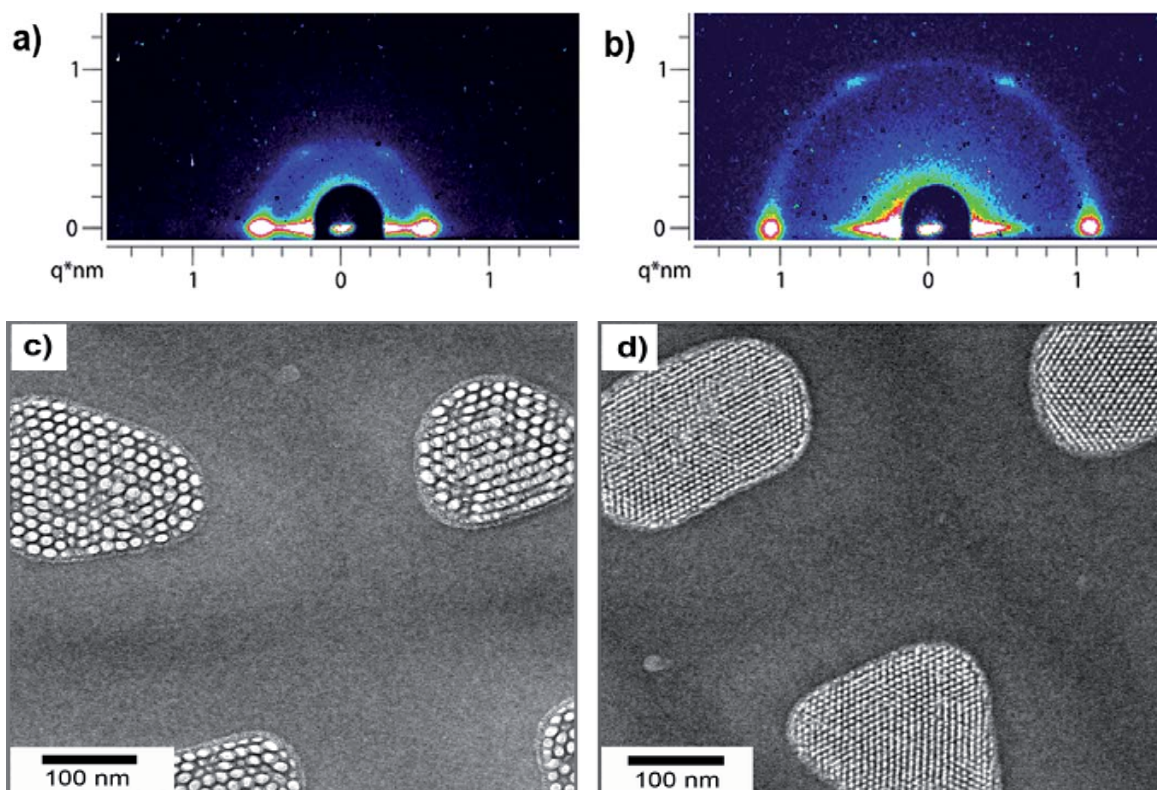


Figure 2.17 — SAXS patterns of samples a) synthesized with P123 and lithium chloride at 30 °C, b) synthesized with Brij56 and lithium chloride at 30 °C. The intense reflections in the horizontal plane of the primary beam show the strong domination of the columnar hexagonal phase. Plan-view TEM images of the samples c) synthesized with P123 and lithium chloride at 30 °C, d) synthesized with Brij56 and lithium chloride at 30 °C, showing pure columnar orientation of the mesostructure. Reprint from [103].

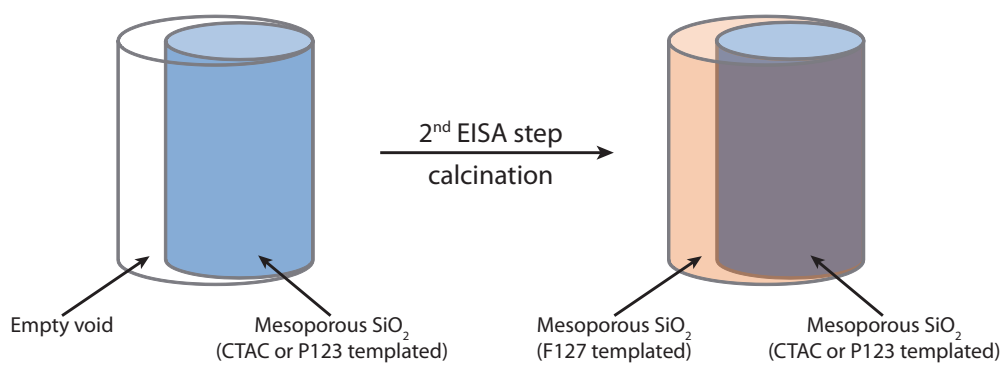
In a recent study, however, the synthesis of phase-pure columnar hexagonal systems was achieved using non-ionic surfactants and additional inorganic salts.^[103] The intention was to mimic the behavior of the ionic surfactant CTAB^[96,100,101] by

adding inorganic salt to precursor solutions containing non-ionic PEO-based structure directing agents. It is known that metal ions can be complexed by the ether chains in PEO, thus the surfactant can assume a more polar nature. The distribution between the phases was evaluated based on two-dimensional SAXS patterns in combination with TEM. The temperature was found to play a key role in the salt-induced formation of the columnar phase. For samples synthesized with P123, room temperature was reported to be sufficient, while higher temperatures (at minimum 30 °C) were necessary for the synthesis of the columnar structure. Different inorganic salts were investigated. Large anions were found to lead to a distortion of the mesostructure, while small cations were observed to be more efficient structure-directors for the columnar phase than larger cations. Best results were obtained with lithium chloride as inorganic salt (Fig. 2.17).

The structures were found to be calcination-stable with respect to structural quality and orientation. Sorption isotherms of ground samples revealed accessible mesoporosity. Besides enabling the synthesis of quasi pure-phase columnar hexagonal structure, the addition of inorganic salt was observed to enhance the interaction between the silica phases and the alumina surface of the matrix. For further applications such as molecular separators it is desirable to produce composite membranes where the mesoporous material completely fills the AAO channels. Especially in calcined samples, shrinkage of the mesostructure is often observed, thus leaving a gap between silica fibers and the alumina channel walls. The stronger interaction between the mesoporous material with the alumina channel walls can prevent formation of such gaps during calcination. The mechanical stress was found to be compensated by the formation of structures with comparatively large pore-diameters. In some cases, merging of the mesopores was observed rather than frac-

2.3. MESOPOROUS STRUCTURES IN CONFINED ENVIRONMENTS

Multiple silica mesophases:



Heterogeneous mesoporous oxides:

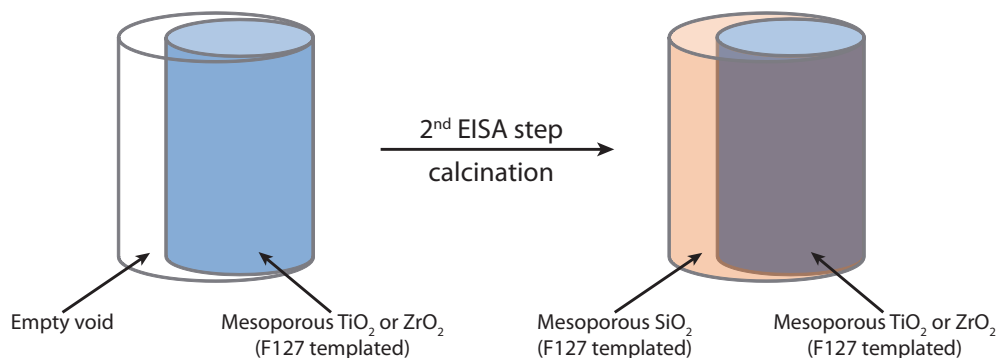


Figure 2.18 — Preparation of multiple silica mesophases or heterogeneous mesoporous oxide composites via sequential EISA processing.

ture between the silica material and the alumina wall.

In related work, sequential loading techniques were employed to overcome the problem of incomplete pore-filling, resulting not only in multiple mesoporous silica phases^[97] but also in composites of different mesoporous oxides (Fig. 2.18).^[98] In a first approach, ionic CTAC and Pluronic P123 were used as structure directing agents to obtain mesostructured composite membranes via the EISA approach. These materials were calcined leaving mesophases that only partially fill the AAO channels but mimic their respective shape. This behavior was attributed to completely filled channels at an early stage of the synthesis followed by shrinkage of

the structure most probably during template removal. The resulting composite membranes were used as substrates in a second synthesis step, where cubic silica mesostructures were obtained with Pluronic F127 acting as surfactant. Complete filling of the AAO channels with the hexagonal - cubic composite material was observed in TEM images. In a second approach, Pluronic F127 was used as template for the formation of mesostructured titania or zirconia in the AAO channels, followed by calcination. In a second step the voids between mesoporous oxide and the alumina channel walls were filled with mesostructured silica and calcined again. Complete filling of the AAO channels was probed by air permeability measurements. The measured values were reported to be in good agreement with literature values for permeation through mesoporous silica powder having 3 nm pore size.

2.3.2.3 Vapor-phase synthesis

Recently, a third approach for the synthesis of silica mesophases within alumina channels was reported by Lee et al.^[104] Inspired by a synthesis strategy known from silica films,^[112,113] the authors developed a vapor-deposition hydrolysis process, where the silica source (TEOS) is diffused into an already pre-aligned surfactant phase. In sol-gel chemistry and the EISA processes, various parameters, such as pH, molar composition, and temperature have to be precisely controlled. The main advantage of synthesis from a vapor phase may be experimental simplicity. The synthesis procedure is depicted in Figure 2.19. In a first step, the AAO membrane is immersed into the surfactant solution. Due to the negative surface charge of the alumina material, the head groups of the cationic surfactant molecules are expected to align on the pore walls, resulting in lamellar arrangement of the surfac-

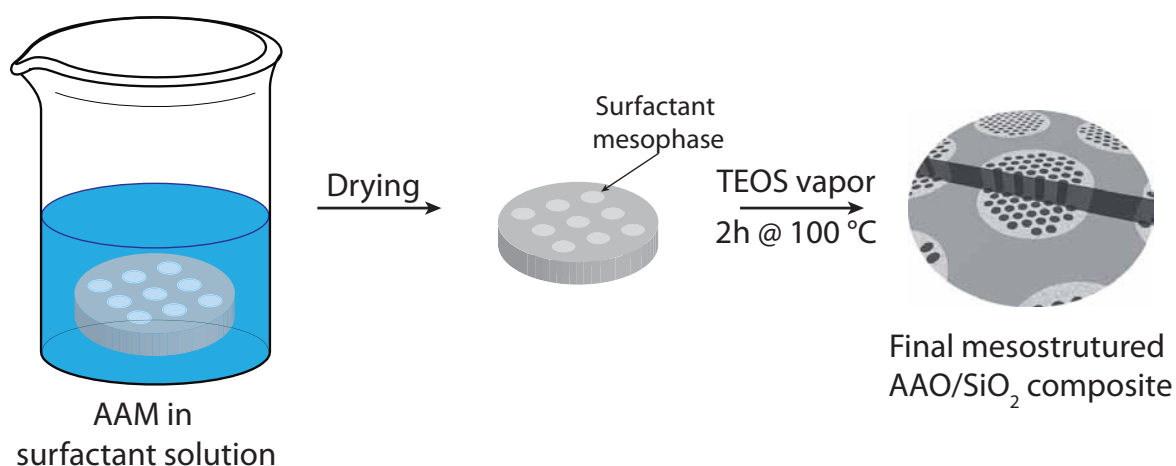


Figure 2.19 — Scheme of the vapor-deposition experiment. First, the alumina membrane is soaked in the surfactant solution. After removal, it is transferred to a closed vessel containing TEOS vapor. Upon the treatment, the mesostructure undergoes a phase change from a lamellar surfactant phase to columnar or tilted mesophases.

tant phase. The membrane is then transferred into a closed reactor and TEOS vapor is introduced. The vapor deposition and hydrolysis step itself is then carried out at a temperature of (minimum 100 °C) over 2 hours. Upon this diffusion of the TEOS molecules into the liquid crystalline phase, the former lamellar arrangement of surfactant molecules changes to hexagonal phases. While the authors found that the formed mesophase is independent of the concentration of the surfactant (as long as the concentration exceeds the cmc), the chain length of the surfactant used has a strong influence on the mesophase geometry. With decreasing chain length from CTAB (16 Carbon atoms alkyl chain) to DeTAB (Decyltrimethyl-ammonium bromide, 10 Carbon atoms alkyl chain length), the mesophase arrangement changed from a parallel alignment (hex. columnar phase) to a tilted alignment, which more and more resembled the circular hexagonal mesophase. The authors explain this by an enhanced surface tension.

2.3.3 PMO and carbon mesophases

By organic modification of the porous material one is able to tailor the properties of the inorganic silica to specific needs; thus it is possible to combine the advantages of inorganic mesoporous silicas (such as tunable pore sizes, high specific surface areas, and ordered pore systems) with the great diversity of organic chemistry. These kinds of materials can be classified as mesoporous organic-inorganic hybrid materials.^[10] Several strategies, such as co-condensation, post-synthesis grafting, and the direct synthesis from pure organo-silsesquioxanes have been developed for their synthesis. An excellent review on these class of materials is given by Hoffmann et al.^[10]

A widely used method for the in-situ functionalization of mesoporous silica is the co-condensation of a pure silica precursor (e.g. TEOS) with a respective organosilane. That way, a large number of functional groups – e.g., alkyl,^[114,115] aromatic,^[114] amino,^[115] and thiol^[115] groups – have been successfully introduced into the wall material of mesoporous silica powders and thin films. The co-condensation method enables a homogeneous incorporation of functional groups into the walls of the mesoporous structures. In a recent study, the influence of the presence of functionalized silanes on the structures and the orientation of the mesophase system within the AAO channels was evaluated by SAXS, TEM, and solid state NMR measurements.^[116] Both Brij 56 and Pluronic P123 were chosen as structure directing agents, and for both surfactants a remarkably different phase behavior was found. In unmodified Brij 56 templated samples, predominantly the formation of the circular mesophase was observed. This is in good agreement to previous studies.^[100,101] Depending on the humidity present during the EISA process, slight

2.3. MESOPOROUS STRUCTURES IN CONFINED ENVIRONMENTS

variations in the ratio of the circular mesophase to the hexagonal mesophase were found. SAXS results on samples synthesized at a relative humidity of 40 % indicated the formation of a purely circular mesophase (oop/ip ratio 0.99). In contrast, a relative humidity of 60 % led to the formation of a circular and columnar mixed phase (oop/ip ratio 0.55). For samples templated with Brij 56, two different sets of functionalizations were studied: alkyl-functional groups (with a varying alkyl chain length of 1 to 8 Carbon atoms) and functional groups having different chemical properties. Remarkably, the alkyl functionalization experiments could be divided into two groups. For short alkyl chain lengths (methyl to isobutyl) and low TEOS ratios the phase changed from circular to a partially columnar structure. With increasing silane to TEOS ratio, the phase changed back to the circular phase before forming a dense phase (no structure) at ratios exceeding 30 % organosilane. In case of the co-condensation experiments with longer alkyl chains (from pentyl to octyl) a different trend was observed. Here, the addition of already small amounts of the respective organosilane led to the formation of a lamellar side-phase. The functionalization with groups carrying basic (cyanopropyl), neutral (phenyl), or acidic (mercaptopropyl) moieties again showed a behavior similar to that observed with the short alkyl chain length. The authors therefore conclude that the length of the functional group plays a key role on the structure to be formed. Different conformations in the surfactant molecules (gauche vs. trans conformation) result in small shifts in the NMR spectrum; thus conformational effects of the alkyl chains on the surfactant molecules can be monitored that way. The gauche conformation can be associated with a higher degree of disorder of the template chains due to its higher mobility than the all-trans conformation. Therefore, decrease in the fraction of template molecules in all-trans indicates lower degree of order in the aggregates formed

by the template molecules. At some point a critical fraction of SDA molecules showing gauche conformation is exceeded and the formation of an ordered phase is no longer possible. These considerations are supported by the experimental data obtained by NMR spectroscopy. Similar experiments were carried out using Pluronic P123 as the SDA; however, already the presence of already 5 % of functionalized silanes led to a phase transformation to the lamellar phase. Surprisingly, also the influence of the humidity present during the EISA process and even changing the P123/Si ratio did not show a strong influence on the phase formation process.

Periodic mesoporous organosilicas are a special group in the field of mesoporous organic-inorganic hybrids. They were discovered independently in 1999 in the labs of S. Inagaki,^[117] A. Stein,^[118] and G. A. Ozin.^[119] PMOs are synthesized directly from bis(alkoxysilyl) precursors in the presence of an appropriate surfactant without any addition of an inorganic silica source. Thus, materials with a high loading of functional groups dispersed evenly over the whole wall material can be obtained. To date, a variety of different materials with linker groups such as ethylene, benzene, or thiophene have been synthesized. By choosing appropriate bridging groups it is also possible to synthesize PMO materials that exhibit various new and interesting properties unknown in purely siliceous mesostructured materials, such as crystal-like pore walls.^[120] Recently, the synthesis of PMO material within the channels of AAO membranes was reported.^[107] Starting from bis-(triethoxysilyl)ethane (BTSE) as the organosilica source, the phase behavior in the presence of CTAB and Brij 56 as SDA was studied. SAXS measurements in combination with TEM micrographs of CTAB based PMO/AAO composites revealed the exclusive formation of the circular hexagonal mesophase. This contrasts to the aforementioned purely siliceous systems, where the only mesophase that can be

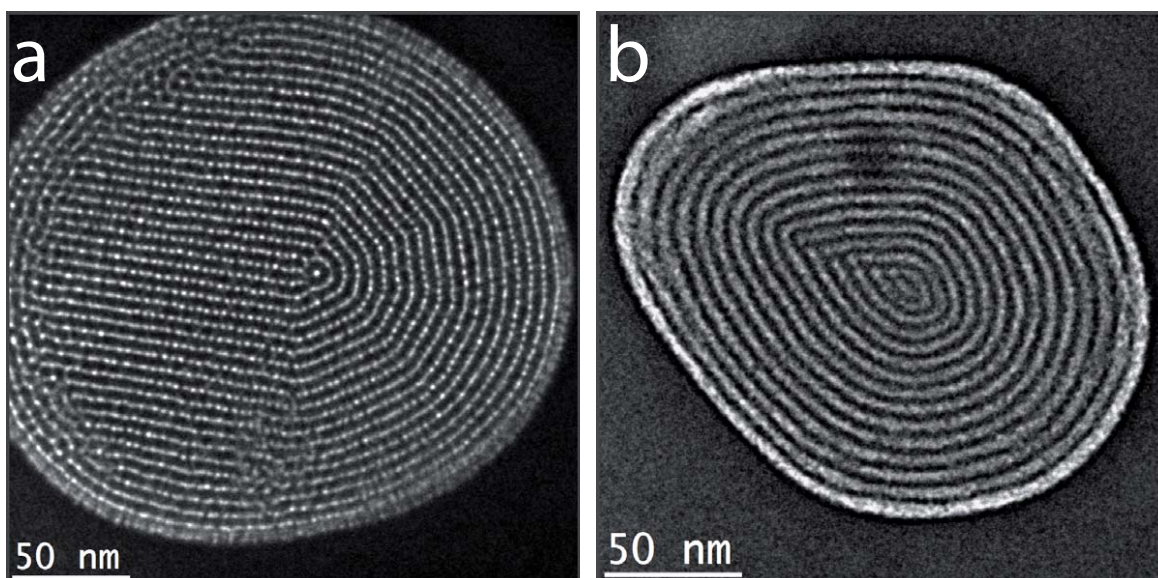


Figure 2.20 — TEM micrographs of Ethylene-bridged PMO material within AAO pores. The micrograph in a) is taken from the cubic mesostructure, b) represents the hexagonal circular variant.

observed is the hexagonal circular phase.^[96,100,104] One reason for this remarkably different behavior could be the result of a change in polarity and size of the organo-silica species in the PMO phase. When using Brij 56 instead of CTAB as the SDA for the EISA process, the existence of a cubic $Fm\bar{3}m$ phase was reported, in addition to the formation of the hexagonal circular and a lamellar phase. TEM images revealed excellent filling rates of the AAO channels, particularly in case of the cubic phase (Fig. 2.20). The possibility of removing the majority of the template molecules from these hierarchical systems by annealing at 120 °C and subsequent acidic ethanol extraction was proven by nitrogen sorption experiments. Because of the isotherm shape and rather broad pore-size distributions an incomplete surfactant removal was assumed. This assumption could be further proven by ^{13}C MAS-NMR measurements of respective samples. For a more efficient removal of the SDA molecules

from the PMO mesophases, different calcination temperatures were tested. The highest BET surface area ($85 \text{ m}^2/\text{g}$) was found for samples calcined at $250 \text{ }^\circ\text{C}$ in air. ^{13}C -NMR data showed that the template could be removed completely at this temperature and SAXS diffractograms and TEM micrographs confirmed that the mesostructure for both the cubic and the circular phase was perfectly retained. Potential applications of these hierarchical systems in nanofiltration and other fields require that the porous system is accessible for ions and molecules over the complete $60 \text{ }\mu\text{m}$ length of the pores. In order to evaluate access into the PMO/AAO systems, the pores of a calcined hexagonal circular sample were replicated by the electro-deposition of nickel.

In the last years, several methods to produce silicon-free mesoporous carbon-based structures (ordered mesoporous carbons, OMC) have been developed.^[74,121,122] In addition to high surface areas and large pore volumes, OMCs also show a high chemical inertness and - if carbonized - also electrical conductivity. Possible applications of OMCs therefore could include electrode materials for batteries, supercapacitors, fuel cells, adsorbents for separation and gas storage, and as catalyst supports. Furthermore, they could serve - similar to siliceous mesostructures - as hosts for the generation of periodic arrays of nanostructures. OMC bulk materials are usually synthesized either by hard-templating or soft-templating methods. Hard templating describes a process where an existing mesostructure (e.g., mesoporous silica) is replicated by a carbon based material; thus a “negative” of the original mesostructure is generated.^[123–127] The need for an inorganic template, which has to be removed by selective etching after the impregnation with the carbonic phase, can be considered as a possible drawback of this technique.

The soft-templating method involves an organic-organic self-assembly process of a

2.3. MESOPOROUS STRUCTURES IN CONFINED ENVIRONMENTS

performed oligomeric resol precursor and a structure directing agent.^[74,121,122,128] The resulting powders show BET surface areas of up to 1500 m²/g and very high thermal stabilities of up to 1400 °C. The mesopore arrangements found for these powders are similar to those known from mesoporous silica: two-dimensional hexagonal (p6mm), three-dimensional bicontinuous ($Ia\bar{3}d$), body centered cubic ($Fm\bar{3}m$), and lamellar.

Despite their novelty, there have been already several reports on the synthesis of OMCs in confined environments. In one of the first reports, the self-assembly of a block-copolymer (polystyrene-*co*-poly(4-vinylpyridine), PS-PVP) and carbohydrates within AAO channels was studied.^[129] After the carbonization at a temperature above 460 °C, the templating copolymer was removed and porous structures were obtained. SEM micrographs of the carbon structures obtained after dissolving the alumina support showed that not completely filled filaments, but tubular structures were synthesized. TEM images of these tubes revealed that the tube wall material had a thickness of about 15 nm and that it was nanoporous. An average pore size of 16 nm was determined by nitrogen sorption.

Zheng et al.^[130] produced core-shell mesoporous carbon nanofibers by a self-assembly process using an oligomeric resol precursor and Pluronic F127 as template. After carbonization at 700 °C, individual fibers could be obtained by removing the alumina template with hydrofluoric acid. TEM micrographs of fibers synthesized in 80 nm alumina pores revealed a core-shell structure with parallel aligned mesopores. Fibers dissolved from larger mesopores (300 nm in average) also showed a core-shell structure, but with differently ordered mesopore systems in the shell and in the inner core. The outer shell of the nanofibers appears to be composed of parallel mesopores perpendicular to the fiber main axis with pore diameters of 12

nm. This outer shell could be removed by sonification of the fibers. SEM and TEM micrographs of the remaining fiber core then revealed a circular orientation of the mesopore system. No reflections in the wide-angle region were found, thus only amorphous carbon phases were obtained. This is also supported by corresponding Raman data.

Steinhart et al.^[131] synthesized mesoporous carbon fibers by solvent-free infiltration of a precursor mixture into porous alumina and carbonization at moderate temperatures of 500 °C. The synthesis started from a solution containing phloroglucinol as the carbon precursor, formaldehyde, dilute HCl in an ethanol/water mixture, and Pluronic F127 as the SDA. After stirring this solution for some time a phase separation was observed. The polymer-rich phase was further dried and then spread onto AAO substrates with pore sizes of 400 nm and 60 nm, respectively. By removing the solvents before the casting process, macroscopic phase separation as well as hydrodynamic instabilities could be avoided. After crosslinking of the phloroglucinol molecules and carbonization at 500 °C, the PEO microdomains are converted to amorphous carbon and thus mesoporous carbon filaments were obtained. These filaments were dissolved from the alumina matrix and probed for their mesostructure by electron microscopy. While for the filaments synthesized within the 400 nm pores a mesopore orientation corresponding to a bulk phase was found, the 60 nm filaments showed confinement effects and the formation of a helical mesophase is reported.

As mentioned above, mesoporous carbon powders and films can be synthesized from resol precursors and block-copolymer surfactants.^[121] This synthesis concept has been successfully adapted for the synthesis of free-standing OMC nanofibers on a silicon wafer.^[132,133] In a first step, the carbon fibers were synthesized on a sili-

2.3. MESOPOROUS STRUCTURES IN CONFINED ENVIRONMENTS

con wafer within AAO pores. This was possible due to the strong adherence of the AAO membrane to the silicon wafer after immersing both into the precursor sol. After carbonization at 600 °C, the AAO membrane was dissolved. The removal of the alumina usually leads to an entanglement of the fibers during the following drying process; the authors prevented this entanglement by using supercritical carbon dioxide that reduces the liquid-gas interface during the drying process. Pluronic P123 templated nanostructures were obtained in the form of mesostructured ribbons, which show circular mesochannels. Using F127 as the SDA, filaments with the circular hexagonal orientation of the mesopore system were obtained as shown with TEM micrographs. Some fibers feature columnar oriented mesochannels in the fiber center that are wrapped by the circular phase. The OMC filaments were further characterized with respect to their conductive properties using conductive atomic force microscopy (C-AFM). That way it is possible to measure the conductivity of individual fibers and thereby prove that they are conductive over the whole fiber length. The fibers showed linear I-V characteristics; the resistivity of single fibers was found to be in the remarkably low range of 0.014-0.018 Ωm .

The possible shrinkage of the mesophase system upon the calcination/carbonization process is a common challenge, as the mesoporous silica/carbon fibers can delaminate from the alumina wall and thus create large voids within the composite membrane. Cao and coworkers^[134] found that this shrinkage does not necessarily occur for carbon phases synthesized within hard templates such as AAO or SiO_2 colloidal crystals due to a 'new restriction effect'. The evaluation of TEM micrographs of carbon fibers synthesized within 90 nm AAO pores and carbonized at 350 °C showed an average pore diameter of 11 nm and an average wall thickness of 5 nm. A remarkable increase in pore size to 15 nm was found for samples carbonized at

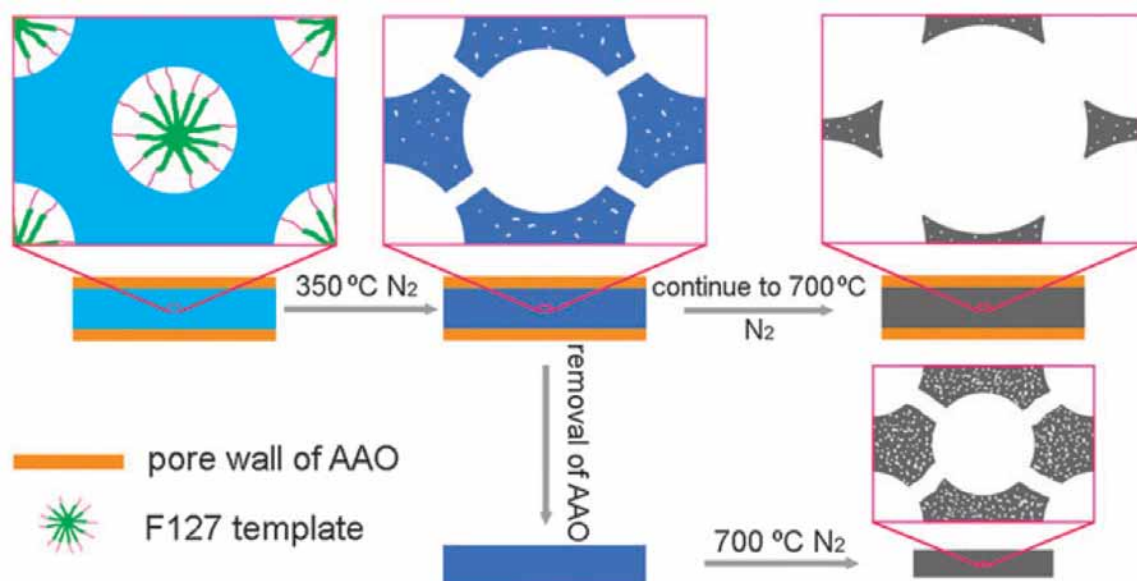


Figure 2.21 — Schematic illustration of the restriction effect of AAO regarding the shrinkage of mesoporous polymer during carbonization.

700 °C; at the same time, the mean thickness of the wall material was decreased to about 2 nm. Thus, the diameter of the fibers stayed constant for both samples and fit the diameter of the templating anopores (Figure 2.21). These findings from electron microscopy were further confirmed by data obtained by nitrogen sorption experiments.

OMC filaments have also been synthesized by hard templating. Thus, the replication of Fe-containing silica mesopores within AAO channels by carbon material was demonstrated.^[135] In a first step, the silica mesopore system was synthesized by an EISA process of a precursor solution containing TEOS, Pluronic P123 and Fe(NO)₃ as the iron source. SAXS measurements and TEM micrographs showed the formation of the 2D hexagonal circular phase. After surfactant removal by calcination, the iron centers were reduced in a hydrogen atmosphere at 750 °C. This com-

2.3. MESOPOROUS STRUCTURES IN CONFINED ENVIRONMENTS

posite was then used as the template for carbon incorporation from a CO₂/xylene mixture using a supercritical fluid deposition technique. By dissolving the silica and alumina host matrices, pure carbon replica were obtained. TEM micrographs of these replicas perfectly resemble the original silica mesostructures (Figure 2.22). The graphitic nature of the carbon filaments was demonstrated by Raman measurements showing the characteristic vibrations of sp²-type carbon.

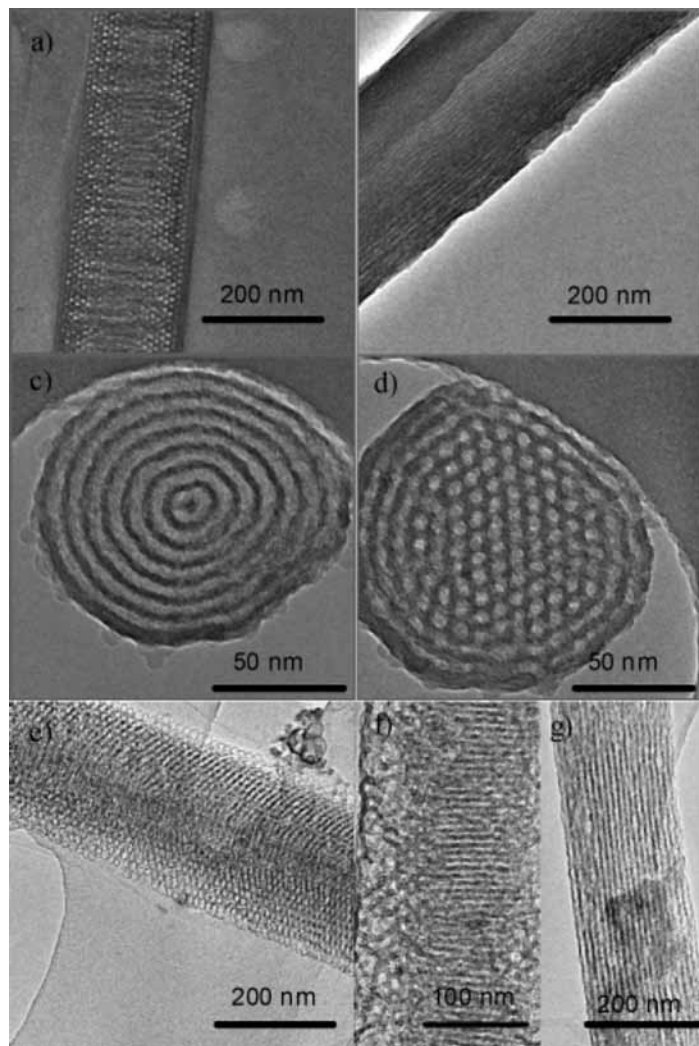


Figure 2.22 — TEM images of the Fe-containing silica mesostructured nanofilaments with (a) circular and (b) columnar channels; (c) and (d) are the corresponding TEM images of the filaments inside the pores of an AAO, and TEM images of isolated carbon replicas with (e) and (f) circular, and (g) columnar mesopores. Reprint from [135].

2.3.4 Inclusion chemistry

Oriented silica mesophases embedded in AAO matrices make ideal template structures for the synthesis of nanostructures via inclusion chemistry. Due to the long-range order, high aspect ratios, and tunable pore diameters of the porous host systems, the synthesis of nanowires is the most obvious implementation of this concept. As already discussed above, Stucky and coworkers successfully replicated the structure of helical mesophases by the electrodeposition of silver.^[95] Subsequently both the alumina and silica mold were dissolved and thus the respective nanowires could be obtained. The free nanowires perfectly resembled the orientation of the original silica mesophase as demonstrated by TEM micrographs (Fig. 2.13). In that particular study, no columnar mesophase and therefore no straight nanowires were obtained. By using the recently published mesopore alignment assisted by the addition of lithium chloride salt (see above), 2D hexagonal columnar structures of Pluronic P123 templated mesopores can be synthesized.^[103] Thus this approach should open up the possibility of synthesizing straight, non curled nanowires. This concept was employed in a recent study for the synthesis of silver, copper, and tellurium nanowires.^[136] To obtain the highest possible fraction of the columnar phase over the circular silica phase, the synthesis conditions were further optimized with respect to the temperature and humidity conditions during the EISA process. As already reported earlier, both the temperature and the humidity present during EISA have a strong influence on the phase formation. The authors found that the highest fraction of the columnar phase can be obtained for samples synthesized at constantly high humidities (> 70 % r.h.) and temperatures above 29 °C. After surfactant removal by calcination, the membranes were sputtered on one side with a thin layer of gold acting as the electrode for the electrodeposition of the wires.

Both the concentration of the electrolyte and the potential used for the electrodeposition were observed to have a strong influence on the growth of the nanowires. Due to the high aspect ratio of the mesopore system, diffusion of the respective ions to the electrode surface is critical. Defects such as cracks, voids, or even empty anopore channels are expected to show a faster mass transport of the precursor species than in the mesopore system. Therefore high electrolyte concentrations and low deposition potentials yielded the best filling rates. Consequently, the deposition of tellurium, which had to be carried out from a highly dilute electrolyte solution, showed only poor filling rates. Additionally, due to the long deposition time in highly acidic media, the orientation of the underlying mesopore system was strongly disturbed. Copper and silver nanowires, electrodeposited from much more concentrated solutions, showed drastically better filling rates. Though both elements were deposited from comparably concentrated electrolytes and by using the same deposition potentials, filling rates appeared to be higher for the copper system (see Fig. 2.23).

Plan view TEM micrographs of the wires embedded within the AAO/silica mold system still show the hexagonal arrangement of the original silica mesophase. To obtain information on the long range order of both the nanowires and the original mesopore system, the alumina mold was selectively dissolved; thus composite silica/nanowire filaments were obtained. TEM micrographs of these filaments showed occasional defects in the arrangement of the mesopores. Besides the hexagonal columnar phase as the main phase, domain boundaries between the hexagonal columnar and the hexagonal circular mesophase were found in TEM images. Wires grown in regions exhibiting the hexagonal columnar phase illustrate that in such 'defect-regions' the porous system is twisted, while leaving the hexagonal short-

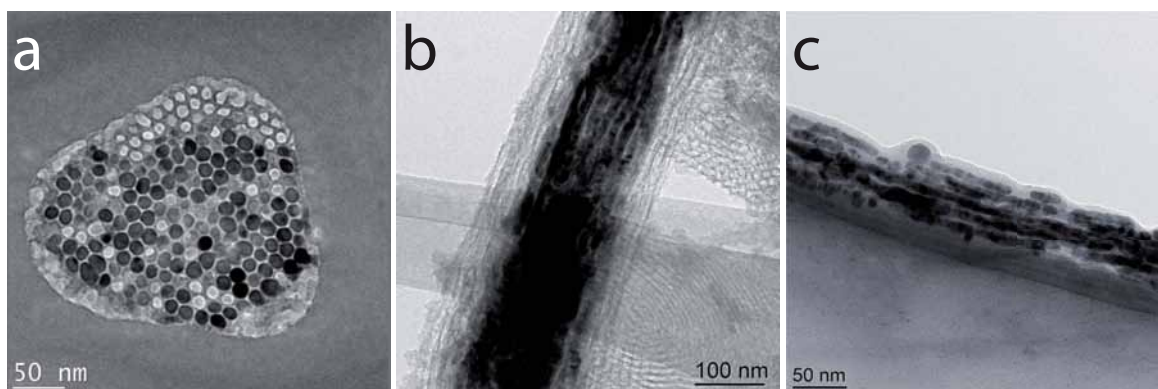


Figure 2.23 — TEM micrographs of nanowires obtained from electrochemical deposition into silica/AAO composites. a) Copper nanowires recorded in plan view. The wires reproduce the original hexagonal arrangement of the underlying mesostructure. b) Image of Cu wires in an isolated silica filament. c) Bundles of free silver nanowires obtained by the total dissolution of the host matrices.

range order intact. This tortuosity was already anticipated from plan-view images. The presence of domain boundaries along the length of the anopore host is not surprising given the synthesis mechanism with multiple nucleation sites discussed above.^[102] To finally obtain free standing wires, both the alumina and the silica matrix had to be dissolved. This was done in hot sodium hydroxide solution; unfortunately, only the silver wires survived this treatment while the thin copper wires were dissolved as well. The straight polycrystalline wires observed in the TEM were always found to be bundled; this is explained by the presence of interconnecting micropores within the silica mold system, a feature well known for block-copolymer-templated mesoporous silica.^[137]

The successful inclusion of noble metal (Pt, Au, Pd) and semiconductor (Ge) nanowires into silica mesophases synthesized within AAO channels can also be accomplished by wet chemical impregnation.^[138] Platinum nanowires have been synthe-

sized in the channels of calcined AAO/silica composites by a repeated impregnation with $\text{Pt}(\text{NH}_3)\text{Cl}_2$ followed by a hydrogen reduction step. Plan-view TEM images of the AAO/silica/Pt system show that the original hexagonal order of the initial mesophase is retained, while the mean diameter of the wires has shrunk to about 5 nm (compared to about 8 nm initial pore diameter). Images of silica/Pt filaments show well-defined nanowires that extend to several hundreds of nanometers. They are composed of small segments suggesting a chainlike morphology, which is commonly observed for metal nanostructures prepared by wet chemical impregnation.^[139] In a related strategy, gold nanostructures could be prepared in previously functionalized columnar mesopores. For this purpose, aminopropyltriethoxysilane (APTES) was grafted into the calcined composite membranes. After the impregnation with $\text{H}[\text{AuCl}_4]$ as gold precursor, the final reduction step was carried out in air, upon which the membranes changed color to violet. Besides the impregnation of metal precursors into calcined samples, treatment of the uncalcined mesophases with a Palladium precursor containing ethanol/water solution was described, resulting in simultaneous extraction of the template, and one-step deposition and reduction of the metal precursor within the silica mesopores during impregnation. This mild reduction method resulted in a higher loading of the mesophase with the respective metal ions as compared to gold reduction in the calcined mesopore system. Additionally, the authors report that no or only little shrinkage of the mesopore system was observed.

The three aforementioned methods all include a solvent-based nucleation and growth mechanism. To facilitate mass transfer and thus enhance the continuity of the nanowires, a solvent-assisted supercritical fluid (SCF) deposition of germanium nanowires was studied. This technique is reported to allow the growth of

continuous semiconductor nanostructures in SBA materials.^[140] During the deposition step, the orientation of the mesophase system is preserved and Ge nanowires with 8 nm were obtained. In some cases, the formation of Ge nanotubes was also observed, resulting from germanium deposition only at the pore walls.

2.3.5 Separation/release

In addition to the utilization of the mesoporous composite membranes for the templated synthesis of nanowires^[95,109,135,136,138] another evident application for those composites is the use as separation membranes. For those studies, permeable mesostructures such as the hexagonal columnar phase or bicontinuous cubic phases are essential. A significant number of such experiments was reported by the group of N. Teramae, and composite membranes including the CTAB-templated columnar hexagonal phase were employed.^[96]

In a detailed permeation study, chromatographic experiments were carried out using a non-calcined CTAB-templated composite membrane as column.^[141] A mixture of toluene and phenol was separated in a chromatographic experiment, where the composite membrane was used as column and the mobile phase was n-hexane at a constant flow rate of 0.2 mL/minute (Figure 13). The retention time of phenol was found to be greater than that of toluene, which was attributed to stronger interactions of phenol with the silica-surfactant composite due to dipole interactions with the ionic interface at the silica pore wall.

Additional permeation flux measurements were done using a U-tube, the feed half-cell containing the solute (phenol, benzene sulfonate, or benzene disulfonate) in

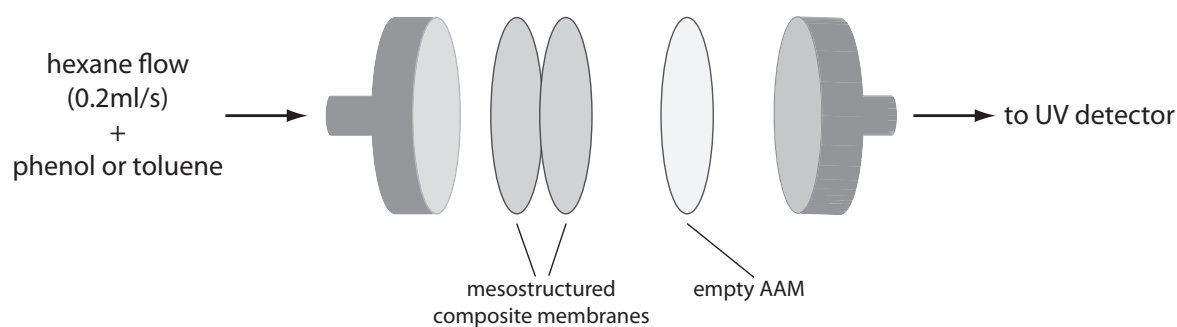


Figure 2.24 — Scheme of the chromatography experiment (after [141]). Two porous alumina membranes were used to stabilize the composite membrane. The composite membrane was used with the surfactant template still present.

water or an ethanol-water mixture, the permeation half-cell containing only solvent. Transport through the membrane was measured by monitoring the UV absorption as a function of time in the permeation half-cell. If water was used as solvent, the transport through the membrane was fast for phenol and less pronounced for the sulfonate-molecules in agreement with the molecular charge. The authors concluded from partitioning experiments that the higher charged sulfonates are adsorbed within the composite membrane, thus showing less pronounced transport through the membrane, while phenol shows high permeation flux. If an ethanol-water mixture was used as a solvent and the ethanol content was successively increased, the permeation of phenol decreased while the permeation of the charged sulfonates increased. Moreover, the interactions with the composite membrane are strongly influenced by the choice of solvent.

A mechanism for the incorporation of charged dye molecules into non-calcined CTAB-templated composite membranes was proposed by the same authors (Figure 2.25).^[142] The dyes were extracted from aqueous solutions containing various types and concentrations of inorganic salts. The extraction of cationic Rhodamine

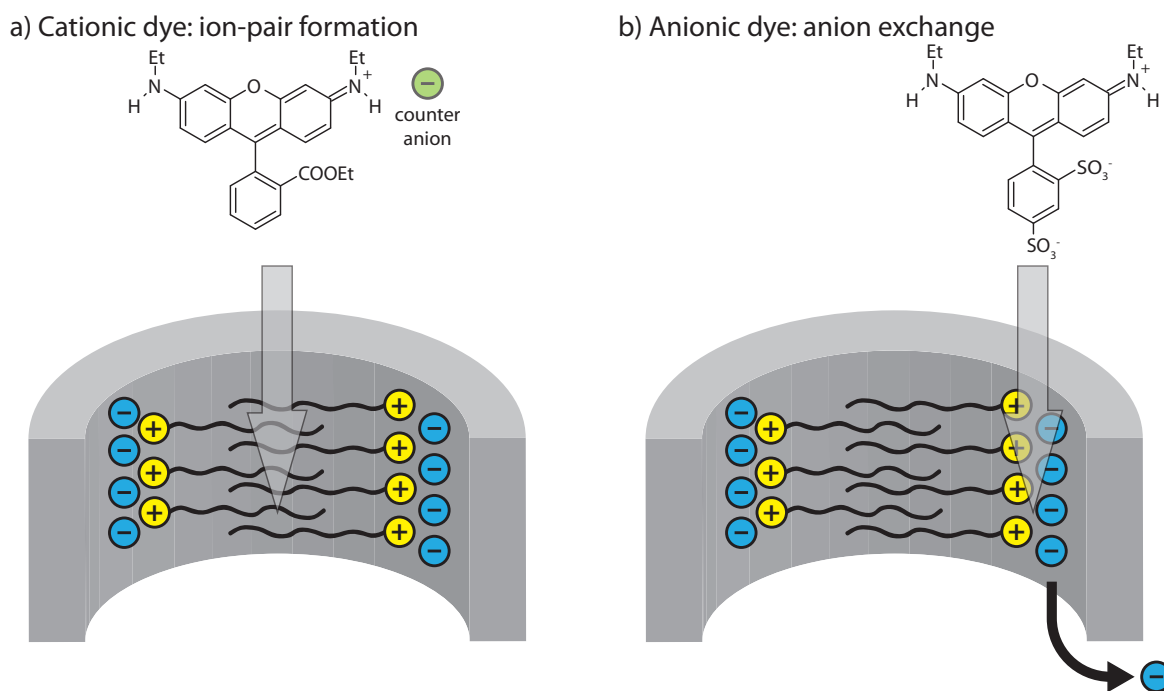


Figure 2.25 — Illustration of the proposed mechanism (after [142]) for incorporation of dye molecules into a silica mesophase containing cationic template. One possibility is the incorporation into hydrophobic areas after ion-pair matching. Another possibility is exchange with the template counter ions

6G was facilitated by inorganic salt addition. The strongest effect was observed for sodium perchlorate followed by sodium nitrate and bromide, the smallest effect was observed for sodium chloride, which is consistent with the Hofmeister series of salts.^[143] The Hofmeister series of salts reflects the dehydration energy of anions, chloride having the highest energy and perchlorate having the lowest. Thus, the authors propose an ion-pair extraction process for the cationic dye molecules, involving counter ion matching and incorporation into the hydrophobic part of the micelles. In contrast, the effect of dye incorporation into the membrane is inhibited by the addition of inorganic salt for anionic sulforhodamine B according to the Hofmeister series. The authors conclude that the anionic dye molecule is extracted from aqueous solution via a different mechanism by replacing the bromide counter ion of CTAB at the silica-surfactant interface. In a related study, the local environment of neutral and anionic coumarin dyes incorporated in non-calcined CTAB-templated composite membranes was investigated by time-resolved fluorescence spectroscopy.^[144]

Furthermore, permeation measurements of tris(2,2'-bipyridyl)ruthenium through a composite membrane after the one-step extraction of the ionic surfactant and simultaneous modification of the silica with alkylsilanes^[145] were carried out.^[146] The transport of the ruthenium complex through the membrane was recorded by time-dependent absorption spectroscopy of a feed and a permeate solution. Diffusion coefficients estimated from observed lag-times were compared for silanes with different alkyl chain lengths and for various solvents. The lag-time is the time before the transport of the ruthenium complex into the permeate solution shows linear behavior. Diffusion coefficients for silanes having short alkyl chains (methyl- and butyl-groups) were several orders of magnitude smaller than in the respective

bulk solutions, when ethanol was used as solvent. Diffusion in mesopores that were modified with long alkyl chains (dedecyl-groups) was about two orders of magnitude smaller than in bulk ethanol solution. This behavior is attributed to stronger hydrogen-bonding interactions between the solvent molecules in the cavity of the mesopores slowing down the molecular diffusion. If the alkyl chains are very long, the authors assume that less solvent molecules are present in the mesopore channels and diffusion can again be faster.

Gas permeation measurements were performed by another group investigating composite membranes composed of anodic alumina and Brij 56-templated mesoporous silica prepared by dip-coating of an EISA precursor solution.^[99] The synthesis procedure was previously reported for thin film preparation, resulting in a bicontinuous cubic phase. However, in the mesoporous/AAO composite, silica fibers with circular hexagonal and cubic structures were observed with transmission electron microscopy. Powder X-ray diffraction patterns were obtained from as-synthesized membranes showing peaks that were attributed to a surface layer formed on the planar membrane surface and assigned to a mixture of lamellar and Ia3d cubic phases. After ethanol extraction of the surfactant, no peaks were observed in powder diffraction anymore, but some of the circular hexagonal and cubic mesoporous material was still observed by TEM imaging. This observation shows that careful investigation of the composite membrane before and after dilution experiments is crucial, since the structural features might be destroyed during the experiment.

Gas permeation measurements were performed with the extracted composite material. The transport of nitrogen, helium, and propane through the membranes was investigated and compared with the permeation properties of commercially

available separation membranes having 200 nm, 20 nm, 10 nm, and 5 nm nominal pore size. Those membranes are generally composed of a large pore alumina support and a thin layer of material exhibiting the smaller pore sizes. The permeance and permselectivity of the membranes were compared; the permselectivity being represented by the ratio of helium to nitrogen permeance or propane to nitrogen permeance, respectively. It was found that the effective pore size of the composite membranes depends on the number of dip-coating cycles, reaching consistency with the expected pore size after four cycles for the Brij 56-templated mesoporous material according to TEM and powder X-ray diffraction experiments. The permselectivity for a four-time dip-coated membrane was much higher than for commercially available membranes with nominally 5 nm pore size, which was attributed to the narrow pore size distribution and absence of pinhole defects in the mesoporous material.

As indicated above, the potential of the composite membranes as molecular separators is promising. However, in order to arrive at clear conclusions regarding the relationship between separation behavior and mesopore morphology, subsequent analysis of the structural and morphological nature and quality of the composite is essential.

The influence of morphological features on molecular diffusion was addressed in a recent study.^[147,148] Thus, drug uptake and release into and from mesoporous silica-anodic alumina composite membranes was investigated and compared with drug release properties of SBA-15 powder samples having fibrous (20 – 30 μm fiber-length) or microspherical (4.5 – 7 μm diameter) morphology, respectively.^[147] The larger diameter of the columnar mesopores is due to the swelling effect of lithium chloride, which was added to induce the phase shift.^[103] Three different compos-

2.3. MESOPOROUS STRUCTURES IN CONFINED ENVIRONMENTS

ite systems were employed: one synthesized with CTAB having columnar pore-alignment and 4.5 nm pore diameter (i), the other two synthesized with Pluronic P123 as surfactant and having circular hexagonal structure and 7 nm pore diameter (ii), or exhibiting a columnar hexagonal main phase (iii) with 9 nm pore diameter, respectively. In this study, the antibiotic vancomycin was introduced into the calcined samples through immersion in drug-containing simulated body fluid.

The CTAB-synthesized sample (i) with pore dimensions comparable to those of the vancomycin molecule was found to adsorb 30.5 mg/g (normalized to the absolute mass of the composite membrane). The drug-loaded composites showed pore-blocking in nitrogen sorption experiments. This is attributed to either vancomycin being located in the outer volume segment of the sample, or due to the deposition of hydroxyapatite-precursors derived from interactions of the silica material with the SBF solvent. The hypothesis that the drug molecules are mainly located in the outer volume segment of the host material is supported by the finding that drug-release is much faster in the CTAB-synthesized sample than in the columnar sample synthesized with P123, despite the larger pore diameters of the P123-templated material. However, the presence of inorganic precipitate was found in all samples by scanning electron microscopy combined with energy dispersive X-Ray spectroscopy (EDX) after exposure to both the dissolved vancomycin or the simulated body fluid alone. Assuming the same influence of the inorganic species on the molecule uptake and release, the authors therefore conclude that differences between the samples can be attributed to the different structural and morphological features alone.

The circular sample synthesized with Pluronic P123 adsorbs only 11 mg/g of the maximum possible amount of vancomycin, which is lower than the relative amount

adsorbed by the empty AAO alone. The pore size distribution derived from sorption measurements before and after drug-uptake is the same, indicating that the molecules are not adsorbed into the inner pores but rather in small quantities at the mouths of the pores. This is also supported by the fact that the circularly structured mesoporous material shows the fastest drug delivery of all studied AAO-composites.

The P123-synthesized composite material having mainly columnar hexagonal structure and a circular hexagonal side-phase (iii) shows with 49.9 mg/g the highest uptake of vancomycin. The pore size distributions from measurements before and after drug-uptake indicate that the vancomycin is located in the columnar pores, resulting in the longest diffusion paths and slowest release in this host.

The authors conclude that pore diameter, pore tortuosity and length, and the accessibility of the pore entrance are critical factors for drug-uptake and release kinetics.

2.3.6 Summary

Great progress has been made in the recent years towards understanding the structure formation and the synthesis process. Although not all questions are cleared yet, a set of parameters for optimization of the quality of the composite membranes is available, ranging from the choice of the right template for the envisioned purpose and optimal synthesis conditions^[90,93,95,100–102] all through the eventual utilization of additives.^[103]

From the studies discussed above it is clear that anodic alumina - mesoporous ma-

2.3. MESOPOROUS STRUCTURES IN CONFINED ENVIRONMENTS

terial composite membranes are of great interest for the design of complex hierarchical nanostructures. They offer a largely independent control of pore size, pore topology, pore orientation, molecular functionalization and possibly also pore wall composition. Potential functionality and applications include molecular separators,^[96,99,141,142,146,147] or host materials for the inclusion of conducting or semi-conducting nanostructures.^[92,95,109,135,136,138] For example, composite membranes were found to exhibit superior permselectivity than commercially available membrane systems in gas permeation experiments.^[99] Furthermore, as compared to conventional mesoporous powder systems, higher control over the structural and morphological features of the pore system can be achieved in composite membranes, enabling greater tunability of the materials properties, for instance regarding the host-guest interactions in potential drug delivery systems.^[147]

One-dimensional Nanostructures

Contents

3.1 Introduction	73
3.2 Nanowire synthesis	74
3.2.1 Spontaneous growth	75
3.2.2 Template-based synthesis	80
3.2.3 Electrospinning and lithography	84
3.3 General Properties of Nanowires	85

3.1 Introduction

Nanoscale objects can be grouped according to their dimensionality (see chapter 1). One-dimensional nanostructures can be defined as systems in which the free mean path of charge carriers is larger in one direction than in the two other spatial dimensions. Thus, the carriers are confined for transport phenomena only in one dimension as it is the case for nanowires, nanotubes, and related materials.^[149]

Nanotubes are defined as hollow nanowires, whose walls have a thickness of less

than a micron. Nanowires and -tubes can be synthesized in a variety of ways and both show very interesting properties; nevertheless, nanotubes are not within the scope of this thesis and will therefore not be discussed here.

Nanowires already have a long history in science; in 2007, the fiftieth anniversary of silicon-nanowire research was commemorated.^[150] Over the times, different terms – nanowiskers and nanowires – have been used, both referring to the same 1-d nanostructures. In modern literature, the latter one is used almost exclusively. There is no clear definition of the difference between nanowires and nanowiskers on the one side and nanorods on the other side; generally speaking, wires have a larger aspect ratio than rods.

The synthesis, properties, and applications of 1-d nanostructures, be it nanowires, -rods, or -tubes, is a field of highly active research.^[151] With electronic circuits becoming smaller and smaller, the size of electronic components – if the trends continues – will reach atomic dimensions within the next two decades. Thus, a lot of effort has to be put into the synthesis, characterization, and properties of such small structures. Besides their role in modern semiconductor physics, nanowires are also to be expected to play an important role in optical, electrochemical, and electromechanical devices.^[152–154]

3.2 Nanowire synthesis

Since there is a long tradition in nanowire research, a large number of synthesis strategies has been developed. These different techniques can be grouped into four categories:^[2]

1. Spontaneous growth
 - a) Vapor (or solution)-liquid-solid growth
 - b) Evaporation (or dissolution)-condensation
 - c) Stress-induced recrystallization
2. Template-based synthesis
 - a) Electroplating and electrophoretic deposition
 - b) Colloid dispersion, melt, or solution filling
 - c) Conversion with chemical reaction
3. Electrospinning
4. Lithography

The first three methods – spontaneous growth, template based synthesis, and electrospinning – are bottom-up approaches, with access to the vast number of chemical synthesis methods that can be applied. The last item, lithography, is a classical top-down approach.

3.2.1 Spontaneous growth

The spontaneous growth technique is based on the reduction of the Gibbs free energy. Some solids naturally crystallize in an anisotropic crystal structure. If growth only occurs along the longitudinal direction of a crystallite and in the other directions only little growth occurs, nanowires or -rods may be formed. As spontaneous growth involves a crystallization process, defects and impurities may have a strong influence on the morphology of the final products. There are several mechanisms known that result in an anisotropic growth:^[2]

1. A different growth rate of different crystal facets. In silicon, the growth rate of {110} facets is higher than that of {111} facets.
2. Presence of imperfections in a specific crystal direction.
3. Preferential accumulation of impurities on specific facets.

Spontaneous growth is a widely used method for the synthesis of nanowires. In a pioneering paper, Ellis and Wagner reported on the synthesis of silicon nanowires by vapor-liquid-solid (VLS) growth.^[155] Although the interest in this work faded in the first decades after the original publication, research on the VLS process gained a lot of momentum back in the '90 of the last century. Since then, the VLS (and the related solution-liquid-solid growth, SLS) method became the by far most widely used method for the growth of semiconductor nanowires. This method allows the synthesis of highly crystalline semiconductor (Si, Ge, etc.) nanowires with several micrometers in length and diameters on the nanometer scale. The VLS process always involves a catalyst in the form of a liquid droplet in the presence of vapor precursor. The classic (and to date best studied) example is the growth of silicon nanowires from a gold catalyst and silane (SiH_4) gas. The VLS process can be best understood with the help of phase diagrams. In general, a phase diagram depicts phases and their compositions in mixtures depending on the relative concentrations and temperature in thermodynamic equilibrium. The phase diagram of the binary system gold and silicon is depicted in Figure 3.1 (left). In a first step, a substrate (usually a silicon wafer) is coated with a thin layer of gold. This substrate is then annealed above the temperature of the eutectic point E (363 °C). This causes the formation of small, liquid gold droplets, as the gold and silicon mix until the eutectic composition is reached. During the whole (dynamic equilibrium) growth process, this composition is constant. Now the silicon precursor is introduced in

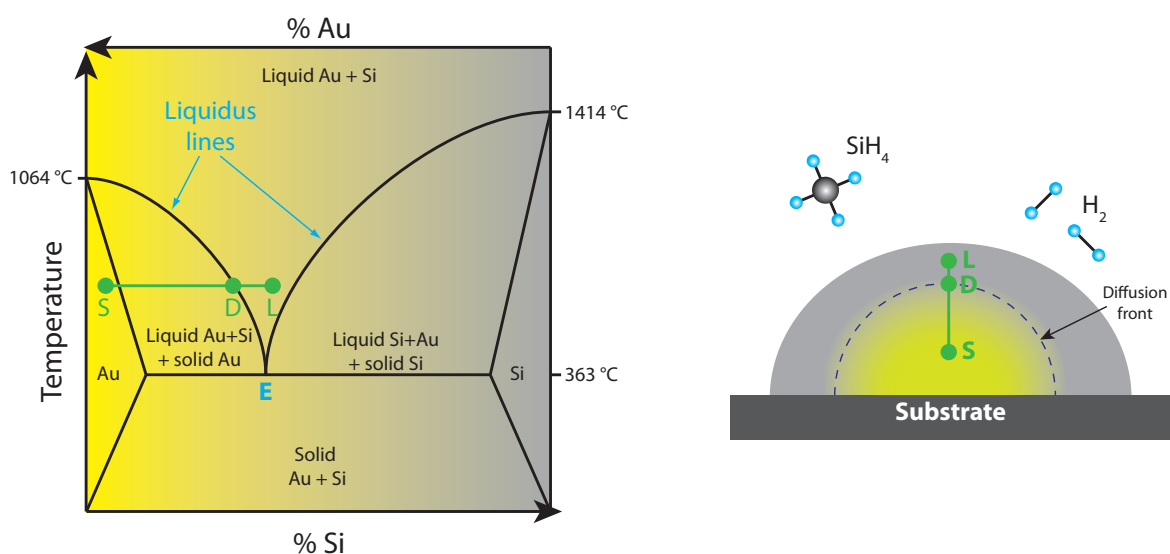


Figure 3.1 — *Left*: Binary phase diagram of Au/Si. The green line marks the evolution of the concentration inside the droplet during nucleation. Point *L* depicts the zone where the concentration is high enough to form a liquid droplet. Point *D* marks the crossing of the liquidus line and point *S* denotes the zone in which gold is still solid. *Right*: Gold droplet in the nucleation process. The impinging silane is catalytically decomposed on the droplet surface. The increasing silicon concentration leads to a diffusion to the center. The volume outside the diffusion front is in a liquid state. Adapted from [156]

vaporized form. The precursor is preferentially decomposed on the catalyst (gold) surface and the silicon atoms now diffuse into the gold droplet. As the composition of the droplet always has to be constant, the droplet gets supersaturated with silicon; thus, the silicon starts to precipitate at the solid-liquid interface. As this interface is always located at the bottom of the droplet, one-dimensional growth is achieved which results in the formation of nanowires. Depending on the growth conditions, the resulting nanowires can be obtained in single-crystalline, polycrystalline, or amorphous form.

Because of the growth process, nanowires prepared by vapor-liquid-solid growth always usually carry their catalyst on top (see Fig. 3.2). The size of the nanowires is mainly determined by the droplet size; however, very small droplets will show growth in all directions because of an increased surface curvature and therefore higher solubility of the precursor within the droplet.^[2] Small amounts of the catalyst are often found to be decorating the nanowire surface or even being incorporated into the wire causing defects. Especially in the case of gold this is an important issue, as Au is a deep level impurity in Si and Ge that significantly degrades the carrier mobility and causes fast nonradiative electron-hole pair recombination.^[157,158] Therefore, different catalysts than Au are often desired. The incorporation of catalyst atoms into the wire core can also have beneficial consequences. By controlling the amount of the incorporated atoms, it is possible to dope the nanowires and thus tune their electronic band-gap. Additionally, if the catalyst is slowly consumed the droplet size is reducing with on-going wire growth; thereby, nanowires with a conical shape can be grown.

VLS growth is not limited by the type of the substrate, precursor and the catalyst used; as long as the phase diagram shows a eutectic point and the precursor

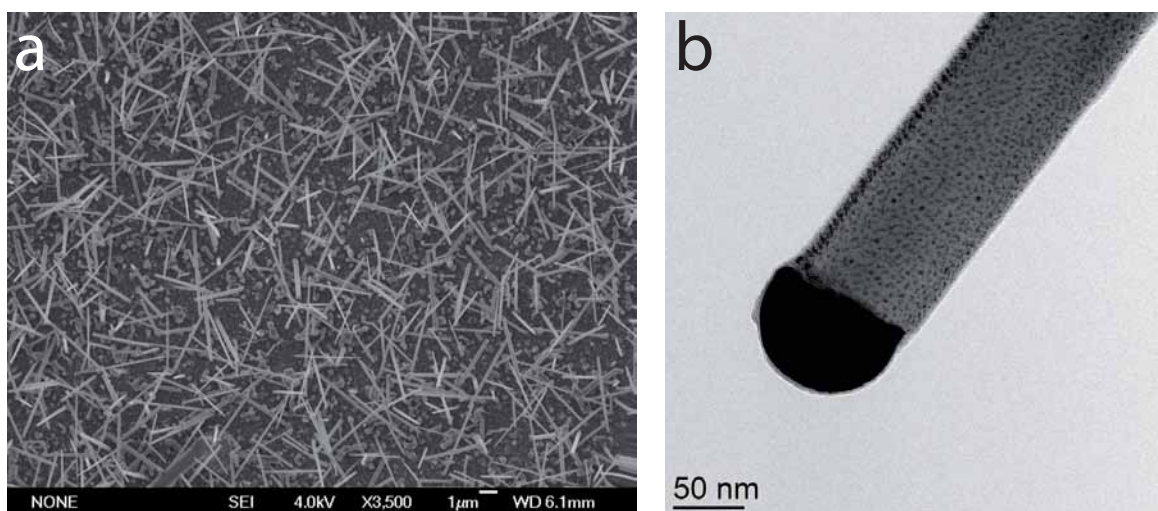


Figure 3.2 — SEM (a) and TEM (b) micrographs of silicon nanowires grown by a VLS process. The wires were grown on the top surface of a gold sputtered AAO/SiO₂ surface. The dark tip of the wire in the TEM image represents the gold catalyst; the small dark spots are traces of gold decorating the nanowire surface.

sor is preferentially decomposed at the catalyst surface, one-dimensional growth might be achieved. Besides the Si/Au system, a variety of other systems have been successfully used for VLS growth. Si nanowires can also be grown using an iron catalyst.^[159] Germanium nanowires can be grown using indium and bismuth as catalysts.^[157,160] A broad range of single-crystalline multicomponent semiconductor nanowires (GaAs, CdSe, SiGe, and others) have been prepared in the group of Charles Lieber.^[161] A combination of VLS and template growth has also been demonstrated by growing silicon nanowires within anodic alumina pores.^[20,162,163]

To date, only a few different materials, mainly oxides, could be synthesized in the form of nanowires by evaporation (or dissolution)-condensation processes. The successful synthesis of single-crystalline semiconducting oxide (ZnO, SnO₂, In₂O₃, CdO) nanobelts has been shown by the group of Zhong Lin Wang.^[164] The syn-

thesis was based on thermal evaporation of the respective oxide powders under controlled conditions. They obtained wires with rectangle-like cross sections (typical widths of 30 to 300 nanometers), width-to-thickness ratios of 5 to 10, and up to a few millimeters length. Tin oxide nanorods could also be synthesized by a conversion of amorphous SnO₂ nanoparticles at elevated temperatures.^[165] The synthesis of elemental nanowires has been achieved by the thermal evaporation of silicon monoxide in a reducing hydrogen atmosphere.^[166]

3.2.2 Template-based synthesis

A template-based approach for the synthesis of nanowires and nanostructures in general is probably the most versatile technique to date. Quite a few different template materials have been successfully employed for this purpose. Most commonly, porous anodic alumina and track-etched polycarbonate substrates are used, but also other materials such as mesoporous silicates, nanochannel array glass, and even carbon nanotubes have been demonstrated as templates.

The beauty of templates-based approaches for the synthesis of nanostructures is that the resulting objects are always replicas of the original (porous) structures; thus it is possible to specifically tailor those objects regarding their size (diameter, length), morphology, and density. The materials used as the templates have to fulfill certain requirements:

- Compatibility with the processing conditions (e. g., the template should be chemically inert under the synthesis conditions)
- The deposition solution or material must be able to wet the template walls

- For the synthesis of nanowires, it must be possible to start the growth from the bottom of the pores

The most widely employed synthesis strategy in template-based synthesis of nanowires and related materials is probably electrochemical deposition; this has been used extensively during this work, thus the later considerations will focus on this technique. Other strategies used in this context are melt and solution filling, chemical vapor deposition and VLS (see above), and deposition by centrifugation.

The electrochemical deposition process (also called electrodeposition or electroplating) can be understood as a special electrolysis that results in the deposition of a solid material on the electrode surface.^[2] In an electrochemical cell, two electrodes (cathode and anode) are immersed into a solution containing the electrolyte. The anode is connected to the positive part of a power supply and serves as the counter electrode; the cathode is connected to the negative part and serves as the working electrode. If the applied potential exceeds the standard potential E_0 of half-reaction of the element to be deposited, an electrochemical reaction will occur and the respective cations will be reduced to their elements at the cathode. In an electrochemical system, the electrode potential E is defined by the Nernst equation:

$$E = E_0 + \frac{RT}{z_i F} \ln(a_i) \quad (3.1)$$

E_0 : standard electrode potential

R : universal gas constant

z_i : number of electrons transferred in the cell reaction or half-reaction

F : Faraday constant

a_i : chemical activity of the relevant species

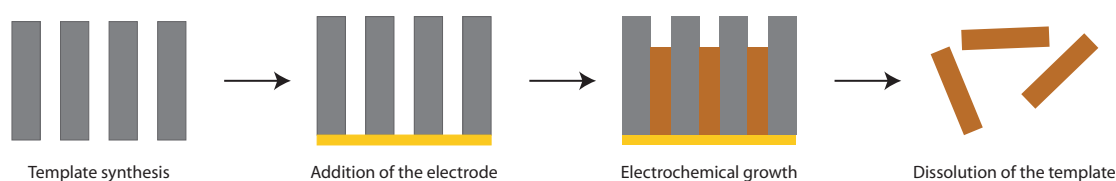


Figure 3.3 — Schematic of the template-based synthesis of nanowires by electrochemical deposition. The main steps (synthesis of a mold system, wire growth, and the eventual dissolution of the host material) are valid for all template-based processes in general.

The basic principle of electrodeposition of nanowires by a template-based approach is shown in Fig. 3.3. In a first step, an appropriate porous mold – commonly in the form of a thin membrane – is synthesized. If necessary, this membrane is coated in a second step with a thin conductive layer that serves as the working electrode. The system is then exposed to a bath containing appropriate electrolytes and an electrical voltage is applied. Now the wires grow until the electric field is switched off again. Finally, the templating material can be dissolved and free wires can be obtained.

Figure 3.4a depicts an SEM micrograph of Nickel nanowires synthesized by electrodeposition into a porous anodic alumina membrane (av. pore diameter 200 nm). One key advantage of electrochemical growth is the possibility to exactly control the length of the resulting wires by monitoring the current over time. Once the electrical field is switched off, the growth process will stop immediately. The growth process itself can be separated into three different stages:

1. Buildup of the double layer and reduction of the first ions close to the electrode surface.
2. Diffusion-controlled growth within the pores.
3. Unconfined growth once the wires reach the pore ends.

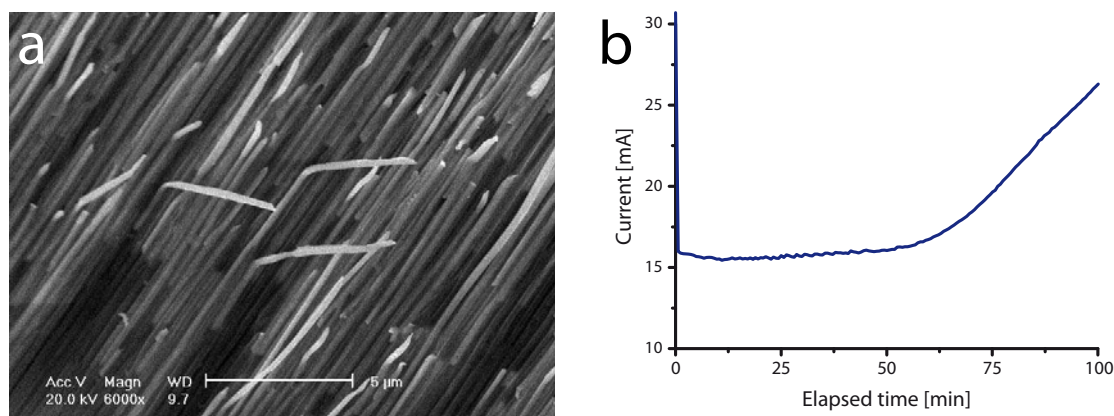


Figure 3.4 — a) SEM micrograph of copper wires prepared by electrodeposition into 200 nm anodic alumina pores. b) depicts the characteristic current behavior for the electrodeposition into nanoporous template. The concentration of CuSO_4 was 0.05 mol/l, the potential applied was 0.01 V.

These three stages can be seen in the graph depicted in Fig. 3.4b. In the beginning, just after the field is on, the current increases to a rather high value. All ions close to the electrode are reduced to Cu. Once they are consumed, new ions have to be transported to the electrode by diffusion through the porous system. This process is slow; thus the electrical current is decreased. As the rate of diffusion is almost constant as long as the wires grow within the pores the currents stays almost constant. Finally the wires reach the end of the pores. The electrochemical reduction is now no longer limited by the diffusion within the pores; additionally, the electrode surface area is increasing. This again leads to an increase in the electrical current. This characteristic behavior can be used to stop the wire growth exactly when the wires reach the end of the pores; thus, completely filled composites can be obtained.

Besides electrodeposition some other methods have been explored to fill the templates. The pores of mesoporous silicas can be filled by electroless reduction meth-



Figure 3.5 — SEM image of mesoporous organosilica filaments templated within anodic alumina pores. The alumina mold has been etched to obtain free filaments.

ods.^[167] Electrophoretic deposition can be used to fill a template material with colloids from colloidal solutions or sols with the help of an electric field.^[168,169] Colloidal solutions or sols can also be used directly for the synthesis of 1d nanostructures.^[107,136] This method was employed for the synthesis of mesostructured silica filaments within AAO pores. Nanowires have also successfully been templated by direct infiltration of porous substrates with melts of the desired materials or adequate precursors.^[170,171]

3.2.3 Electrospinning and lithography

Electrospinning is used mainly for the preparation of polymer nanofibers. Its main advantage is the simplicity combined with low costs. It makes use of the electrostatic repulsions between surface charges to reduce the diameter of a viscoelastic

jet or a glassy filament.^[172] Classic materials that have been employed in electrospinning are – amongst many others – organic polymers such as Nylon-6,6, polyurethane, and polycarbonate.

In contrast to all the aforementioned methods optical lithography (and all other micro- or nanolithographical methods) are a classic top-down techniques. Lithography in general describes a process in which a pattern or structure is replicated onto a given substrate. A large number of different methods, that fall under the generic term lithography, have been developed in the last decades, making it a very versatile method that is widely applied in both research labs and industry.

3.3 General Properties of Nanowires

It is generally accepted that nanoscale objects show remarkably different properties than their bulk counterparts. It is obvious that one-dimensional nanostructures with well-controlled dimension, composition, and crystallinity represent a new class of intriguing systems for the investigation of structure-property relations and related applications. The properties that are attractive and dependent on the nanosized dimensions are: thermal, mechanical, phonon transport, optical, field emission, and electronic (e. g., transport and quantum confinement) properties.^[8]

The investigation of the mechanical properties of nanostructures is essential for the atomic-scale manipulation of these materials in constructing composites with improved mechanical properties. Single crystalline one-dimensional nanostructures that are essentially defect-free tend to be significantly stronger than larger structures.^[173] This can be explained by the reduction in the number of the defect

sites per unit length as a result of decreased lateral dimensions. Measurements of the mechanical properties of one-dimensional nanostructures were performed by attaching the nanowires to STM tips.^[174]

For their implementation as building blocks in nanoelectronic devices, the thermal stability of one-dimensional nanostructures is a critical feature. In general it can be said that the melting point of a nanostructure can be significantly reduced if compared to the corresponding bulk material.^[175] In the case of nanowires, the lowering of the melting point is inversely proportional to the nanowire length. In detail, Wu and Yang found that the melting points of germanium nanowires approach bulk values for long nanowires,^[176] however, if the nanowire lengths were reduced to nanometer scales, the melting point was drastically reduced. This was attributed to a large hysteresis in the melting and recrystallization process. The authors therefore concluded, that the chemical and thermal stability of new devices may be limited.

The electronic properties of nanowires and nanorods are of primary interest nowadays because there is a need to go beyond the traditional microelectronic approaches. As the critical dimensions of an individual device become smaller and smaller, the electron transport properties of their components become an important issue to study. Quantization due to the transverse confinement and the resulting finite level spacing of electronic and phononic states are responsible for some novel effects.^[8]

The electrical transport characteristics of nanowires strongly depend on their diameter. Wires with diameters above the carrier mean free path have similar I-V characteristics as the corresponding bulk materials. But if the wire diameter is decreased below the carrier mean free path, the electron transport properties begin to differ

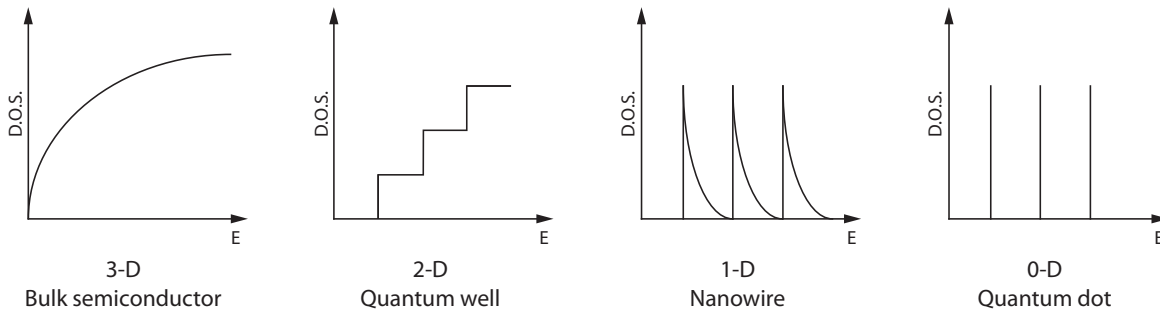


Figure 3.6 — Electronic density of states for a) 3-D crystalline semiconductor, b) 2-D quantum well, c) 1-D nanowire or nanorod, c) 0-D quantum dot. Adapted from [8].

from their bulk counterparts. For this reason, electron transport properties become an interesting area of study as a material is reduced from three-dimensional or two-dimensional to one-dimensional or even zero-dimensional. When a nanowire or nanotube diameter becomes small, singularities in the electronic density of states develop at special energies, called van Hove singularities, where the electronic density of states becomes very large resembling more closely the case of molecules and atoms but appearing to be very different from the case of crystalline solids or even two-dimensional systems (Figure 3.6). Therefore, much effort has been dedicated to the study of how the nanowire diameter controls the electronic transport properties. The electronic transport properties of metallic or semiconductor nanowires have been studied by measuring the current/voltage characteristics at different temperatures and show that some metal nanowires can become semiconducting as their diameters are reduced to below certain values. For semiconductor nanowires such as GaN it has been shown that they still could function properly as a semiconductor as their dimensions are decreased to several nanometers.^[177]

Characterization of Nanomaterials

Contents

4.1	Introduction	90
4.2	X-Ray diffraction (XRD)	90
4.2.1	Small angle X-ray scattering	91
4.2.2	Wide angle XRD	95
4.3	Electron microscopy	96
4.3.1	Scanning electron microscopy	97
4.3.2	Transmission electron microscopy	98
4.3.3	Elemental analysis	101
4.4	Sorption measurements	102
4.5	Other characterization techniques	107
4.5.1	Infrared and Raman Spectroscopy	107
4.5.2	Thermogravimetric analysis	107
4.5.3	Nuclear magnetic resonance	108

4.1 Introduction

Over the last decades, numerous methods for the characterization of nanostructured materials have been developed. Usually, a material has to be characterized by a combination of these methods, as no single technique is capable of providing complete characterization of a specific material. The main characterization tools can be grouped into three main categories; these are diffraction, microscopic, and spectroscopic techniques. In addition to that, other techniques such as sorption of gases, or thermal analysis, may give valuable information.

The purpose of this chapter is to summarize different characterization techniques that have been used in this study with emphasis on the characterization methods used for thin membranes and nanostructured materials. It is assumed that the fundamental knowledge behind all the methods is well known.

4.2 X-Ray diffraction (XRD)

While microscopes usually cover only a small part of the sample, scattering techniques provide structural information over larger areas, so statistically relevant data can be obtained.

X-rays are part of the electromagnetic spectrum and have a wavelength λ of less than one nanometer. Electromagnetic waves propagate because an electric field (\vec{E}) causes a magnetic field (\vec{H}) and so on. Electromagnetic waves can interact with the

electrons in matter, which can be described by the model of the harmonic oscillator. The electric component $\vec{E}_0(t)$ of the incident wave can “deform” the electron shell of an atom that now relaxes by emitting radiation of the same wavelength. These waves are called scattered waves $\vec{E}_s(t)$, that can be measured by a detector system.

In a crystal, the atoms (or structural elements) are organized in lattice planes. The distance between these lattice planes is of the same order of magnitude as the wavelength of X-rays and therefore constructive or destructive interference will occur. This interference can be recorded as a function of the incident angle. The relationship between the incident angle (θ), the lattice plane spacing (d), and the X-ray wavelength can be described by the Bragg equation (eq. 4.1).

$$2d \cdot \sin \theta = n \cdot \lambda \quad (4.1)$$

4.2.1 Small angle X-ray scattering

Small angle X-ray scattering allows the study of structures in the range from approximately 1 nm to 50 nm. Depending on the setup it is also possible to obtain a two-dimensional scattering pattern. This makes it an ideal tool for the analysis of anisotropic and ordered systems such as aligned mesopores.^[178–181] Other typical applications include microemulsions,^[182,183] lipid membranes,^[184] polymer systems and the determination of the particle sizes of nano powders (in suspension).

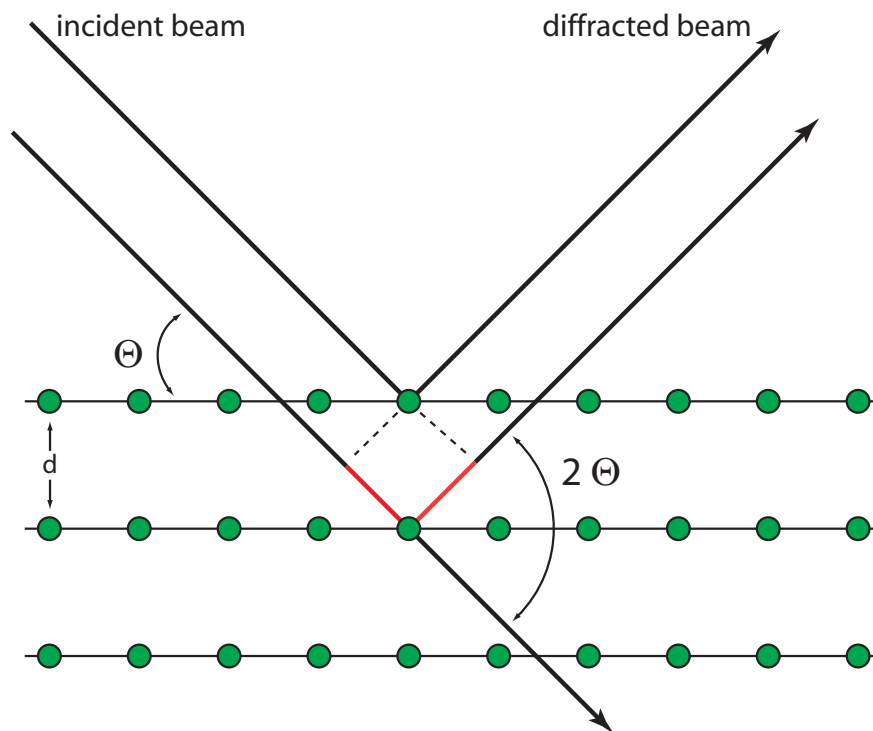


Figure 4.1 — Scheme of the diffraction of x-rays on the lattice planes of a crystal to illustrate the Bragg equation. θ denotes the angle of incidence.

Theoretical background of SAXS. As the scattering step is an intermediate step in all microscopic techniques similar relations can be applied for scattering experiments like SAXS. As the name implies, the scattered X-rays are detected at low angles (typically about $0.07^\circ < \Theta < 7^\circ$). The basic concept is the same as for all X-ray scattering methods.^[185]

As already mentioned above, a scattering experiment and a microscope have many things in common, so similar relations are valid for both experiments. Objects can only be resolved, when their size r is between a smallest and a biggest possible value ($\Delta r \leq r \leq D_{max}$).^[185] The values Δr and D_{max} define the lower and the upper resolution limit and depend on the wavelength of the incident beam and the range of angles the instrument can detect. The lower resolution Δr can be calculated via

$$\Delta r \geq \frac{\pi}{q_{max}} \quad (4.2)$$

with

$$q_{max} = \frac{4\pi}{\lambda} \sin(\Theta_{max}/2) \quad (4.3)$$

The largest objects D_{max} , that can be resolved in a SAXS experiment can be calculated in a similar way via

$$D_{max} \geq \frac{\pi}{q_{min}} \quad (4.4)$$

with

$$q_{min} = \frac{4\pi}{\lambda} \sin(\Theta_{min}/2) \quad (4.5)$$

In SAXS experiments the position of a reflex is called q-value. This value corresponds to the so called Bragg-spacing d (as commonly used in wide-angle XRD)

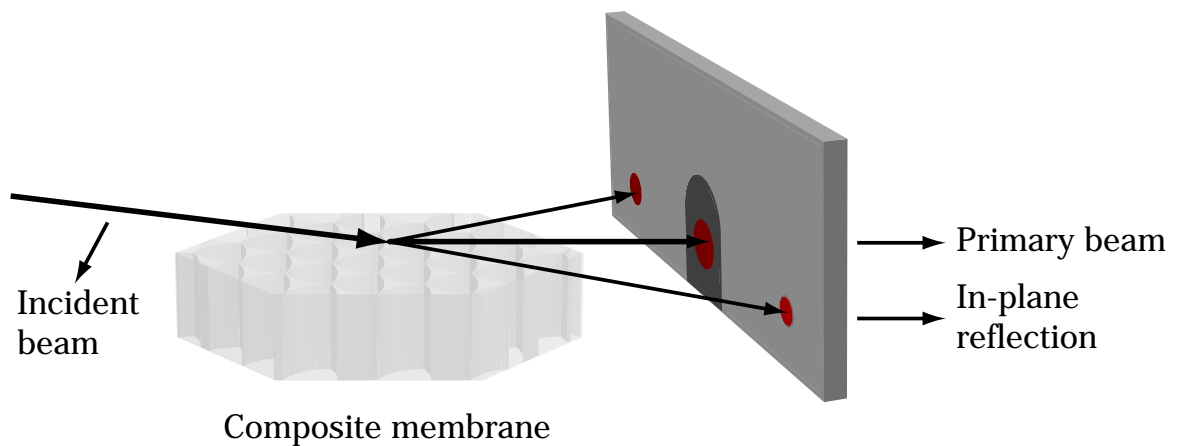


Figure 4.2 — Experimental setup for a SAXS experiment on a porous membrane. The incident collimated X-Ray beam is slightly tilted towards the membrane. While most of the x-rays pass the specimen without interaction and are absorbed by the beam stop, some are diffracted to produce a characteristic pattern.

via

$$d = \frac{2\pi}{q_{peak}} \quad (4.6)$$

where the value d is the distance between the lattice planes of the crystal.

Experimental Setup The sample is brought into a monochromatic, collimated X-ray beam. As most of the X-rays will pass the sample without being scattered (“zero-diffraction beam”), those X-rays have to be eliminated by the beam-stop. The scattered X-rays are recorded on a 2D detection system (image plate or a CCD) (fig. 4.2).

4.2.2 Wide angle XRD

Very similar considerations as already discussed above for small angles are valid for wide-angle X-ray scattering or diffraction (WAXS or just XRD) experiments. As in a WAXS experiment higher angles than in SAXS are detected, materials can be probed regarding their crystallinity; thus, information on crystal structure and sometimes even the composition of the material becomes available.

In a common powder set up with a diffractometer in $\Theta - \Theta$ geometry, the source of monochromatic X-rays (usually an X-ray tube) and the detector (scintillator or semiconductor detector) will scan along Θ (giving a plot of intensities against 2Θ) to record the so-called XRD pattern. Because a powder is usually randomly oriented and the various lattice planes are also presented in every possible orientation, cones of diffraction are created rather than “spots”. Nevertheless, because of the one-dimensional detection, well-resolved lines (Bragg peaks, reflections) are only recorded when the Bragg condition (eq. 4.1) is fulfilled.

4.3 Electron microscopy

Due to the comparably large wavelength of visible light (400 to 800 nm), normal light microscopes are limited to a magnification factor of 1000 and a resolution in the range of 0.2 micrometers. By reducing the wavelength used for imaging, much higher resolutions and magnifications can be achieved. In electron microscopy, highly accelerated electrons are used for this purpose. The wavelength of these electrons is related to the accelerating voltage U by equation 4.7:

$$\lambda = \frac{hc}{[2m_0eU(1 + eU/2m_0c^2)]^{1/2}} \quad (4.7)$$

where m_0 is the mass and e is the elementary charge of an electron, h is the Planck constant and c the speed of light. In transmission electron microscopy (TEM) an accelerating potential of 200 kV is a widely used. This results in an electron wavelength of only 2.51 pm, making an atomic resolution possible. In order to be able to focus the electron beam, electromagnetic lenses are used. For example, the condenser lens in the TEM is used to control the size and the angular spread of the electron beam that is incident on the sample.

The first electron microscope was developed by Max Knoll and Ernst Ruska in 1931. They built a transmission electron microscope analogous to an optical microscope with the only difference of using a focused electron beam instead of visible light. Scanning electron microscopes (SEM) were developed in the early 1950's and commercially available around 1965.

4.3.1 Scanning electron microscopy

Scanning electron microscopes (SEM) permit the visualization and characterization of materials down to the nanometer range. The popularity of SEM is based on its capability of obtaining topographic images of surfaces over a very wide range of materials.^[186] Nevertheless, the versatility of scanning electron microscopes is not limited to topography.

In a SEM, an electron beam is generated by an electron gun (usually a tungsten filament or a field emission gun) producing a beam of electrons. A set of condenser lenses demagnifies the beam until it has a diameter of only 2-10 nm as it hits the specimen.^[187] A set of coils sweeps the beam in a grid fashion (like a television), dwelling on points for a period of time determined by the scan speed. In more modern instruments the same effect can be achieved by a digital control of the beam position on the sample. Finally the third objective lens focuses the beam on the specimen. For each spot of the scan, the signal resulting from the interaction of the electrons with the sample is detected and can be used for contrast generation with a CRT or a computer screen. A general setup is shown in Fig. 4.3.

The mechanism for magnification is very simple. The raster scanned by the electron beam is made smaller than the raster displayed on the screen. If, for example, the scanned specimen area is $10\ \mu\text{m} \times 10\ \mu\text{m}$ and the image displayed is in the size of $100\ \text{mm} \times 100\ \text{mm}$, the magnification factor is 10000.

Secondary electrons are by far the most often used signal in scanning electron microscopy.^[187] These electrons stem from the sample region close to the surface and have an energy below 50 eV. They have a sharp emission maximum at the area close to the incoming beam enabling high resolution. They can be detected with the

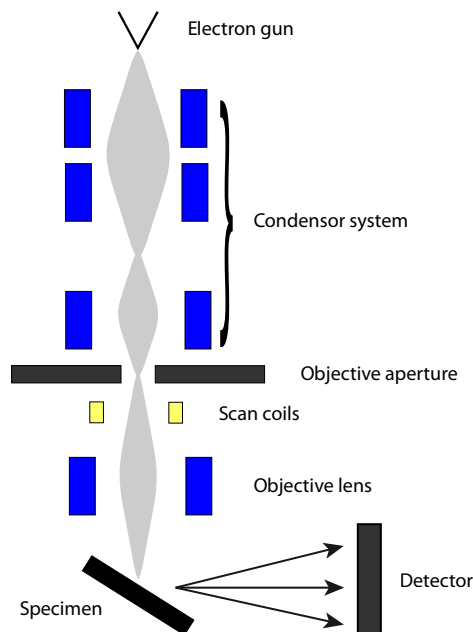


Figure 4.3 — Schematic of the operational principle of a scanning electron microscope (SEM).

use of a scintillator emitting photons which can be collected and amplified with a photomultiplier.

4.3.2 Transmission electron microscopy

Similar to a SEM a beam of highly accelerated electrons is directed at the specimen in transmission electron microscopy (TEM). But while the SEM provides mostly information of the specimen surface, a TEM can provide information about the internal structure. As shown in Fig. 4.4, the illumination system of a TEM (like electron gun and condenser system) is similar to that of an SEM, while the process of imaging is totally different.

The electron gun mounted on top of the instrument, is commonly a thermoionic gun (containing LaB_6 - or W) or for better resolution a field emission gun (FEG).

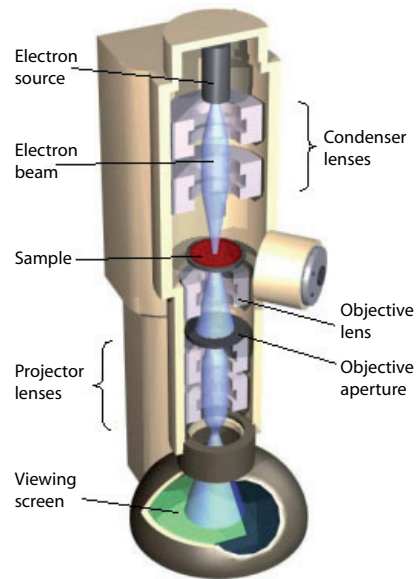


Figure 4.4 — Schematic image of a transmission electron microscope. Image taken from [188].

Using a FEG, the coherence and the brightness of the beam can be improved. The electrons are then accelerated by a high potential difference in the range of 40 to 3000 kV. The acceleration voltage depends on the type of the specimen and the required information. Microscopes using very high voltages (HVEM) have some advantages over those working in the standard range (120 to 200 kV) and those working at a medium voltage (300 to 400 kV), such as potential higher resolution and a better transillumination of the sample. But the application range of those microscopes has narrowed with the improving possibilities of sample preparation and the emergence of the field emission guns delivering a greater spatial resolution by a better coherence of the beam.

The electrons now pass a pair of condenser lenses that align and focus the beam until it hits the specimen. In TEM, the specimen has to be very thin (some tens of

nanometers) to allow the electrons to pass the sample. Behind the specimen the objective lens forms the first enlarged image that is magnified to the final image by the projector lenses. The lens system – especially the performance of the objective lens – is the main limiting factor for the resolution of the microscope. By variation of the lens current and the aperture sizes the illuminated area, the brightness, the contrast mechanism as well as the size of the beam (“spot size”) can be tuned.

On the bottom of the column a fluorescence screen displays the final image. To record the image a CCD camera (or also a conventional film camera) is used. The number of pixels and the performance of the camera are also limiting factors for the performance of the microscope.

Besides the above mentioned ‘standard’ TEM mode, microscopes can also operate in other modes. In this thesis, Z-contrast images were obtained by using scanning transmission electron microscopy (STEM). In this mode, the electron beam is focused to form a small, convergent beam on the specimen surface. The image is then formed by raster scanning the beam on the specimen and detecting the electrons transmitted from the specimen as a function of the scattering angle (Fig. 4.5). For high angle scattered electrons, the scattering probability strongly depends on the atom number. Therefore, the use of high angle annular dark field (HAADF) detectors is most popular.

In this thesis, both a Jeol JEM 2010 microscope (operating at 200 kV) and a FEI Titan microscope (operating at 300 kV) were used. STEM HAADF images and EDX spectra obtained from TEM images were recorded on the Titan microscope.

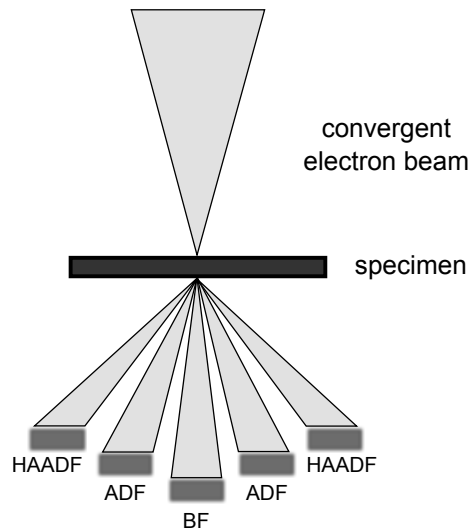


Figure 4.5 — Schematic of a scanning transmission electron microscopy (STEM) experiment and signals used for STEM imaging. BF: bright field, ADF: annular dark field, HAADF: high angle annular dark field. Adapted from Williams and Carter.^[189]

4.3.3 Elemental analysis

Modern electron microscopes can be used to obtain information about the elemental composition of a specimen using characteristic x-rays. When a sample is placed in the microscope and bombarded with high energy electrons, electronic transitions can occur that result in the generation of X-rays. These X-rays result in characteristic emission spectra of the elements present in the sample. These emission spectra can be obtained by measuring the energy dispersion of the generated x-rays (energy dispersive x-ray spectroscopy, EDX) or by sorting the x-rays according to their wavelength (wavelength dispersive spectroscopy, WDX). Using this technique, elements with atomic number as low as 4 (Beryllium) can be detected.^[190] While it is possible to obtain EDX spectra from both TEM and SEM instruments, WDX data can only be recorded in an SEM.

4.4 Sorption measurements

Nitrogen sorption is commonly used in the characterization of porous solids, giving access to the specific surface area, pore volume, and pore size distribution.^[13,191] The terms “physical sorption” or “physisorption” refer to the phenomenon of gas molecules adhering to a surface at a pressure less than the vapor pressure of the respective gas used during the experiment.^[192] With the discovery of the ordered mesoporous materials, the theoretical models for the estimation of the aforementioned parameters have been successfully proven.^[193] A result of the gas sorption measurement is a plot of the volume of gas adsorbed/desorbed vs the relative pressure p/p_0 (p is the absolute pressure, p_0 is the saturation vapor pressure) at constant temperature, called sorption isotherm. Nitrogen-sorption instruments present an important characterization tool for many laboratories dealing with nanoporous materials. The basic principle of physisorption is a weak bonding (mostly van-der-Waals bonding) of molecules on a surface. The following terms and definitions are essential for the discussion:

- **(Ad)sorptive:** the gas to be adsorbed.
- **(Ad)sorbent:** the substrate to be covered by the adsorptive.
- **(Ad)sorbate:** the adsorbed adsorptive.

Experimental gas-adsorption isotherms are categorized by IUPAC into six categories^[13] (Figure 4.6). The most important isotherms for gas adsorption on porous solids are those of a shape following type I, II, and IV. Isotherms of type I represent a sorption experiment on microporous materials, with micropore filling taking place during the steep slope at low relative pressures. Type II isotherms character-

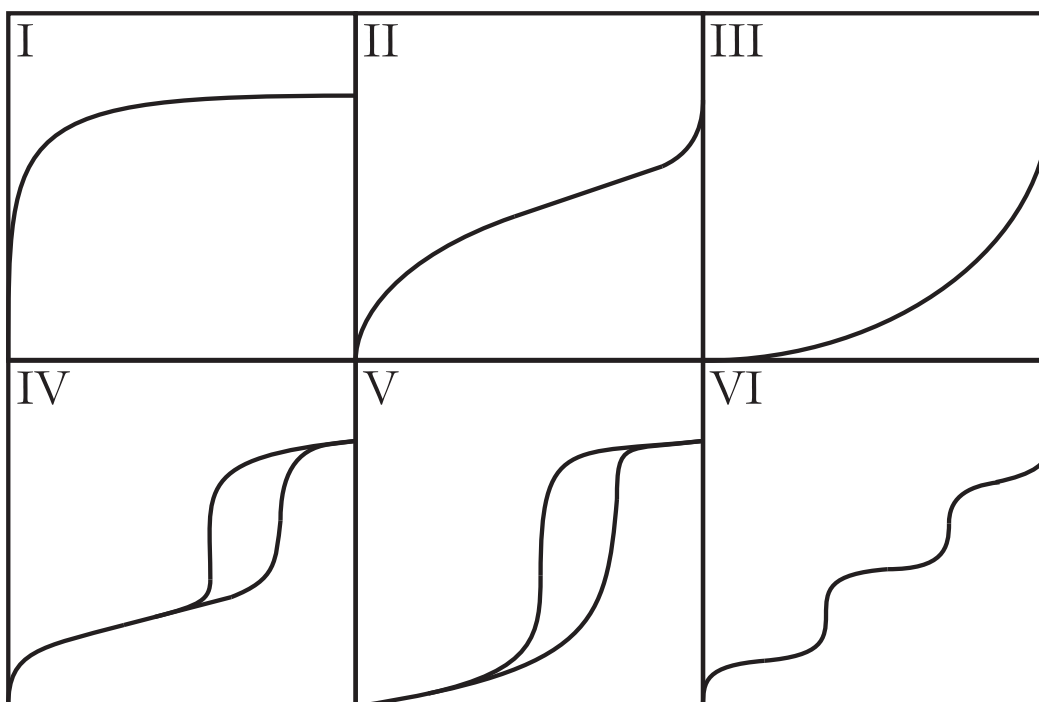


Figure 4.6 — Classification of sorption isotherms as defined by IUPAC. Isotherms of type I are characteristic for microporous materials or chemisorption. Isotherms following type II are obtained from macro- or nonporous materials with a high heat of adsorption. Nonporous materials with low adsorption enthalpies follow type III. Type IV and V isotherms with a steep second slope (capillary condensation step) are characteristic for mesoporous materials with high (IV) or low (V) adsorption enthalpies; they often show a hysteresis loop. Type VI isotherms are attributed to several possibilities, e.g., layer-by-layer adsorption.

ize sorption on macroporous/nonporous materials. In Type IV isotherms the gas absorption proceeds via multilayer adsorption followed by capillary condensation (steep steps in the isotherms).

Surface area determination. At present, there are two methods for the determination of the surface area from an isotherm: the BET method and the χ method.^[192] The BET theory,^[194] available since 1938 and named after its authors S. Brunauer,

P. Emmett, and E. Teller, is the method most widely used today. The BET equation in its standard form is displayed in equation 4.8, where n_a is the amount adsorbed at the relative pressure p/p_0 , n_m^a is the monolayer capacity and C is a constant depending on the shape of the isotherm.

$$\frac{p}{n^a(p_0 - p)} = \frac{1}{n_m^a C} + \frac{(C - 1)}{n_m^a C} \cdot \frac{p}{p_0} \quad (4.8)$$

The determination of the surface area is based on the evaluation of the monolayer capacity (the number of the adsorbed molecules in the monolayer on the surface of a material), which can be derived by plotting the BET equation in an appropriate form. The monolayer capacity is multiplied by the cross-sectional area of the adsorbed molecules in the monolayer formed on a given surface. The derivation of the BET model is based on the Langmuir equation relating the number of molecules adsorbing on the surface with the number of molecules evaporating (desorbing) from the sample, involving three main assumptions:

- There are no interactions between particles in a layer.
- The adsorption enthalpy for the agglomeration of all layers is the same, with the exception of the first layer. The adsorption enthalpy for the first layer is different as it is only based on the interactions between the adsorbent and the adsorptive.
- There is no limit in the number of layers that can be adsorbed.

In the case of adsorption on real solids, these assumptions often do not hold exactly. Therefore caution must be exercised regarding the interpretation of the specific surface area of the solids derived from the BET model. Despite the limitations, the BET

model is currently a standard method for the specific surface area evaluation, and relative comparisons provide valuable information.

Determination of the pore size. Standard methods for the determination of the pore size of mesoporous solids, such as the original BJH approach, are usually based on a modified form of the Kelvin equation. Thus, the accuracy of the calculated pore size distribution (PSD) mainly depends on the applicability and the deficiencies of the Kelvin equation.^[195] The Kelvin equation describes the change of the vapor pressure of a liquid upon the formation of a curved liquid/vapor interface. This can be assigned to the process of capillary condensation in mesopores. However, in very narrow pores, such as micropores or also small mesopores, the thermodynamic concept of a smooth liquid/vapor interface and a bulk-like pore fluid is no longer a realistic description of the system. Therefore, significant deviations from the real PSD can be expected. Several attempts have been made to establish necessary corrections to the original methods. One of them, proposed by Kruk et al.,^[196] used a corrected and calibrated form of the BJH method. A series of MCM-41 type silica samples was used for calibration; thus, this method is only applicable for these and closely related kinds of materials. In recent years, microscopic methods based on Density Functional Theory (DFT) calculations and Grand Canonical Monte Carlo (GCMC) simulations became available. These methods correctly describe the local fluid structure near curved solid walls on a microscopic level.^[195] Comparison measurements between these new methods vs. methods derived from classical thermodynamic BJH related methods showed that the DFT based models give correct results for all pore size ranges from micropores to large mesopores. Therefore, future calculations of the PSD should always be done by applying the

DFT and GCMC based models.

In this thesis, the nitrogen-sorption measurements on powdered mesoporous materials were performed with a NOVA 4000e Surface area & Pore Size Analyzer or an Autosorb-1 by Quantachrome Instruments. All samples were outgassed at 120 °C for 12 hours prior to measurement. Calculations of the pore size distribution were done by applying DFT calculations from the desorption branch (unless stated otherwise).

4.5 Other characterization techniques

4.5.1 Infrared and Raman Spectroscopy

Vibrations and rotations of molecules can be excited by absorbance of radiation in the infrared region of the electromagnetic spectra. There are two major alternatives for measuring these vibrations and rotations:^[197]

- directly as absorption in an infrared spectrum
- indirectly as scattered light in a Raman spectrum

The Raman effect is based on the inelastic scattering of light. The scattered light can show either a shift towards lower frequencies (Stokes shift), that corresponds to an energy loss, or towards higher frequencies (anti-Stokes shift), that corresponds to an energy gain from the sample. The variety of bands in a Raman spectrum can be assigned to various vibrations in the molecule and thus can help to identify the molecule can be identified. Raman experiments are often carried out via a spectrometer attached to a light microscope.^[187] A modern development is the use of Raman scattering in confocal microscopes to produce chemical maps of the specimen.

4.5.2 Thermogravimetric analysis

Thermogravimetry is a technique for measuring the change in weight of a substance as a function of temperature or time. The sample is usually heated at a constant rate and has a constant weight until it begins to decompose at a certain temperature. The differences in the weights and the slopes of the decomposition

steps are characteristic for the decomposition process and can be used for quantitative calculations of compositional changes.

4.5.3 Nuclear magnetic resonance

Nuclear magnetic resonance (NMR) experiments can give information about the local chemical environment (connectivity, coordination numbers, local symmetry) of certain magnetic isotopes in molecules.^[198] For nuclei that possess a permanent magnetic moment, the orientations of their magnetic moments are limited to discrete quantum states relative to an applied external magnetic field. Transitions between these states can be observed by irradiation of a sample with electromagnetic waves in the radio frequency region, if the respective frequency meets the resonance condition given by equation 4.9:

$$\omega = \gamma \cdot B_{loc} = \gamma(B_0 + B_{int}) \quad (4.9)$$

with

- ω : frequency of the electromagnetic field at resonance condition
- γ : gyromagnetic ratio
- B_{loc} : strength of the magnetic field at the nucleus
- B_0 : external magnetic field
- B_{int} : internal field

The measured difference between the local magnetic field strength and the applied external field gives insights into the electronic and chemical environment of the nuclei. In the case of solids, dipole-dipole interactions between the magnetic moments

4.5. OTHER CHARACTERIZATION TECHNIQUES

of nearby nuclei lead to a line-broadening in the spectra, making the interpretation of the spectra difficult or impossible. This anisotropic effect can be eliminated by rotating the sample at an angle of 54.7° (so-called magic angle) with respect to the applied field; hence this technique is named magic-angle spinning nuclear magnetic field resonance (MAS-NMR). In liquids this line-broadening effect is eliminated, as the mobility of the nuclei in a liquid is averaging these dipole-dipole interactions out.

Multiple Nanowire Species Synthesized on a Single Chip by Selectively Addressable Horizontal Nanochannels

Contents

5.1 Introduction	111
5.2 Experimental	114
5.3 Results and discussion	117
5.4 Conclusion	125

This chapter is based on the article “Multiple Nanowire Species Synthesized on a Single Chip by Selectively Addressable Horizontal Nanochannels”, published in Nano Letters.^[163]

5.1 Introduction

One-dimensional nanostructures such as nanowires and nanorods have become a major research topic over the last years.^[199–203] To date, a variety of methods for the

synthesis of these materials has been developed, such as vapor-liquid-solid (VLS) growth,^[155,161] sol-gel techniques,^[204] and template based approaches.^[205–208] Template based methods offer access to a wide variety of nanowires with a broad diversity in composition and shape. As template material most commonly substrates such as track-etched polycarbonate membranes,^[209] mesoporous silica,^[138] and porous anodic alumina membranes^[210,211] are used. Anodic aluminum oxide (AAO or Porous anodic alumina, PAA) membranes are widely used as they give an easy access to self-organized pores with high aspect ratios and tunable pore sizes.^[108,211–214] These pores are then used as a molding system for the synthesis of the desired nanostructures. Most commonly, the alumina pores are aligned perpendicular with respect to the membrane surface, making it difficult to integrate the synthesized structures into a chip. Recently, procedures to synthesize horizontally aligned anodic alumina pores on a chip have been reported,^[215,216] enabling the fabrication of single-pore devices.^[210] These pores were then subsequently filled by electro-deposition with different materials to form nanowires. The so formed nanowires are expected to have possible applications in fields such as sensing,^[217,218] nanobiotechnology,^[202] nano-optophotonics,^[202] and in nanoelectronics.^[205]

For many of these applications it is desirable to integrate different nanostructure morphologies and species on a single chip. Recently, a process where a focused ion beam was used to selectively block and unblock pores of certain regions was reported.^[219] Thus it was possible to deposit silver and copper nanowires in different regions on the same substrate. This is a very elegant technique for vertical AAO substrates. However, it has limitations for the generation of multiple (more than two) elements on a chip and for the use in horizontal alumina pores. Furthermore, using this technique it is difficult to obtain pores of different morphologies



Figure 5.1 — Schematic of a multi-contact horizontal anodic aluminum oxide device. Due to separation of the Al contacts, anodic microscopic finger ensembles can be anodized individually, enabling the fabrication of a horizontal porous alumina structure containing different pore morphologies, i.e., different pore diameter, interpore distances, and pore length. The resulting composite can then be used for the subsequent growth of nanowire arrays. Due to the electrical insulation of the individual contacts it is possible to grow different nanowires of different compositions (as indicated by the different colors of the wires in the above scheme) on the same chip.

and lengths on the same device.

The advantage of the multi-contact design reported here (Figure 5.1) is that individual contacts with various sizes are electrically separated from each other, enabling their individual anodization. Thus, a single chip can be fabricated containing various nanopore morphologies, i.e., different pore diameters and different interpore distances. Furthermore, a variation of the anodization time for the individual contacts would result in nanopore channels exhibiting different aspect ratios. Depending on the width of the individual aluminum fingers, one can easily control the number of nanopores grown within the microscopic fingers when the same anodization conditions are applied. When anodizing different contacts equipped with equally sized fingers at different anodization conditions, one would obtain different pore densities, enabling the fabrication of multi contact densities on the same

sample.

5.2 Experimental

2 inch silicon wafers were thermally oxidized to cover the surface with a 1 μm thick silicon dioxide layer. Subsequently, a 1 μm thick aluminum thin film was thermally evaporated onto the substrate from a high purity source and annealed in 10 % hydrogen in nitrogen (forming gas) at 500 $^{\circ}\text{C}$ for 4 h. The wafers were then cut into pieces with a size of 1 cm x 1.5 cm. The multi-contact design is shown in Figure 5.1.

To fabricate samples having in-plane contacts on a single chip that are individually addressable during anodization, special optical lithography masks were designed to pattern the 1 μm thick aluminum on the sample surface. Different contact configurations were investigated, starting from a single contact, up to 2-, 3-, 4-, and 5-contact samples. Figure 5.2 summarizes multiple contact sample species investigated in this work. 2-, 3-, 4-, and 5-contact samples were fabricated where the total aluminum width was kept at 5 mm.

To ensure electrical separation between neighboring contacts, a spacer width of 25 μm between two contacts was chosen. Within a single contact, equally sized and equally spaced microscopic fingers with a finger width varying between 1 μm and 5 μm were fabricated; the distance between individual fingers was fixed at 5 μm . Apart from the number of contacts chosen, one can individually tune the width of the microscopic fingers according to the application requirements, enabling the control over the number of nanochannels and thus the amount of nanowires grown.

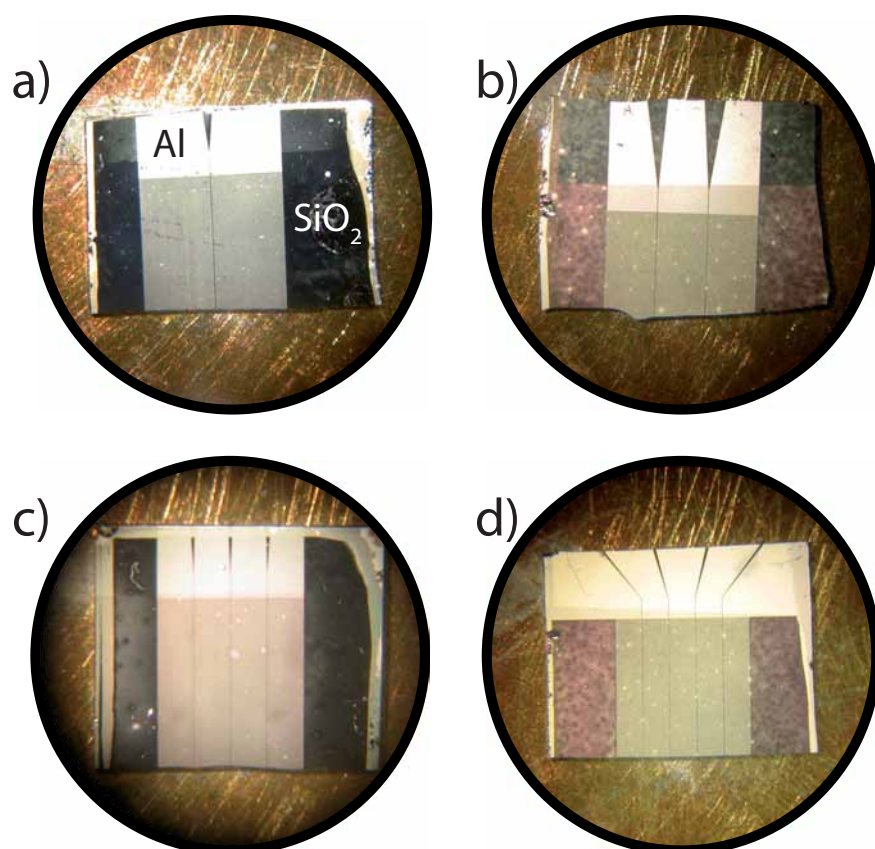


Figure 5.2 — Optical images of representative 2- to 5-contact devices, respectively. The upper bright part (denoted with Al) is serving as electrical contact area and therefore freed of silicon dioxide. The slightly darker grey part below shows the microscopic aluminum fingers insulated against the electrolyte solution by a dense silicon dioxide layer. The contacts are electrically isolated from each other, thus securing their individual anodization.

	Solution [M]	Deposition Mode	Voltage [V]
Au	0.001 M HAuCl ₄	dc	-0.5
Cu	0.64 M CuSO ₄	dc	-0.3
Co	0.4 M CoSO ₄ 0.7 M H ₃ BO ₃	dc	-1
Te	1 mM TeO ₂ 0.5 M K ₂ SO ₄	ac	8 ms@10V 992 ms@0V
Ni	1.14 M NiSO ₄ *6 H ₂ O 0.19 M NiCl 0.73 M H ₃ BO ₃ *6 H ₂ O	ac	8 ms@10V 42 ms@0V

Table 5.1 — Electro-deposition parameters used for metallic and semiconducting nanowire synthesis. All potentials are measured relative to a silver/silver chloride reference electrode.

To form pores with the desired diameters, samples were anodized in various electrolytes at 0 °C and various voltages as given in Table 5.1. Prior to the anodization process, all neighboring contact pairs were measured using a multimeter to ensure physical and electrical isolation.

In this work gold, copper, cobalt, nickel and tellurium nanowires were electro-deposited within the multi-contact samples. The respective parameters used for deposition are given in Table 5.1. Both direct current (dc) and pulsed electro-deposition was applied.

CVD growth of silicon nanowires was performed by electro-depositing a thin gold layer as catalyst. For this purpose, one tenth of the time needed to completely fill the pores as described previously was employed, corresponding to a filling of approximately 100 nm. After mounting the sample inside the CVD chamber and flushing with nitrogen gas, the growth chamber was evacuated to a pressure of 1.4 mbar at 10 sccm of hydrogen flux. The growth chamber was then heated up to

630 °C in order to anneal the gold catalyst. A period of 30 minutes annealing in hydrogen atmosphere was employed, followed by the decrease of the temperature to the growth temperature. Once the growth temperature of 570 °C for gold-catalyzed Si nanowire growth was reached, 1 sccm of silane was introduced into the chamber. After a total growth time of 3 h, the deposition was stopped, the growth chamber flushed with nitrogen, and the cooling process was started.

To investigate multi-contact samples, various combinations of anodization conditions were explored. Anodization experiments were carried out in sulfuric, oxalic, and phosphoric acid at 0 °C. The anodization voltages were chosen within a range between 20 V and 110 V, and the anodization time varied between 1 h and 16 h.

	Temperature [°C]	Voltage [V]	Concentration [M]
H ₂ SO ₄	0	20 - 30	0.3
(COOH) ₂	0	20 - 40	0.3
H ₃ PO ₄	0	50 - 110	0.4

Table 5.2 — Conditions used for the anodic oxidation of the Al thin film structures.

5.3 Results and discussion

Efforts were made to obtain single chips containing different pore sizes and pore densities, and different channel lengths.

For the anodization runs using different electrolytes and different anodization voltages on a single device, representative SEM images are illustrated in Figure 5.3. Here, a 2-contact sample was subsequently anodized in phosphoric and oxalic acid at 0 °C for 1 h. As expected, since different electrolytes and anodization voltages

were applied, two different sizes of nanopores could be observed on a single substrate. While the contact anodized in phosphoric acid results in large-pore diameters and interpore distances (pore diameter 80 nm and interpore distance 120 nm), the second contact anodized in oxalic acid shows smaller-sized nanopores (pore diameter 27 nm and interpore distance 87 nm). The pore sizes obtained on multi-contact samples are identical to those obtained in a previous publication reporting on horizontal microscopic finger structures.^[210]

The anodization of fingers having different finger widths under the same anodization conditions results only in a difference of the total number of nanopores per finger. The pore size and pore density remain constant. As shown previously,^[210] it is generally possible to decrease the finger size such that only one nanopore per finger is formed, enabling the fabrication of single-pore, and therefore single-wire devices.

When the same electrolyte, the same anodization voltage, but different anodization times were applied during anodization of individual contacts on a single sample, both the pore diameters and the interpore distances do not significantly differ from the results obtained within microscopic finger structures. The diameter and the interpore distance remain the same, only the length of the nanopores is changed following the growth rate of approximately 1 μm per hour. This is reasonable, since during anodization the alumina dissolution is field-assisted and only takes place at the bottom of each pore.

After performing the anodization of the first contact, SEM characterization indicated that the surface of the remaining non-anodized contacts was not significantly affected by the electrolyte bath. Thus, no pre-patterning effect of the non-anodized

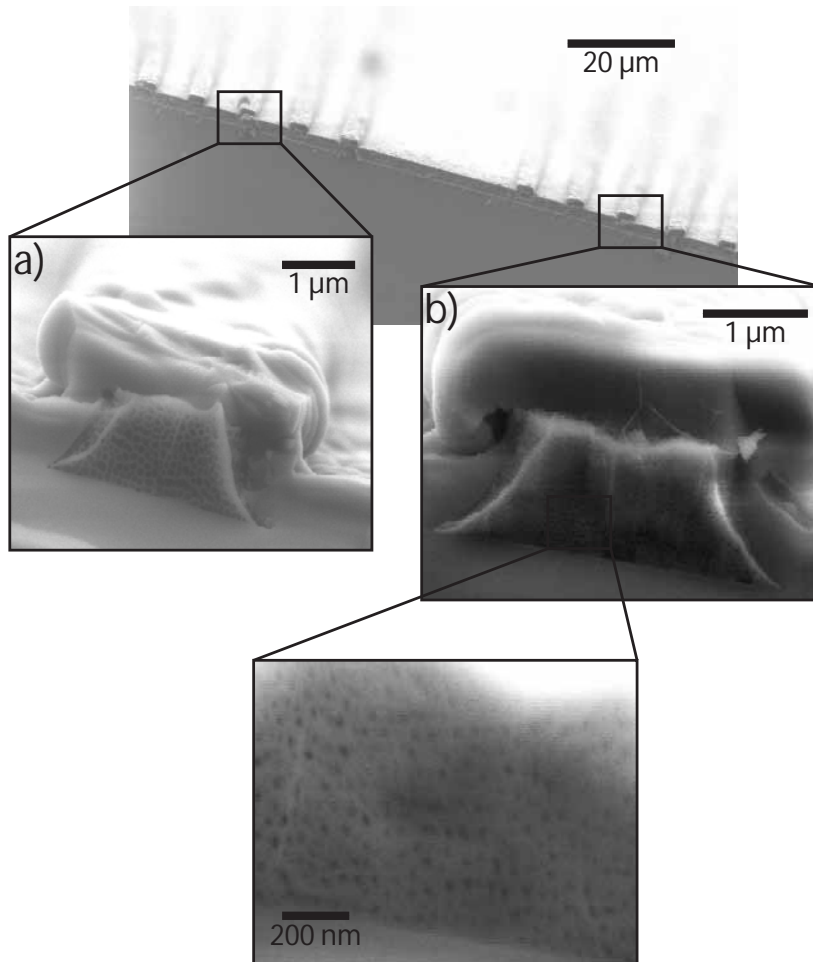


Figure 5.3 — SEM images of a representative 2-contact device. The anodization of each contact was carried out within different types of solutions and different anodization voltages. The left contact of the 2-contact sample in a) was anodized in phosphoric acid at 50 V, followed by the anodization of the right contact in oxalic acid at 40 V (depicted in b). While the microscopic fingers of the left contact reveal pore diameters and an interpore distance of 80 nm and 120 nm, respectively, the zoom-in of b) indicates a smaller pore size. The pore diameter and the interpore distance of the right contact are 27 nm and 87 nm, respectively.

fingers was observed. When the same anodization conditions were subsequently applied to all contacts, the already anodized ones necessarily were etched by the electrolyte for the time the neighboring fingers were being anodized. To quantify this undesired etching step, the etching rate of the non-connected contacts had to be studied. Therefore, individual contacts were anodized at 0 °C in oxalic acid. The anodization voltage was 40 V and the anodization time was 1 h. The difference between the 3 images in Figure 5.4 is the time period that each contact was immersed inside the electrolyte until the neighboring contacts were anodized. While image a) presents an as-anodized contact, b) and c) show contacts that were immersed inside oxalic acid baths for 1 h and 16 h, respectively. The average pore diameter histograms of the samples described above are shown in Figure 5.4a-c (bottom).

The results show that the average diameter is not significantly altered when the contacts are immersed in the electrolyte while anodizing the neighboring contacts. All samples show an average diameter of approximately 27 nm. Furthermore, with the average pore diameter being almost constant, the alumina pore wall thickness is also not significantly decreased. In principle, a slight etching of the alumina would be expected. We attribute this slow etching rate to the low working temperature. At a low anodization temperature, the chemical reaction rate is lowered compared to a higher temperature, e.g., room-temperature experiments.

The special design of the multi-contact chips allows for the synthesis of multi-sized horizontal nanostructures integrated into a single device. In bio-sensing applications it is desirable to have the possibility of detecting several different molecules, for instance enzymes or DNAs within the same solution. Additionally, horizontally aligned multi nanowire species could be integrated into existing technologies for CMOS fabrication, enabling the direct integration into electronic and electro-

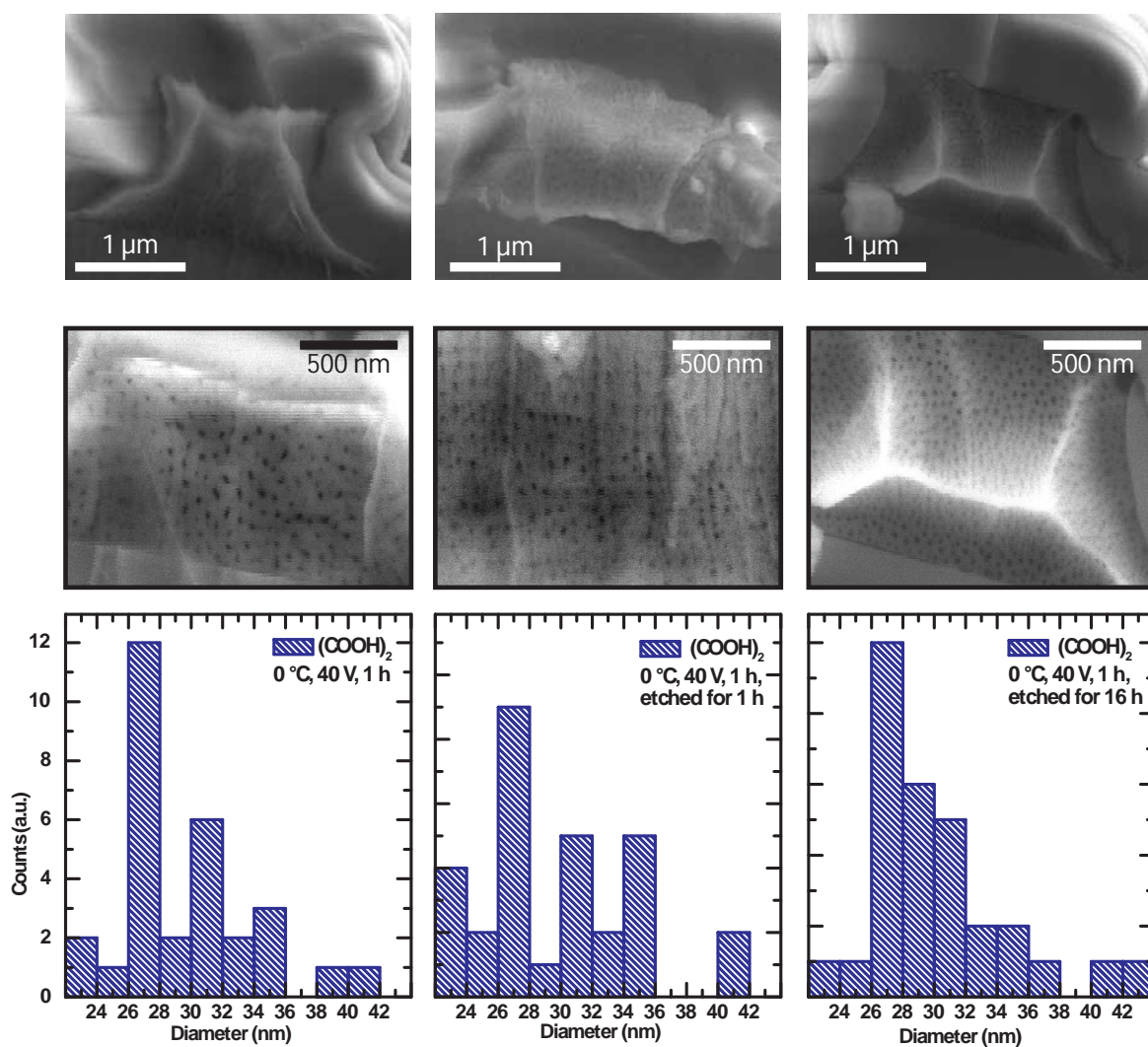


Figure 5.4 — SEM images showing the effect of pore widening during anodization of neighboring contacts. a) As-anodized sample, b) refers to an anodized sample etched for 1 h in oxalic acid, and c) shows a sample etched for 16 h in oxalic acid. All etching experiments were carried out at 0 °C.

optical devices.

An essential prerequisite for the successful electro-deposition of nanowires into the pores is a thorough barrier-layer thinning prior to wire growth. For this purpose, an adapted stepwise voltage reduction method as described by Furneaux et al.^[220] was used. When a constant voltage is applied during anodization, the barrier layer thickness remains constant due to the constant electric field oxidizing Al at the metal-oxide interface and constant oxide etching at the tip of the pores. Thus it is possible to reduce the barrier layer thickness by lowering the anodization voltage. Eventually, a total elimination of the barrier layer can be achieved by lowering the anodization voltage to a sufficiently low value.

The parameters and conditions used for pore filling are summarized in Table 5.1. Characteristic SEM images for metallic Au and Cu as well as semiconducting Te nanowires are depicted in Figure 5.5. Corresponding data for Co and Ni and EDX data obtained from those electro-deposited nanowires are presented in the supporting information. The data clearly demonstrate the successful deposition of the respective materials within the anodic alumina pores of an individual contact on a multi-contact device.

For DC electro-deposition, a low filling rate was obtained, as shown by Au and Cu in Figure 5.5. The reason for the absence of nanowires in several pore openings could be a result of a partially incomplete barrier layer thinning. A thin insulating alumina layer would shield the electric field applied, thus leading to a slower rate of reduction or preventing any reduction at all. Additionally, due to an inhomogeneous barrier layer thinning, pores equipped with a barrier layer possessing the optimum field strength are more favored as nucleation centers. Thus the filling rate

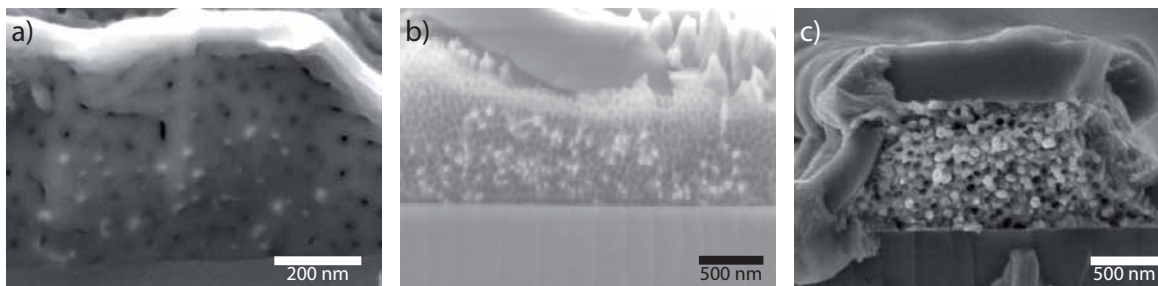


Figure 5.5 — SEM micrographs of electrodeposited nanowires within the anodic alumina pore system: (a) gold nanowires, (b) copper nanowires, (c) Te nanowires.

differs slightly, causing a variation in the length of the nanowires grown. Please note that here we only consider nanowires for the filling rate that have reached the pore opening.

A remarkable increase of the filling rate was obtained by AC electro-deposition of tellurium nanowires, as illustrated in Figure 5.5 with filling rates reaching approximately 90 %. As reported in the literature,^[214] AC deposition can result in a higher filling rate even with inhomogeneous barrier-layer thinning. This is generally explained by the rectifying effect of aluminum oxide. Aluminum oxide is a so-called 'valve metal oxide',^[221] that is, it preferentially conducts an electronic current in one direction (cathodic).^[222] This allows reduction of the metal cations only during the cathodic half-cycle, while no oxidation reaction can occur during the following anodic half-cycle.

To demonstrate the feasibility of chemical vapor deposition of semiconductor nanowires into the porous system, in a first step a small amount of gold as catalyst was electro-deposited at the pore bottom. As shown previously, the pores of anodic alumina can be filled with silicon nanowires by chemical vapor deposition.^[20,162]

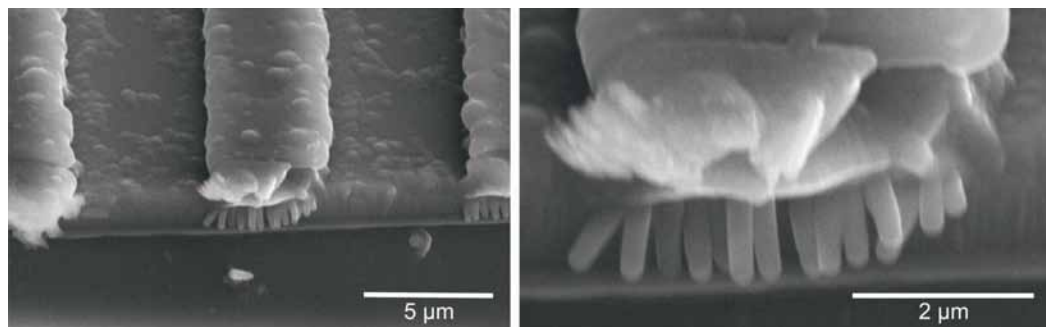


Figure 5.6 — SEM images of as-grown silicon nanowires synthesized by thermal CVD inside horizontal microscopic alumina fingers. Once the wires reach the outside of the porous system, the wire diameter is enlarged.

In order to only fill the pore bottom, the time for electro-deposition was limited to about 4 seconds, corresponding to a filling of approximately 100 nm. After annealing and the subsequent CVD growth, silicon nanowires were obtained. Representative SEM images showing an as-grown sample are presented in Figure 5.6. Horizontally aligned, equally sized nanowires are growing out of the pore opening. The diameter of the nanowires is about 100 nm, even though the initial pore diameter of the alumina pores is smaller. This could be explained by the following growth mechanism. First, during the growth within the porous alumina system, the wire diameter is defined by the spatial confinement given by the diameter of the anodic pore system. Once the catalyst reaches the pore opening, the catalyst droplet is now able to spread out to its thermodynamic equilibrium size, leading to a larger diameter of the nanowires outside the porous system. Please note that the growth direction is still conserved, even though the diameter is changed.

5.4 Conclusion

In summary, we have successfully demonstrated the concept of multi-contact anodization on a single chip with subsequent filling of the anodic pores with various metals and semiconductors. The fabrication of individually contacted and separately addressable aluminum finger structures is shown. These fingers can be individually anodized using different conditions or even using different electrolytes. Thus, different pore sizes, pore lengths, and total numbers of pores per finger are possible. The pore density is not affected by the width of the individual fingers. It was also successfully demonstrated that the already anodized structures are not significantly altered while the neighboring contacts are being anodized. The barrier layer of the anodized pores could be successfully thinned, allowing the electro-deposition of metallic (Au, Co, Ni, Cu) and semi-conducting (Te) nanowires. Furthermore, the possibility to synthesize silicon nanowires via chemical vapor deposition is demonstrated.

The multi-contact design opens up an effective and reproducible platform to synthesize multiple nanowire species, individually and independently addressable on a single chip. When using semiconductor nanowires, such as silicon or germanium, the multi-contact design offers the potential to create multiplex nanowire field-effect sensing devices. For example, by modifying individual nanowires with different surface receptors, they will enable the detection and quantification of a broad range of biological and chemical species simultaneously on a single platform. Therefore, it is anticipated that this sample design has a high potential to impact the future synthesis of complex nanostructures for sensing and nanoelectronic applications.

Synthesis of Nanowires by Electrodeposition within Columnar Silica/Alumina Composites

Contents

6.1	Introduction	128
6.2	Experimental	131
6.3	Results and discussion	133
6.3.1	Optimization of the composite membrane synthesis	133
6.3.2	Influence of the electrolyte concentration and the deposition potential	135
6.3.3	Plan view TEM micrographs	136
6.3.4	TEM of filaments	139
6.3.5	TEM of free standing wires	143
6.4	Conclusion	147
6.5	Outlook	148

This chapter is based on the article “Synthesis of Nanowires by Electrodeposition within Columnar Silica/Alumina Composites”, submitted to *Chemistry of Materials*.^[136]

6.1 Introduction

During the last decade one-dimensional nanosystems such as nanowires and nanorods have become a burgeoning field of research.^[199,223,224] Several methods have been developed for the synthesis of such structures, including vapor-liquid-solid (VLS) growth^[201,225] and template based methods.^[138,153,226] The VLS method is widely used to grow semiconductor nanowires, due to its ability to grow large numbers of highly pure and single-crystalline nanostructures. The growth process involves a liquid catalyst droplet, which adsorbs precursor molecules from the gas phase. While this approach can produce highly crystalline, high aspect ratio nanowires of numerous materials, the wires are typically not ordered and issues such as contamination from the catalyst can limit the scope of this method.^[199] In contrast, template-based synthesis offers the generation of a large variety of nanostructures, does not depend on a catalytic process, and can be used for the synthesis of vastly different materials, such as metals,^[214] metal oxides,^[227] and semiconductors.^[228] Template-based synthesis offers a variety of processing methods to incorporate the required growth species into the template host. Among the most popular methods are electrochemistry, sol-gel chemistry, and impregnation techniques.

Porous anodic aluminum oxide (AAO)^[229,230] or track-etched polycarbonate membranes^[231,232] are often used as templates, due to their commercial availability and relatively easy synthesis of different channel diameters and channel densities. These porous substrates have a channel system running perpendicular to the membrane surface, allowing the synthesis of nanowires with diameters ranging from about 10 to 400 nm. Periodic mesoporous silicates with their tunable pore sizes down

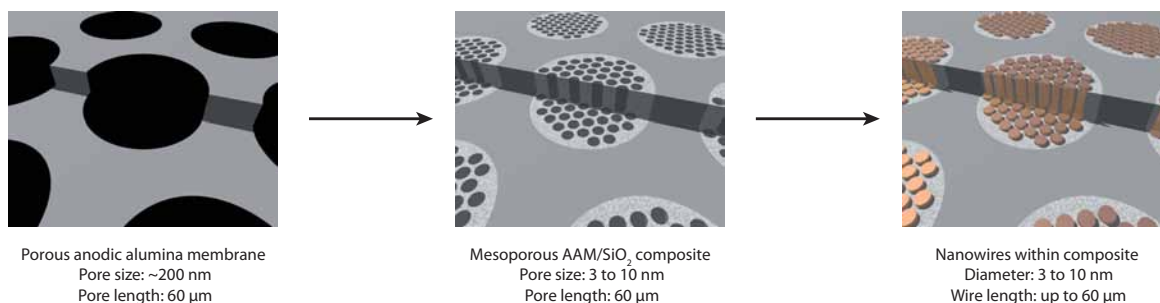


Figure 6.1 — Scheme illustrating the concept of the synthesis of nanowires within hierarchical mesoporous silica/AAO composites. The AAO pores serve as the template for the synthesis of a columnar mesoporous silica structure. This can afterwards be used as the mold for the electrodeposition of nanowires. The AAO/silica mold can be chemically dissolved; thus, free nanowires can be obtained.

to about 2 nm could extend this range to even smaller diameters, however, they are usually synthesized in the form of powders or thin films. Due to the random orientation of the channel orientation in powders, there is practically no way to contact the individual particles to an electrode; thus these systems cannot be used for electrochemical and directed growth of wires within their mesopores. Mesoporous thin films could overcome this issue, but the mesophase system usually aligns parallel to the substrate surface, thus making oriented vertical growth impossible. To overcome this challenge, several methods such as “nanometer-scale epitaxy”^[80] or mesopore alignment by electric field^[78,79] have been reported. Recently, Stucky and coworkers published the synthesis of nanowires by a hierarchical two-mold process, which involves the synthesis of a first mold of anodic aluminum oxide film that is subsequently filled by a silica mesophase.^[95] In that work, the orientation of the mesophase was tuned by changing the diameter of the alumina matrix, resulting in the formation of helical mesopores or isolated mesopore spheres. This mesophase was then used as a template for the replication of the mesopore system

by electrodeposition of silver; that way, bundles of spiral-shaped nanowires were obtained.

The orientation of the silica mesophase embedded within the alumina channels can also be controlled by choosing appropriate synthesis conditions during the self-assembly process.^[100,103] This makes it possible to extend the mesopore orientation to hexagonal circular, hexagonal columnar, and lamellar arrangements.

Here we report on the synthesis of metal (copper, silver, tellurium) nanowires within the pores of hexagonal columnar Pluronic P123 triblock copolymer templated mesopores (a scheme of the synthesis is shown in Fig. 6.2). The mesopore synthesis was carried out using commercially available anodic alumina membranes, thus giving access to high aspect ratios and allowing a reproducible synthesis. By further tuning the synthesis conditions during the evaporation-induced self-assembly process (EISA), mesoporous composites with a high fraction of the hexagonal columnar phase over the hexagonal circular phase have been prepared.^[103] Further filling of these mesopores by electrochemical deposition led to the formation of nanowires. Characterization of the wires in plan-view orientation (perpendicular view to the membrane surface) without dissolution of the surrounding AAO/silica matrix reveals high filling factors for copper and silver. The wires were further characterized by partial dissolution of the alumina matrix, thus revealing the long-range order of the mesopore channels. Finally, it was possible to obtain individual bundles of silver wires by complete dissolution of the double-mold matrix.

6.2 Experimental

Synthesis of the columnar mesophase system. Whatman Anodiscs (47 mm diameter, nominal pore diameter 0.02 μm , effective pore diameter between 150 and 250 nm) were used as anodic aluminum oxide (AAO) membranes. The columnar mesopores were synthesized similar to a previously published procedure (Fig. 6.2).^[103] Typically, a prehydrolysis solution was prepared by mixing 1.8 g (10 mmol) of water, 3.0 g (corresponding to 17 mmol of H_2O and 0.60 mmol of HCl) of hydrochloric acid (0.2 molar in water), 3.95 g (85 mmol) of Ethanol, and 2.08 g (10 mmol) Tetraethylorthosilicate (TEOS). This solution was then prehydrolyzed at 60 $^\circ\text{C}$ for one hour. To this solution, 0.75 g (0.13 mmol) of Pluronic P123 in 11.86 g (260 mmol) of Ethanol and 0.045 g (1 mmol) of Lithium chloride were added to induce the formation of the columnar phase. After thoroughly mixing the solution, 0.75 ml were cast onto an AAO membrane and dried overnight at various temperatures and humidities. The resulting composite membranes were subsequently calcined in air at 500 $^\circ\text{C}$ for 5 hours, using a heating rate of 0.5 $^\circ\text{C}$ per minute.

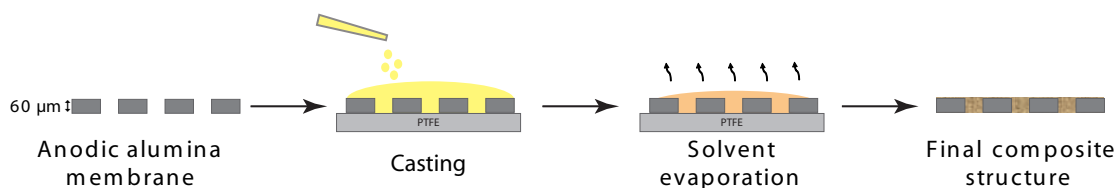


Figure 6.2 — Scheme of the mesophase synthesis within anodic alumina pores.

Electrodeposition. A 100 nm thick gold film was sputtered onto one side of the calcined membranes serving as the working electrode. A thin copper wire was attached onto the gold film using silver paste. Finally, the electrode side of the composite was carefully isolated against the electrolyte solution using nail polish.

Typically, for all the experiments a volume of 25 ml of the respective electrolyte solution was used for electroplating. The electrodeposition was performed at various potentials (-0.01 V to -1 V) using a three electrode setup and a PAR 2271 potentiostat from Princeton Applied Research. Platinum foil served as counter electrode. A constant flow of nitrogen was bubbled through the electrolyte solution to remove oxygen. The electrodeposition of silver was performed with a two electrode setup from a solution containing 0.5 mol/L AgNO₃ and 0.57 mol/L B(OH)₃. The deposition potential was set to 0.01 V using a PAR 2271 potentiostat. A constant flow of nitrogen was bubbling through the electrolyte solution to remove oxygen. Tellurium was electrodeposited from a solution containing 1 mmol of TeO₂ and 500 mmol of K₂SO₄. The pH of the electrolyte solution was adjusted to pH 2 by addition of hydrochloric acid to partially dissolve TeO₂.^[233,234] To dissolve selectively only the silica filaments, a small sample was immersed into 2.5 wt-% NaOH in a 1:1 mixture of water/ethanol. For a total dissolution of the matrix, a small piece of sample was immersed into 5 wt-% NaOH at 60 °C.

Instrumentation. Transmission electron microscopy (TEM) images were recorded using a JEOL JEM 2011 operated at 200 kV and a FEI Titan 80-300 operated at 300 kV. On the latter microscope we also performed energy-dispersive X-ray spectroscopy (EDX) and scanning transmission electron microscopy (STEM). STEM images were recorded in high angle annular dark field (HAADF) mode using a Fischione detector and a camera length of 190 mm.

6.3 Results and discussion

6.3.1 Optimization of the composite membrane synthesis

The general synthesis of mesoporous silica/AAO composites with a hexagonal columnar arrangement of pores has been published recently.^[103] As already mentioned in that previous report, the temperature plays a key role during the synthesis of these composites, as high quality hexagonal columnar mesophase systems were only found at an elevated temperature (30 °C). In this work, the synthesis was slightly altered, as the temperature and humidity were precisely controlled and kept constant during the EISA process. The resulting mesophases were evaluated by 2D SAXS (small angle X-ray scattering) measurements. In a 2D SAXS experiment, the ratio of the hexagonal columnar mesophase to the hexagonal circular mesophase can be estimated by calculating the ratio of the in-plane reflections to the out-of-plane reflections.^[103] The results of this evaluation yield a trend (Figure 6.3a), as the oop/ip ratios for 27 °C at 70 % humidity and the oop/ip ratios for 29 °C and 50 % humidity showed strong deviations and were not reproducible even on the same membrane. We attribute this behavior to the presence of a phase boundary, where already very small energetic differences have a strong influence on the phase formation. Specimens synthesized at temperatures above 29 °C and humidities above 70% did not show this variation and oop/ip ratios were reproducibly low (<0.1).

When adding this additional aging step we were able to further enhance the overall structural quality and the yield of the hexagonal columnar phase. In particular, we found by SAXS experiments that an aging temperature over 29 °C and a relative

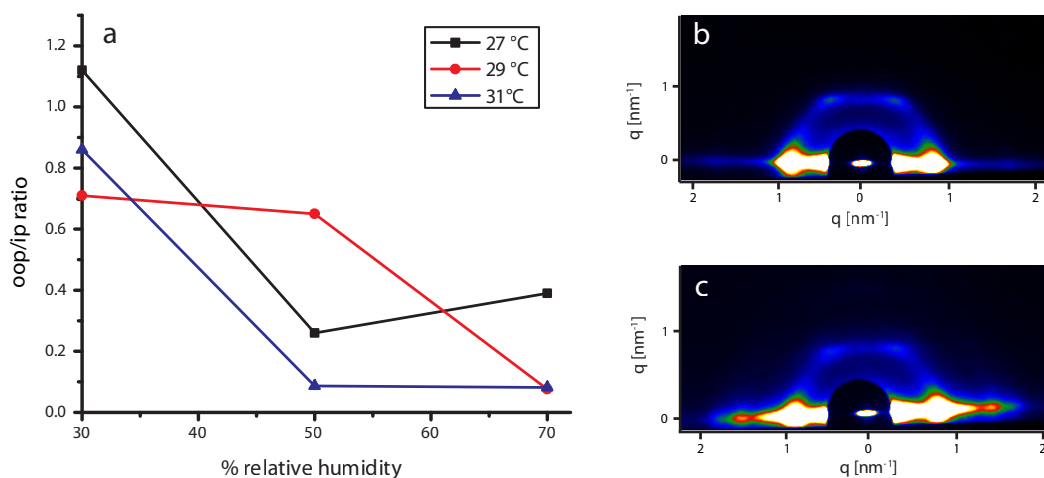


Figure 6.3 — a) Graph illustrating the trends in the formation of the circular vs. the columnar phase depending on the temperature and the relative humidity. b) and c) 2D SAXS patterns of a sample synthesized at 31 °C and 70 % r.h. before (b) and after calcination (c).

humidity of 70 % over at least 12 hours yields the highest fraction of the columnar phase. In the SAXS experiment, only very weak reflections characteristic for the hexagonal circular phase could be detected for these experimental conditions. Figures 6.3b and 6.3c show typical SAXS patterns as obtained from an as-synthesized sample (b) and a sample calcined at 400 °C (c). The calcined sample shows even stronger reflection intensities than the as-synthesized sample; this result clearly proves that the hexagonal columnar order is perfectly maintained throughout the surfactant removal process.

6.3.2 Structure of the mesoporous host and nanowire synthesis

- Influence of the electrolyte concentration and the deposition potential

TEM micrographs before electrochemical pore-filling show that not all of the pores are completely filled with the silica mesostructure prior to deposition. In particular, three main defect types have to be considered. First, a few pores of the anodic alumina membrane appear to be unfilled or only partially filled by the mesoporous silica system. Second, the existence of voids between the anodic alumina pore wall and the silica mesostructure has to be taken into account. These defects might be a result from incomplete filling by the precursor sol, or more likely, could result from pore shrinkage during calcination. Third, due to multi-point nucleation of the silica mesophase in the anopore channels one would expect mesophase domain boundaries at fairly large distances in the anopore membrane; this could cause a few discontinuities in the overall mesopore system along the 60 μm anopore channels.

For the successful electrodeposition of the wires within the mesoporous system, the concentration of the electrolyte and the deposition potential play an important role. Due to the very high aspect ratio of the pore diameter to the accessible pore length, the rate of diffusion of the ions to the electrode is an important issue. Empty AAO pores or voids in the mesopore/AAO system will show an increased diffusion rate over the small mesopores, while domain boundaries in the silica mesophase can block deposition in certain mesopores. To ensure that the depletion of the ions close to the electrode is slower than the wire growth in adventitious big voids, the concentration of the respective ions must be chosen sufficiently high.

Experiments carried out at lower concentrations (0.01 M to 0.1 M) of the respective ions showed almost no filling of the mesoporous system, while a deposition in the empty pores/voids was still observed.

When choosing the correct deposition potential, similar considerations have to be taken into account to enable the deposition in the mesopores. The rate of reduction must be kept low enough to allow simultaneous deposition in the small mesopores and possibly existing voids, cracks, or empty anodic alumina pores. For copper and silver, the same potential of -0.01 V was found to produce optimal results. When choosing higher deposition potentials, predominant deposition in big voids and/or empty anodic alumina pores was found. When choosing lower potentials, the filling rate of pores decreased and the formation of wires also decreased.

6.3.3 Plan view TEM micrographs

Plan view images give a good overview over the wire system embedded within the matrix, as both structural aspects and the degree of filling can be visualized. Figure 6.4 shows plan view TEM micrographs of copper, silver and tellurium nanowires. The micrographs of copper and silver in Fig. 6.4a-c clearly show the structure characteristic for the original hexagonal columnar order of the silica mesopore system. An estimation of the degree of filling from low magnification images is difficult and should be done with care, as damage of the specimen during sample preparation and the exact location within the membrane (height) cannot be determined. The images suggest that the filling rate varies over the sample. Furthermore, comparisons between copper-filled and silver-filled samples suggest that higher filling rates can be reached when depositing Cu.

Figure 6.4a illustrates another interesting aspect that can be derived from plan view images. The thickness of the silica wall material seems to be decreased in areas with filled mesopores, while it is retained in unfilled areas. This might be a result from wire growth, as the crystallization of the electrodeposited metal species apparently exerts enough pressure to compress the amorphous and less dense silica in the mesopore wall.

The average wire diameter is in the range of 10 nm, which is in good agreement with the pore size obtained from nitrogen sorption measurements.^[103] The micrographs show that there are some deviations in the apparent wire diameter. This might be a result of several effects. First, there might be some wires growing faster than others, expanding the pore size due to crystallization effects and compressing the available pore size in their neighboring pores. The wires growing there would then have less space available for growth, leading to smaller pore sizes. The formation of connected, small crystallites is supported by STEM images of the dissolved wires (discussed below). Second, the pore system might not be perfectly straight, resulting in a small tilt of the tubular system. As TEM images are always projections in the direction of the electron beam, this fact would result in an apparent elongation along one wire axis, also resulting in apparently larger wire diameters. Third, as already discussed above for the wall thickness, deviations in the shape of the wire might also result in the projection of a larger apparent wire diameter.

The deposition of tellurium proved to be more difficult. The solubility of tellurium oxide in water is very low (10^{-4} M at pH=2),^[233] thus the growth rate of the tellurium wires is very slow. This results in long deposition times and very poor filling rates. Furthermore, plan-view micrographs taken from the synthesized composites (Fig. 6.4d) also show a strong distortion of the silica mesophase itself, which

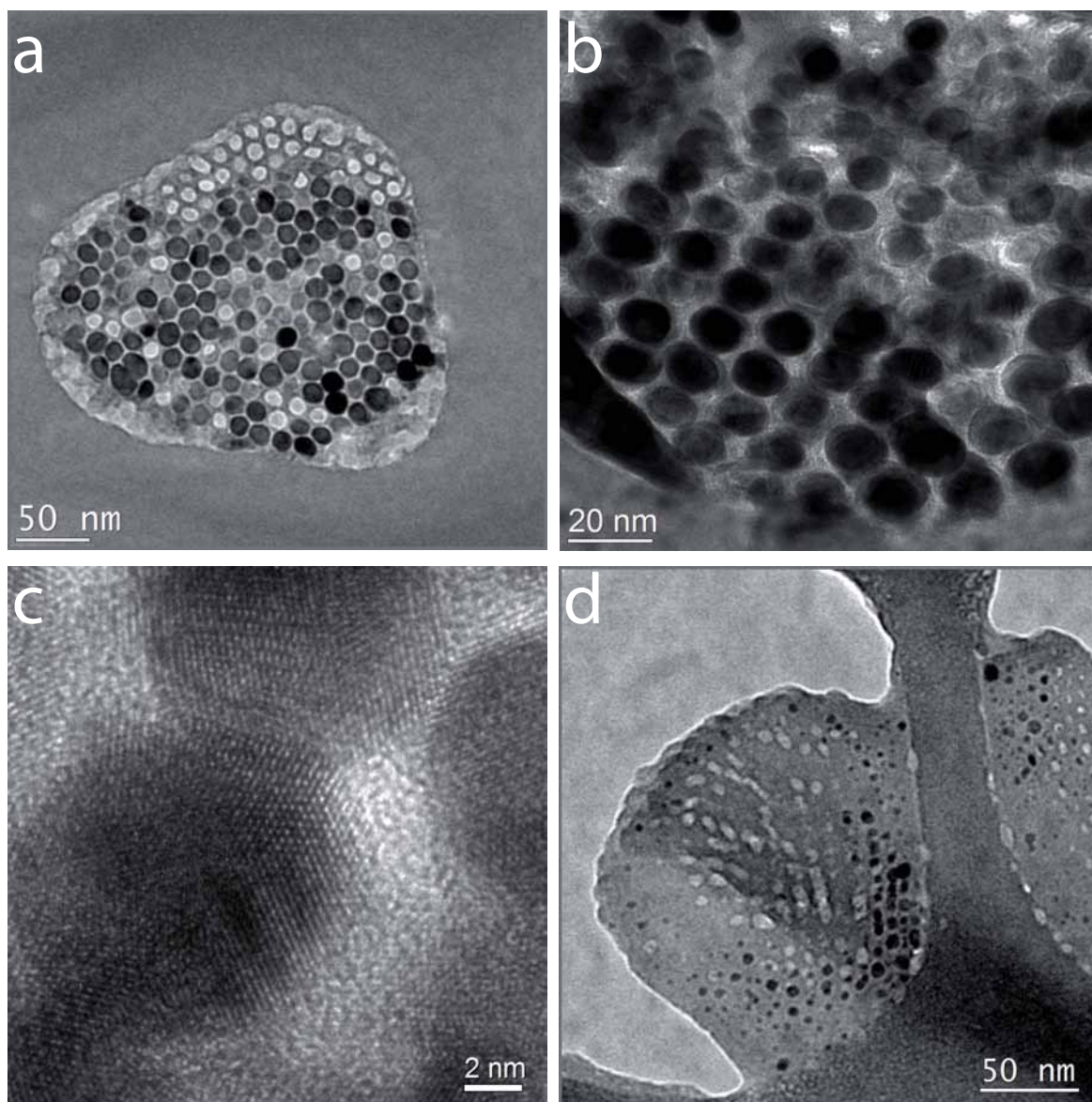


Figure 6.4 — Plan view TEM images of nanowires embedded within the AAO/silica matrix. a) TEM micrograph of copper nanowires. The wire arrangement still perfectly resembles the original hexagonal pattern of the underlying silica mesostructure. b) Close-up TEM and c) HRTEM micrographs of silver nanowires embedded within the silica mold. d) Tellurium nanowires within the silica structure. The severe distortion of the silica mesophase might result from the rigorous conditions during electrodeposition (see text).

we attribute to the long deposition times (> 12 h) in the highly acidic media.

In the case of copper and silver nanowires, further characterization by selected-area diffraction (SAED) and energy-dispersive X-ray spectroscopy (EDX) was carried out (Fig. 6.5). The SAED patterns obtained from both materials prove that the wires are crystalline. The EDX spectrum of the alumina/silica/composite materials shows – besides carbon – no elements other than those expected from the alumina/silica double mold and the wires themselves; thus, the synthesized structures are chemically clean.

6.3.4 TEM of filaments

Plan view micrographs of silica mesophases embedded in an AAO matrix only show a local cross section of the porous system. Thus, the long-range order of the porous system and of the embedded wires cannot be visualized this way. Standard TEM cross sections also suffer from such a drawback, as the electron-transparent area is rather small. Furthermore, these preparation methods involve abrasive steps during specimen preparation (grinding and ion milling). The effect of these steps on the specimen is yet unclear, but we suppose that different milling rates of the ceramic host and the metallic nanowires may lead to changes in morphology. In particular, the degree of filling of the mesopore system with nanowires might be underestimated. Thus, to reveal the long range order of the silica mesophase and the wires embedded therein, the AAO matrix was selectively dissolved by immersing the samples into a sodium hydroxide solution. This way it was possible to obtain long silica/nanowire composite filaments, whose structure can be studied by TEM.

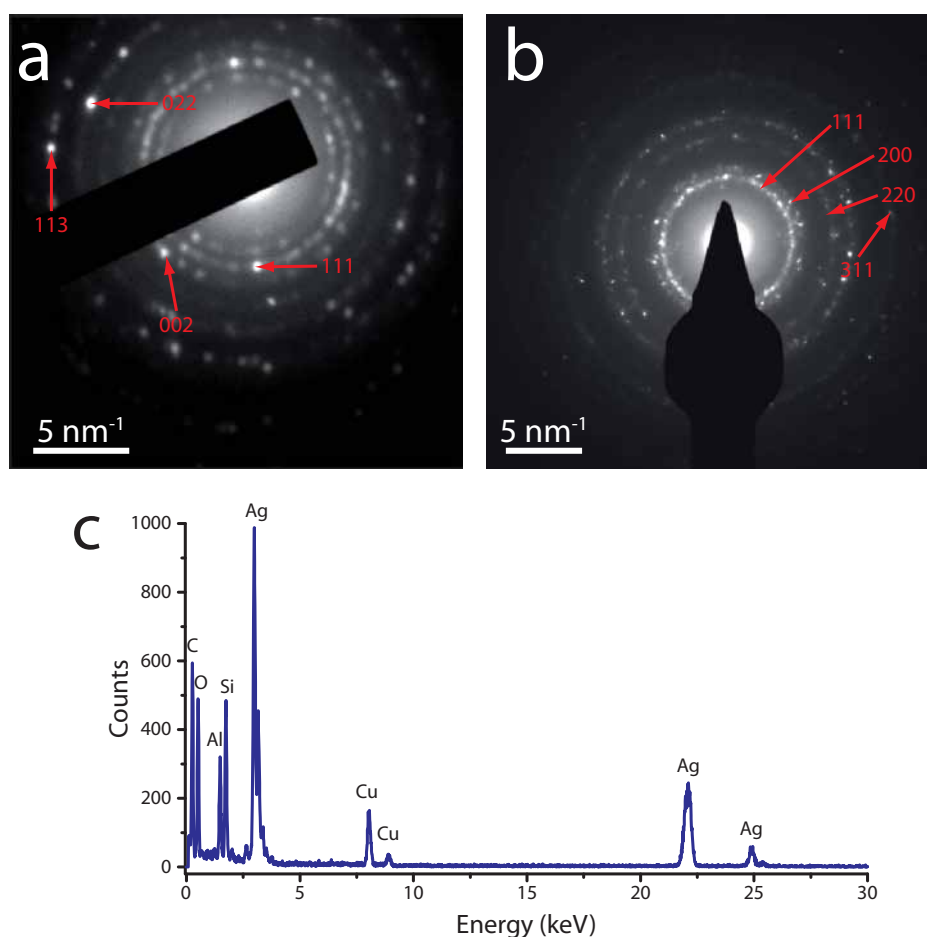


Figure 6.5 — SAED patterns of a) copper and b) silver nanowires embedded within the silica mold. The patterns can be indexed to the respective element phases (both elements crystallize in the $Fm\bar{3}m$ space group). c) shows an EDX spectrum obtained from an alumina/silica/silver composite. The copper signals are an artifact of the supporting copper grid in TEM.

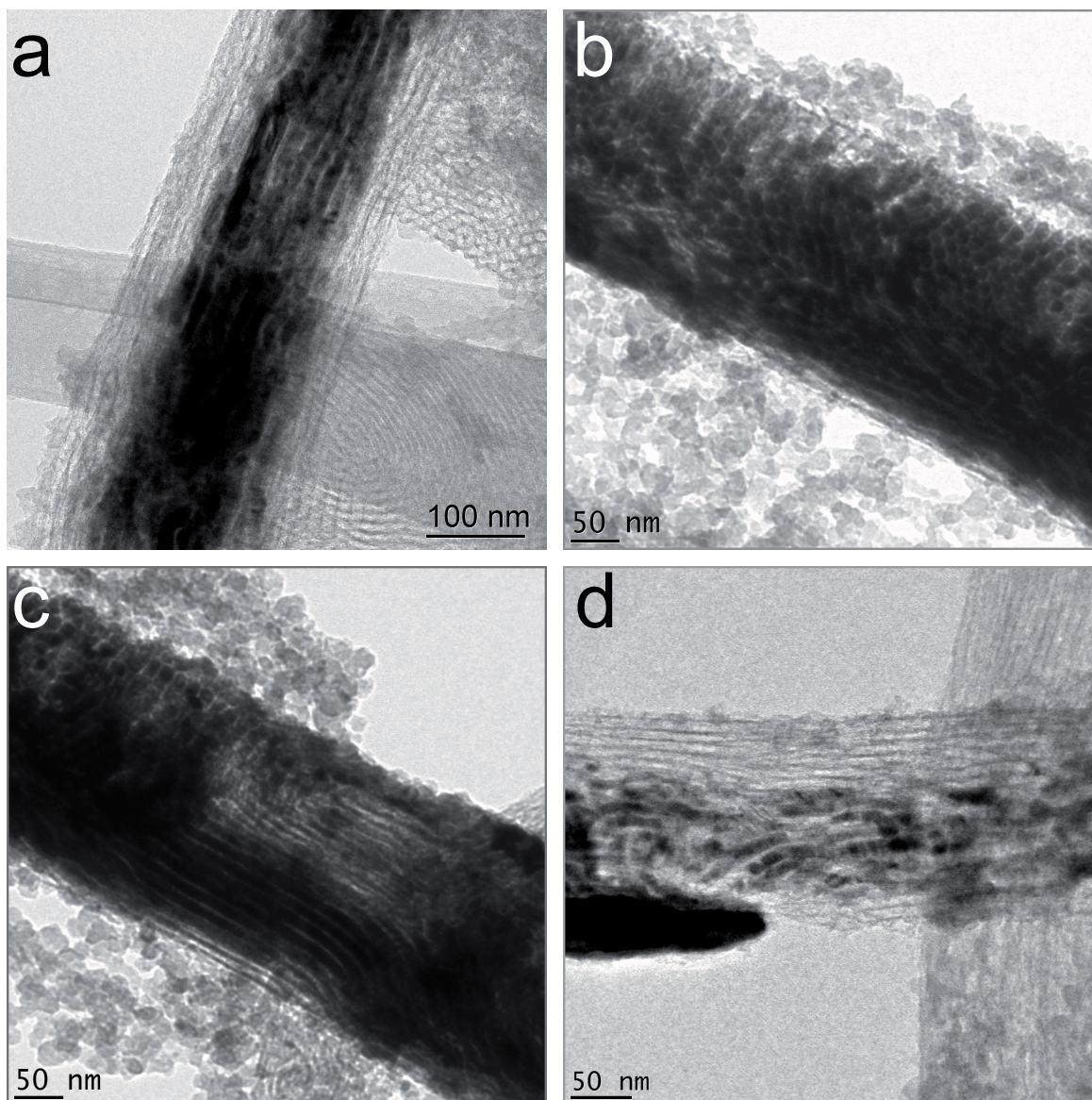


Figure 6.6 — TEM micrographs of silica filaments dissolved from the AAO mold and filled with copper nanowires. a) silica filament filled with columnar nanowires. b) Filament with the hexagonal circular mesostructure. The wires still follow the circular host structure. c) TEM micrograph of a phase-change region. The mesosystem orientation changes from a columnar to a circular domain. d) Filament with a copper chunk.

TEM micrographs of the specimens revealed a large variety of empty, partially filled, and completely filled silica filaments. Here we focus on the imaging of partially filled filaments, because completely filled filaments tend to become intransparent for electrons due to their projected thickness of up to 300 nm. Micrographs of partially filled filaments (Figure 6.6) give an overview on the structural diversity of filaments. As already discussed above for the plan view images, the hexagonal arrangement of the original mesopore system is perfectly replicated. The average wire diameter is again in the range of 10 nm. The hexagonal columnar phase is the dominant phase; however, orientational switching of the hexagonal phase between the columnar and the circular orientation of the hexagonal channel system can be observed in some regions over the whole length of the filaments. Wires grown in regions exhibiting the hexagonal columnar phase (Figure 6.6a) illustrate that the porous system can be twisted in such regions, while leaving the hexagonal short-range order intact. This cannot be readily visualized with thin sliced plan view samples. In regions exhibiting the hexagonal circular phase (Figure 6.6b) similar geometries as for plan view images can be observed as expected. Many of the silica filaments show phase boundaries from one phase orientation to another, with the wires following these structures (Figure 6.6c).

Another interesting feature is the existence of larger chunks attached to the sides of the some filaments as depicted in Figure 6.6d. These metal objects are attributed to defect sites in the anopore channels that had not been completely filled by mesoporous silica, but could still be filled with metal through diffusion from neighboring mesopores. By stitching together a series of images (“mapping”), the long-range arrangements in such filaments can be visualized over several micrometers.

6.3.5 TEM of free standing wires

Free silver nanowires could be obtained by dissolving the host matrix completely in a hot sodium hydroxide solution (TEM and STEM micrographs in Figure 6.7). Dissolution experiments carried out at room temperature resulted only in the dissolution of the alumina membrane, while the silica/metal filaments stayed intact.

The free standing wires vary in length; most of the wires appear to be broken either during preparation for TEM or directly during the dissolution process (Figure 6.7a). Due to the nature of electrochemical growth with the wire tip always acting as the active cathode for further wire growth, all broken wire fragments must have been connected during growth and as long as they were still embedded within the silica matrix. In micrographs obtained from the isolated silica filaments (Figure 6.6) no evidence for broken wires could be found. It is noteworthy to mention that no coiled wires could be found that would have resulted from the hexagonal circular mesostructure, which implies that these wires have either uncoiled or that the fraction of the circular mesophase was negligible. The average wire diameter measured from the micrographs is still within the range of 10 nm.

HRTEM micrographs as depicted in Figure 6.7b did not show any direct evidence for the presence of interwire connects resulting from deposition within the microporous pore walls of the silica phase. However, the wires were always found to be agglomerated to bundles; Ryoo et al. have attributed the existence of such bundles to the presence of micropore interconnects,^[137] gluing together individual wires even after removal of the silica mold. The indexing of the SAED patterns in the inset of Figure 6.8a reveals the formation of the standard cubic ($Fm\bar{3}m$) silver phase. This also corresponds to wide-angle X-ray diffraction data obtained from the re-

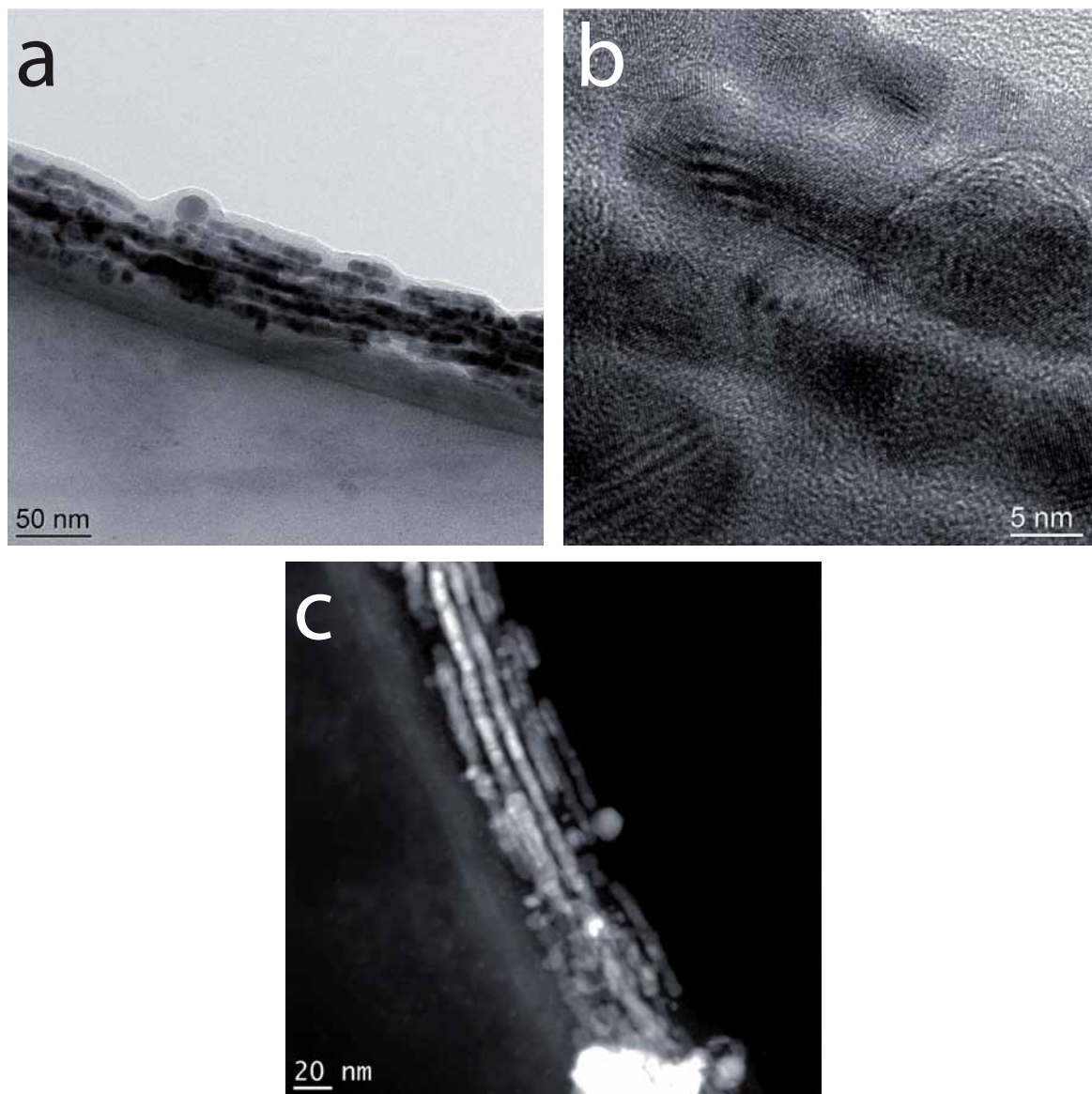


Figure 6.7 — Characterization of the dissolved silver wires. a) TEM micrograph of a bundle of Ag nanowires adhered to the carbon support of a TEM grid. b) Corresponding HRTEM micrograph of the wires, illustrating the polycrystalline nature of the wires. c) HAADF STEM image of the isolated silver wires.

spective membranes. STEM-HAADF images show that the individual wires exhibit slight variations in their contrast (Figure 6.7c), which could be due to variations in thickness.

The complete dissolution of the host matrix could be clearly proven by EDX measurements. The spectra depicted in Figure 6.8b show strong signals for silver, but no signals for the elements of the double mold matrix (aluminum and silicon). The signals for copper result from the copper grid used as a substrate for electron microscopy. The presence of only traces of oxygen indicates that the wires have not been oxidized to silver oxide, which is confirmed by SAED diffraction (inset in Figure 6.7a). In contrast to the silver nanowires, free copper nanowires could not be successfully prepared by the described approach. TEM micrographs taken from such samples only showed formation of large amounts of salts, as copper is most probably not noble enough to withstand the treatment with hot NaOH.

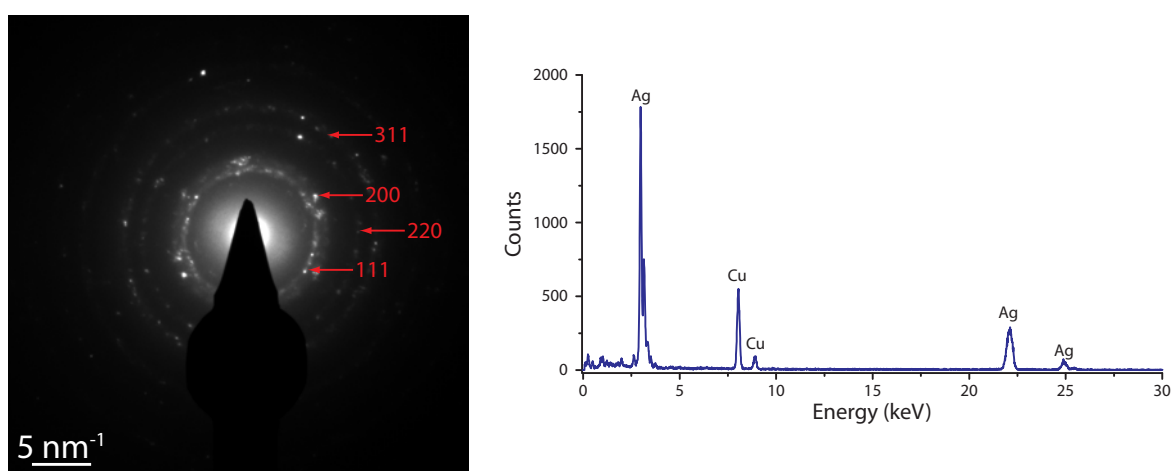


Figure 6.8 — a) SAED pattern of the free wires. The pattern can be indexed to the standard silver phase (space group $Fm\bar{3}m$). b) EDX data proving the complete absence of the composite mold material (AAO/silica matrix). The low oxygen content also indicates that the wires have not been oxidized during the mold removal process. The copper signals result from the supporting copper grid in TEM.

6.4 Conclusion

In summary, we have successfully synthesized copper and silver nanowires with diameters of approximately 10 nm by electrochemistry within hierarchical mesoporous composite structures. The existence of these wires within the matrix was demonstrated with plan-view TEM, STEM and EDX measurements. TEM micrographs of free silica filaments filled with copper show that the metal phase can replicate the mesoporous phase over a long distance ($>1 \mu\text{m}$). Individual silver nanowires could be completely dissolved from the matrix. The plan-view micrographs of both the silver and the copper nanowires embedded in the mesoporous composite matrix show an almost perfect hexagonal alignment originating from the host silica mesophase. TEM-maps generated from micrographs of isolated silica filaments filled with copper provide insights into the domain structure of the anopore-embedded mesoporous silica; an orientational switching between columnar and circular hexagonal phases can be observed. Finally, silver nanowires could be completely isolated from the host matrix as proven by TEM, STEM, and EDX measurements.

6.5 Outlook - Silica Mesopores within AAO on Conductive Substrates

The possibility to obtain high-aspect ratio metal nanowires by electrodeposition into mesoporous AAO/silica composites was successfully demonstrated above; nevertheless, there are some important challenges – such as homogeneity of the mesophase, the existence of voids, and the over-all fill rate – remaining. These challenges are addressed by creating a slightly adapted synthesis strategy as depicted in Figure 6.9. First, a 500 nm thick aluminum film is sputter-coated onto a glass substrate covered by a thin, conductive oxide film. Due to this conductive layer, the aluminum can then be anodized directly on the substrate. As the ITO itself is not etched during the electrolysis, the Al can be completely anodized; thus, no subsequent removal of the barrier oxide is necessary. By moving from the commercially available, large pore Whatman Anodisc substrates towards lab-anodized thin films much more regular pore systems with an almost circular pore cross-section can be obtained. Furthermore, the pore size of the anopores can be tailored to an optimized size. The synthesis of the silica mesophase is, similar to the experiments in the commercial membranes, carried out using an EISA process. The precise compositions are given already in section 6.2. After the removal of the structure-directing agent, the composites can be used directly for the electrodeposition of metallic nanowires. As the FTO/glass substrate itself is already conductive, no further attachment of an electrode is necessary; thus, the time-consuming and delicate steps of applying the electrical contact and sealing the electrode backside by nail polish can be avoided.

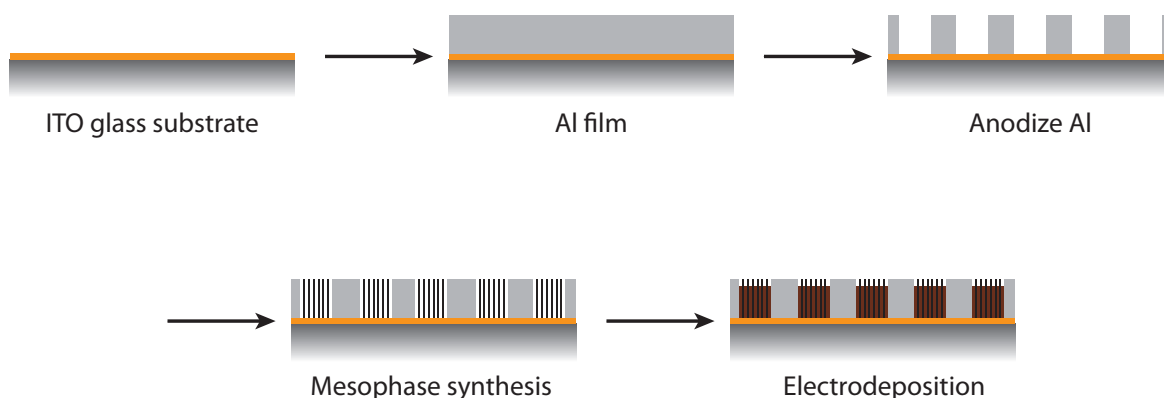


Figure 6.9 — Scheme of the improved synthesis strategy for the electrochemical deposition of nanowires within AAO/silica composites. In a first step a conductive ITO glass substrate is sputter-coated with a 500 nm thick Al film. After anodization, the anodic alumina pores are filled with a silica mesostructure. As the substrate itself is already conductive, the nanowires can be directly filled by electrodeposition.

Experimental details. The experiments are still in a very early stage and represent merely a proof of concept rather than optimized results; thus only limited experimental details are presently available. Glass slides with approx. 1 cm by 1 cm in size covered by a 100 nm thick layer of either tin-doped indium oxide (ITO) or fluorine-doped tin oxide (FTO) were used as conductive substrates. After careful cleaning using dilute HCl and ethanol, an approximately 500 nm thick film of aluminum was sputter coated onto the substrate surface. The anodization was carried out in a 0.3 molar oxalic acid electrolyte at 40 V. An electronic feedback system based on current ensured that the power was switched off at the moment the anodization process reached the conductive oxide film to prevent delamination of the AAO film. A final pore size of 60 to 80 nm was obtained after pore widening in an aqueous 5 % phosphoric acid solution for 1 hour. For the synthesis of the silica mesostructures, sol solutions with the compositions as already discussed above were used. This precursor solution was then spin-coated, cast, or dipcoated onto

the substrates to allow the mesophase formation by the EISA method. The resulting composites could be calcined successfully at 500 °C.

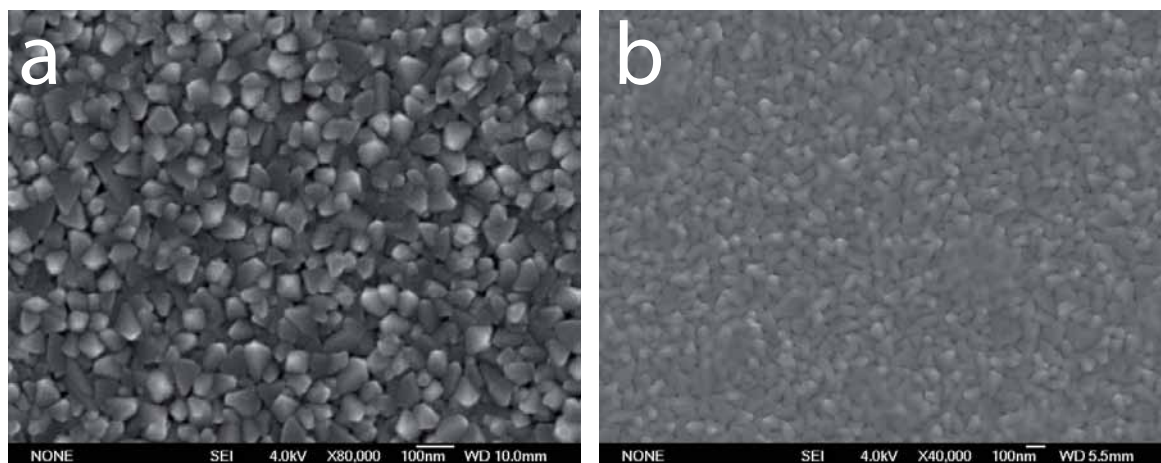


Figure 6.10 — SEM micrographs of aluminum films on FTO/glass substrates. a) depicts a film prepared by a sputter coating process; b) is prepared by a thermal evaporation process. Both films show a similar degree of fragmentation by a grainy structure.

Results and discussion. As the pore nucleation and formation process preferably starts at defect sites (see Chapter 2.2), it is desirable to have a homogeneous and flat aluminum film surface after the sputter process. Unfortunately, such films could not yet be produced. Figure 6.10a depicts an SEM image of a sputter-coated aluminum film. The film surface consists of small aluminum grains with sizes at the order of about 100 nm. SEM cross-sections prepared from such films show that this grainy structure is maintained over the whole film. At this moment, we attribute the grain formation to the sputtering process itself. Due to the high energy, aluminum clusters rather than single Al atoms may be knocked out of the aluminum target. Initial experiments showed indeed that the cluster size is increasing with increasing plasma energy used for the sputtering process. Thus, it would be de-

sirable to sputter at very low plasma energies; unfortunately, already at the lowest possible energy at which Al sputtering occurs large clusters are obtained. Al films on conductive oxide glass slides were also prepared by thermal evaporation of aluminum. For these films, a similar grainy film morphology is observed (Fig. 6.10b). As we did not have easy access to such a machine, no detailed investigations or optimizations were carried out on these films.

The effect of the grainy aluminum film morphology on the anodization process and the resulting porous aluminum films can be seen in SEM images of the as-anodized films (Fig. 6.11). The pore nucleation and growth is much more pronounced at the Al grain boundaries, leading to an increased pore size and an elongated pore shape in these regions. The pores growing in the grain centers appear to be smaller and of a more rounded shape. The initial pore size is in the range of about 20 nm, which is too small for the following mesophase synthesis. To widen up the pores, they were etched in an aqueous phosphoric acid solution at room temperature. This is a very common process to tailor the pore size of AAO films after anodization to specific requirements.^[210,235] Fortunately, it also evens out the anopore inhomogeneities to some extent, thus giving the whole film morphology look much more regular appearance. For the later synthesis of the silica mesophase, an anopore diameter of about 60 nm was targeted, as this diameter allows the synthesis of a significant number of mesopores per channel while keeping the effect of confinement low enough not to obtain isolated spherical pores as reported by the Stucky group.^[95] The pore widening effect was therefore studied and it was found that the pore diameter scales linearly with the etching time. After 60 minutes of etching in H_3PO_4 , an average pore diameter of 50 nm can be obtained. The SEM micrograph of such a film depicted in Figure 6.11b shows well-defined pores with a

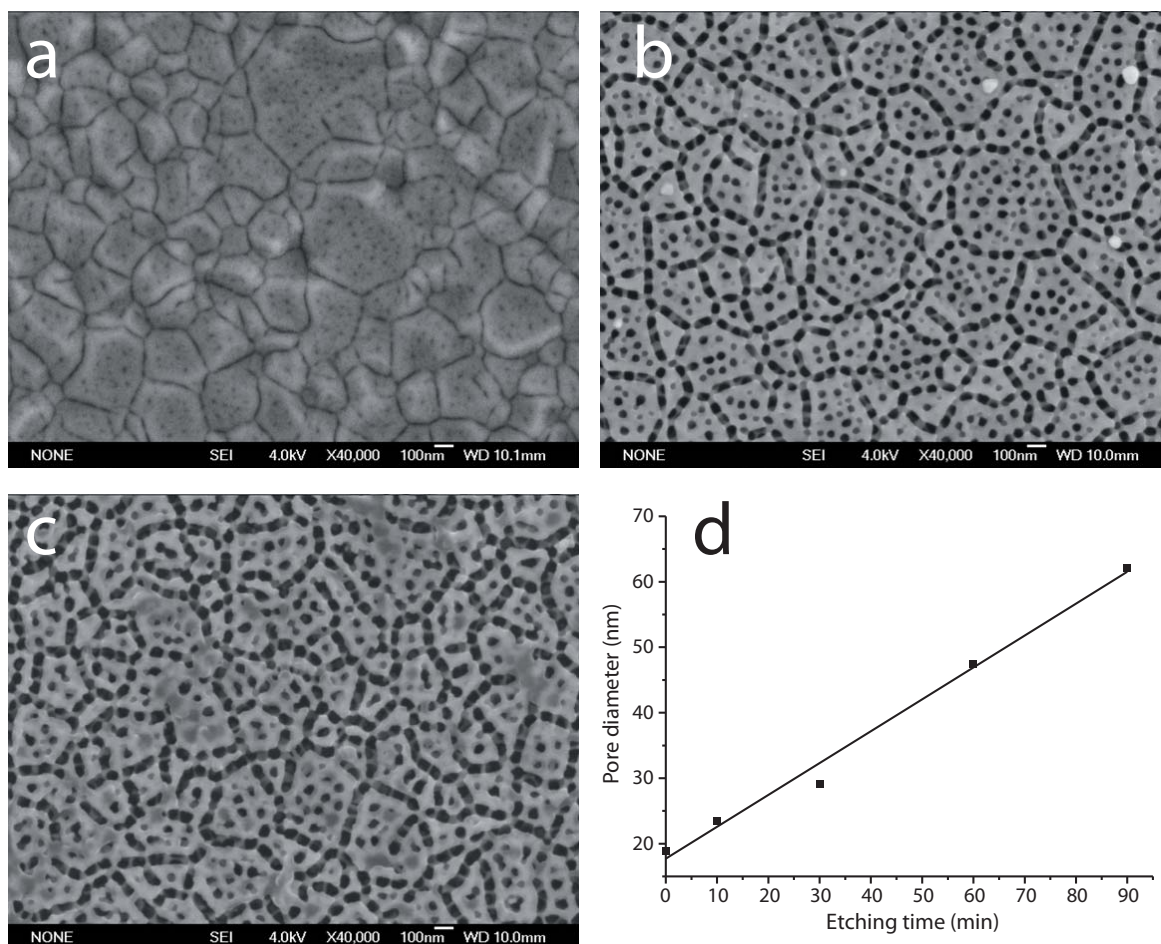


Figure 6.11 — Effect of pore widening on the porous anodic alumina film morphology. a) as-synthesized film without any further treatment after anodization, b) after 60 min. of pore widening, c) after 90 min. of pore widening. The graph in d) depicts the linear dependence of the anopore diameter from the etching time in phosphoric acid.

sufficiently narrow pore size distribution. Films with a pore size of 60 nm, as originally aimed for, can in principle also be obtained after 90 minutes of etching time (Fig. 6.11c). Unfortunately, some pores were found to already merge as the alumina pore walls were partially consumed by the phosphoric acid. As this leads to a very inhomogeneous pore-size distribution and strongly elongated anopore shapes, an etching time of 60 minutes was preferred for the following experiments with the silica mesophase.

Initial experiments on the synthesis of silica mesophases within the anopores have already been carried out and characterized. As a starting point, precursor solutions with compositions as already used for the synthesis of SiO₂ mesopores within the commercial Whatman membranes have been used. In addition to the casting method employed there, also dip-coating and spin-coating experiments have been carried out. Best results (with respect to mesopore order) were found for samples prepared by the spin-coating technique. The TEM micrographs of such composites are shown in Fig. 6.12 show the evolution of a highly ordered mesophase. The filling of the anopores with the confined mesophase was found to be complete in all electron-transparent regions. No voids caused by bubbles or incomplete penetration of the pores with the precursor sol were found. In the images, only a thin surface layer of the silica mesophase was observed, as it can be expected for a spin-coating experiment. The mesophase orientation is most likely to be circular hexagonal, although a cubic phase cannot be completely ruled out. This could best be clarified by 2D SAXS measurements; unfortunately, successful experiments were not yet possible with our laboratory equipment. Due to the fast evaporation process during spin-coating, we might expect that the phase to be formed will usually be the kinetically more accessible one. In experiments on the Whatman membranes,

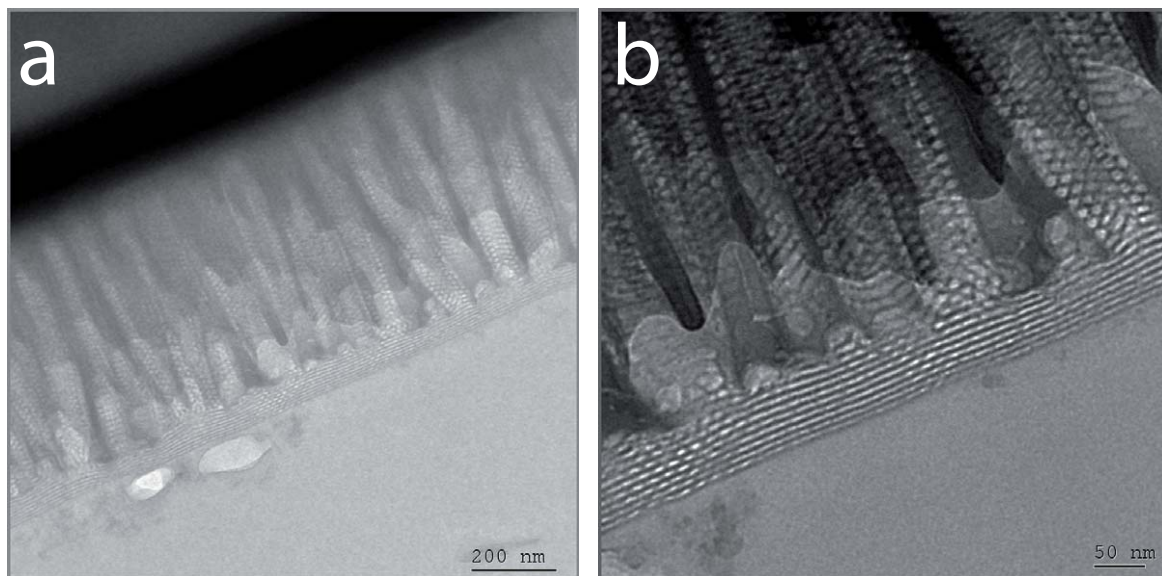


Figure 6.12 — TEM micrographs of a silica mesophase synthesized within AAO thin films prepared by spin-coating. The cross-sections show excellent degrees of filling with a high order of the mesostructure.

this was usually the circular mesophase rather than the hexagonal columnar one. Thus it is still an open question if a highly columnar mesophase can be synthesized by spin-coating.

Ordered silica mesophases could also be obtained by spin-coating and casting methods. TEM micrographs of these composites did not yet show as nicely ordered systems as those that were obtained from dip-coated samples. Nevertheless, as the speed of evaporation can be slowed down by adjusting the humidity and temperature during the EISA process, these experiments could finally lead to the formation of hexagonal columnar mesophases. First results from dip-coated samples already suggest that this might indeed be possible (Fig. 6.13), but up to now only poorly structured specimens could be prepared from such systems making further optimization necessary.

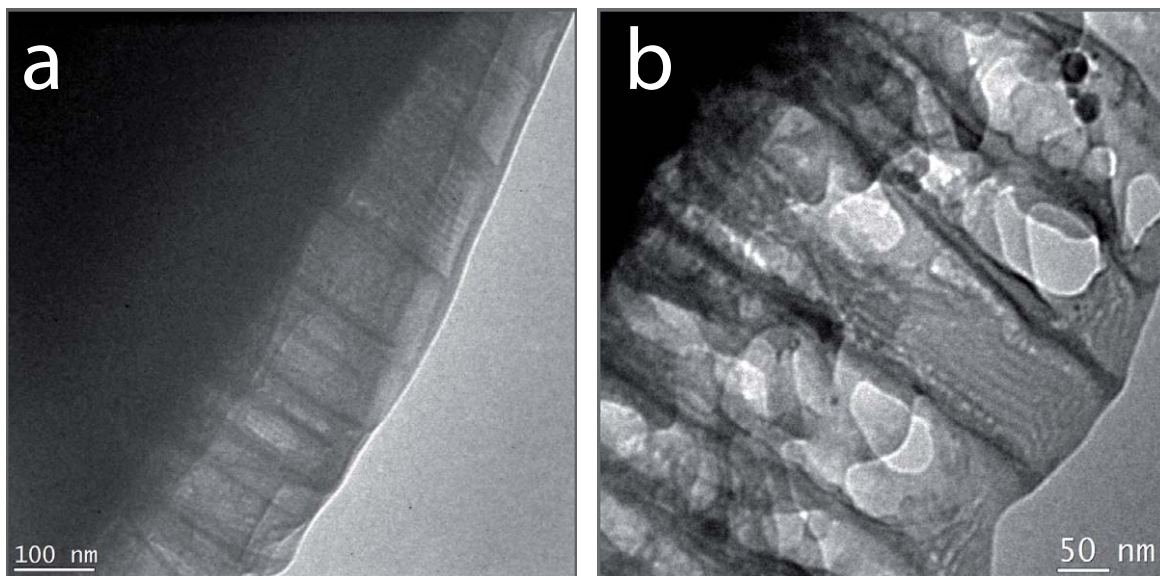


Figure 6.13 — TEM cross-sectional micrographs of composites prepared by a) casting and b) dip-coating with the precursor solutions.

Conclusion. The first results that were obtained from the experiments already demonstrate the high potential of this strategy. By being able to control not only the conditions during the EISA process, but having the control over the anopore morphology in combination with the lower aspect ratio one can synthesize almost defect-free composite materials. Further optimization of the synthesis protocol and the conditions present during the EISA process could finally lead to a hexagonal columnar mesophase without any circular side phase. These systems would then be ideal substrates for the subsequent nanowire growth by electrodeposition or other techniques.

Periodic Mesoporous Organosilicas in Confined Environments

Contents

7.1	Introduction	158
7.2	Experimental	160
7.3	Results and discussion	162
7.3.1	CTAB-template	162
7.3.2	Brij 56-template	163
7.3.3	Removal of the template	166
7.3.4	Replication of the porous system	169
7.3.5	Additional details	171
7.4	Conclusions and perspectives	177

This chapter is based on the article “Periodic Mesoporous Organosilica in Confined Environments”, published in Chemistry – A European Journal.^[107]

7.1 Introduction

Surfactant-driven synthesis of mesoporous silicates has been a field of extensive research since their discovery by Mobil Oil researchers in 1992.^[36] These kinds of materials are expected to offer a wide field of potential applications, such as separation, drug delivery, support for various catalysts, or as host for the synthesis of nanostructures.^[167,236–238] The combination of the advantages of inorganic mesoporous silicas such as tunable pore sizes (between 2 nm and 15 nm), high specific surface areas, and ordered pore systems with the great diversity of organic chemistry led to the development of mesoporous organic-inorganic hybrid materials.^[10] The organic modification of the porous materials allows one to tailor the properties of the inorganic silica to specific needs. A special group in this field of materials is represented by periodic mesoporous organosilicas (PMO), which were discovered in 1999.^[117,119] They can be synthesized from bis(alkoxysilyl) precursors in the presence of surfactants such as tetraalkylammonium halides or nonionic triblock-copolymers acting as structure-directing agents. This approach permits a high loading of organic functional groups, which are homogeneously distributed throughout the silica matrix. By choosing appropriate linker molecules it is also possible to synthesize PMO materials that exhibit various new and interesting properties unknown in purely siliceous mesostructured materials, such as crystal-like pore walls.^[120,239]

To date, PMO materials have been synthesized in the form of powders and thin films. In thin films, the alignment of the pore system is usually parallel with respect to the substrate (see, however, recent reports on mesoporous silica films with other orientations^[76,77,80]). Recently, the incorporation of mesostructured silica within the

pores of anodic aluminum oxide (AAO) membranes has been reported.^[81,95–97,100,102,110] These types of composite materials permit the synthesis of mesopores aligned perpendicular to the membrane surface. The synthesis was achieved by employing evaporation-induced self-assembly (EISA).^[58] These composites can offer significant advantages over thin films, such as high mechanical stability and high aspect ratios of the mesophase system, making them excellent candidates for applications such as separations, nanofiltration or nanotemplating. Due to the confinement of the silica within the alumina pores, the formation of unusual mesophase morphologies was observed. There have been reports on a 2D hexagonal columnar mesophase (mesopore orientation along the alumina pore), a 2D hexagonal circular mesophase (mesopore orientation perpendicular to the alumina pore), and a circular lamellar phase.^[97,100]

Here we report on the synthesis of PMO materials based on bis(triethoxysilyl)ethane (BTSE) confined within the pores of anodic alumina membranes. In addition to the previously reported 2D hexagonal circular phase and the lamellar phase, for the first time we observed a circular phase that was formed by an ionic surfactant. Furthermore, the existence of a 3D porous system (cubic $Im\bar{3}m$) was observed, which has not yet been reported for these types of confined materials. These hierarchical systems offer excellent fill factors in the alumina channels and very high surface areas.

7.2 Experimental

General synthesis. Whatman Anodiscs (47 mm diameter, nominal pore diameter 0.02 μm) were used as porous alumina substrates. SEM measurements showed that these membranes have an effective pore diameter between 150 and 250 nm. Bis(triethoxysilyl) ethane (BTSE, 98 %, Gelest) served as silica precursor. Non-ionic decaethylene glycol hexadecyl ether (Brij 56, Aldrich) as well as ionic hexadecyltrimethylammonium bromide (CTAB, Aldrich) were used as structure directing agents. All chemicals were used without further purification. PMO mesophases were synthesized in a two step method similar to previous reports.¹⁴ A first solution containing 1.72 g (5 mmol) BTSE, 1.92 g H₂O (107 mmol), 3.0 g HCl (0.2 M, 0.6 mmol of HCl), and 3.84 g (83 mmol) of Ethanol were mixed in a closed plastic beaker and pre-hydrolyzed for one hour at 60 °C. Meanwhile, another solution containing various amounts of the structure directing agent was prepared. For CTAB and Brij 56, 0.800 g of water, 1.500 g of HCl (0.2 M, 0.3 mmol of HCl), and 3.785 g of Ethanol were mixed with the respective SDA. In case of CTAB, amounts of 0.72 g up to 3.28 g, corresponding to 2 - 9 mmol of CTAB were dissolved in this solution. When using Brij 56 as SDA, 0.546 g (0.8 mmol, B1), 0.684 g (1 mmol, B2), or 0.956 g (1.4 mmol) of Brij 56 were dissolved, respectively. Finally, both the solutions, containing the silsesquioxane and the SDA, were mixed and a volume of 0.75 ml was cast onto the anodic alumina membrane. In case of laboratory experiments, this membrane was laying on a flat PTFE substrate, while for GISAXS experiments at the synchrotron, the membrane was lying on a grooved PTFE plate (grove width 0.5 cm, depth 0.4 cm).

Calcination protocol. The samples with Brij 56 as SDA were calcined using a multi-

ple step calcination protocol. In a first ramp (0.5 °C/min) the samples were heated from room temperature up to 120 °C. This temperature was held for at least five hours. This step was followed by another ramp (0.5 °C/min) up to 180 °C, which was kept constant for another five hours. After that the samples were finally heated up to either 200 °C or 250 °C with a heating rate of 0.25 °C/min, this final temperature was kept for 10 hours for complete surfactant removal.

Electrodeposition of nickel. For the deposition of nickel within the mesopores, a small fragment of the calcined composite material (B2) was sputtered on one side with a thin gold layer acting as electrode material and connected to a wire using silver paint. Finally the electrode was isolated against the electrolyte solution using nail polish. The electrolyte solution was composed of 30 g/l NiCl₂ · 6 H₂O, 100 g/l NiSO₄ · 6 H₂O, and 40 g/l H₃BO₃.

Characterization. TEM micrographs were recorded using a JEOL 2011 transmission electron microscope, the acceleration voltage was set to 200 kV. Nitrogen sorption measurements were carried out at 77 K using an Autosorb-1 by Quantachrome Instruments. 2D small angle X-ray scattering experiments were carried out using the SAXSess system by Anton Paar in combination with a CCD detector system (Roper Scientific). The wavelength of the incident beam is 0.154056 nm (Cu K_α), the sample-detector distance was set to 307.8 mm. Samples were measured with a tilt angle of 10° with respect to the primary beam. GISAXS experiments were performed at beamline BL 5.2 L at Sincrotrone Elettra (Trieste, Italy). The wavelength of the incident beam was 0.154980 nm (8 keV), and the sample-detector distance was 641.7 mm. The incident angle of the beam to the substrate was 2.35° in a transmission mode. The substrate was placed on a grooved PTFE plate (groove width 0.5 cm, depth 0.5 cm). Solid state NMR measurements were performed using a

Bruker DSX Avance 500 FT.

7.3 Results and discussion

7.3.1 CTAB-template

Hexadecyltrimethylammonium bromide is a commonly-used template in the synthesis of mesoporous materials. In the CTAB/Silica/AAO system, the only mesophase previously found for these composites has a hexagonal columnar structure. To determine the structure of the new CTAB/PMO/AAO mesophase systems, 2D - small angle X-ray scattering (SAXS) experiments in combination with TEM were performed. In contrast to our previous results on inorganic silica/AAO composites, the SAXS patterns for the confined PMO systems showed only evidence for the hexagonal circular mesophase (Figure 1a).^[96] The average d-spacing calculated from the SAXS patterns was 4.5 nm. Additionally, TEM micrographs of this phase (Figure 1b) confirm the formation of the hexagonal circular phase. The d-spacing calculated from the electron micrographs is 4.0 nm, somewhat smaller than the d-spacing resulting from X-ray-diffraction. This can be attributed to the shrinkage of the porous system during the ion milling procedure, which is a crucial step in the TEM specimen preparation, as well as the effect of the exposure to the electron beam under vacuum in the TEM column.

In comparison to silica, the remarkably different PMO structures formed during the EISA process could be the result of a change in polarity and size of the organo-silica species in the PMO phase. This might lead to different interactions between the

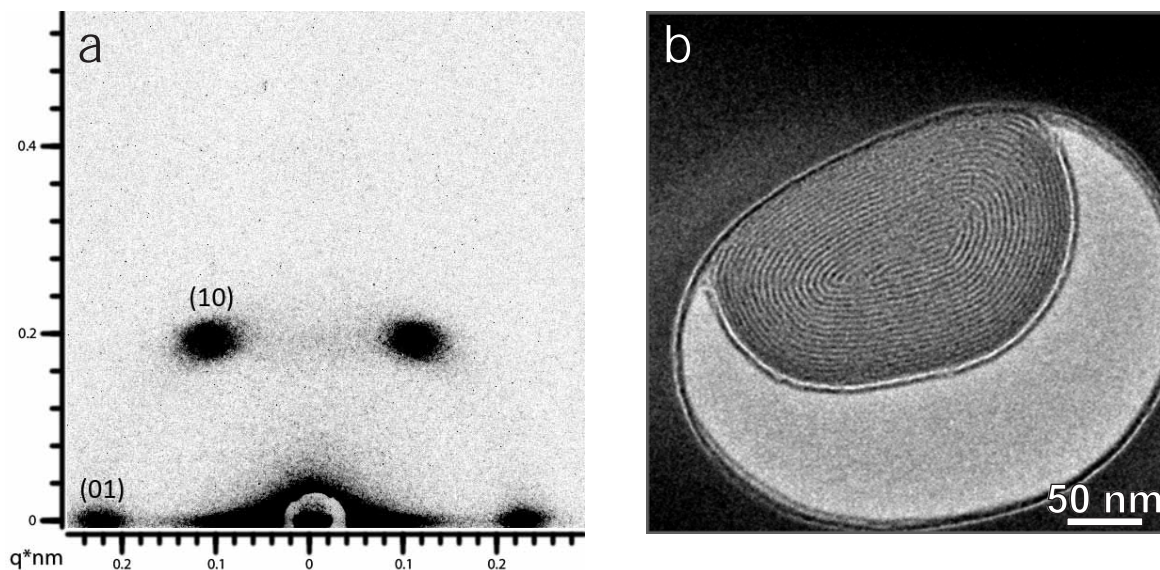


Figure 7.1 — a) 2D-SAXS pattern and b) TEM micrograph of CTAB-based as-synthesized composite material representing the circular hexagonal mesophase.

SDA and the organosilica wall material, making the hexagonal circular mesophase favorable over the hexagonal columnar one.

7.3.2 Brij 56-template

The use of Brij 56 as a structure directing agent for EISA synthesis resulted in the formation of two different mesophases. For SDA/BTSE ratios above 0.09 (sample B2), the formation of a circular mesophase was observed by SAXS (Fig. 7.2 (a)), yielding the typical diffraction pattern for this mesophase.^[96,100] The average d-spacing calculated from the diffraction pattern is 5.8 nm, which is in agreement with the corresponding TEM data (Fig. 7.2b). At a SDA/BTSE ratio between 0.06 and 0.08 (sample B1), the formation of a previously unknown structure for mesophases

confined within the pores of AAO membranes was detected.

X-ray diffraction in a laboratory SAXS experiment (incident angle 10° with respect to the AAO membrane surface) revealed six reflection spots above the horizon (instrumental lower limit) (inset in Fig. 7.2 c) with an average d-spacing of again 5.8 nm. In contrast to these results, experiments carried out at the Elettra synchrotron resulted in a diffraction pattern known from literature for cubic $Im\bar{3}m$ phases (Fig 7.2 (c)).^[240,241] The d-spacing of the indexed 110 reflections of 5.8 nm is the same as for the laboratory experiments. The difference in the diffraction patterns from the laboratory instrument and the ones obtained at the synchrotron can be explained by the different measurement geometries.^[242] Due to the relatively low photon flux and the larger beam size of the in-house diffractometer, the incident angle of the beam with respect to the sample has to be set to 10° in order to observe diffraction patterns intense enough for evaluation. Using the high photon flux of the synchrotron, it was possible to reduce the incident angle to 2.353° , resulting in the diffraction patterns depicted in Figure 2c. The same patterns could also be obtained with the laboratory instrument at a low angle of incidence, but the data quality did not permit quantitative evaluation. TEM data obtained from this cubic phase support the formation of a cubic $Im\bar{3}m$ mesophase. The micrograph depicted in Figure 2d shows a view along the [110] zone axis, with the mesophase perfectly aligned to the anopore curvature. The distances of the structural elements are 3.9 nm and 5.8 nm (corresponding to d_{110}), which is in very good agreement with the X-ray diffraction data (showing only the reflections for the [110] zone axis). The calculation of the d-values along the [111] direction and a corresponding TEM micrograph can be found in the supporting information.

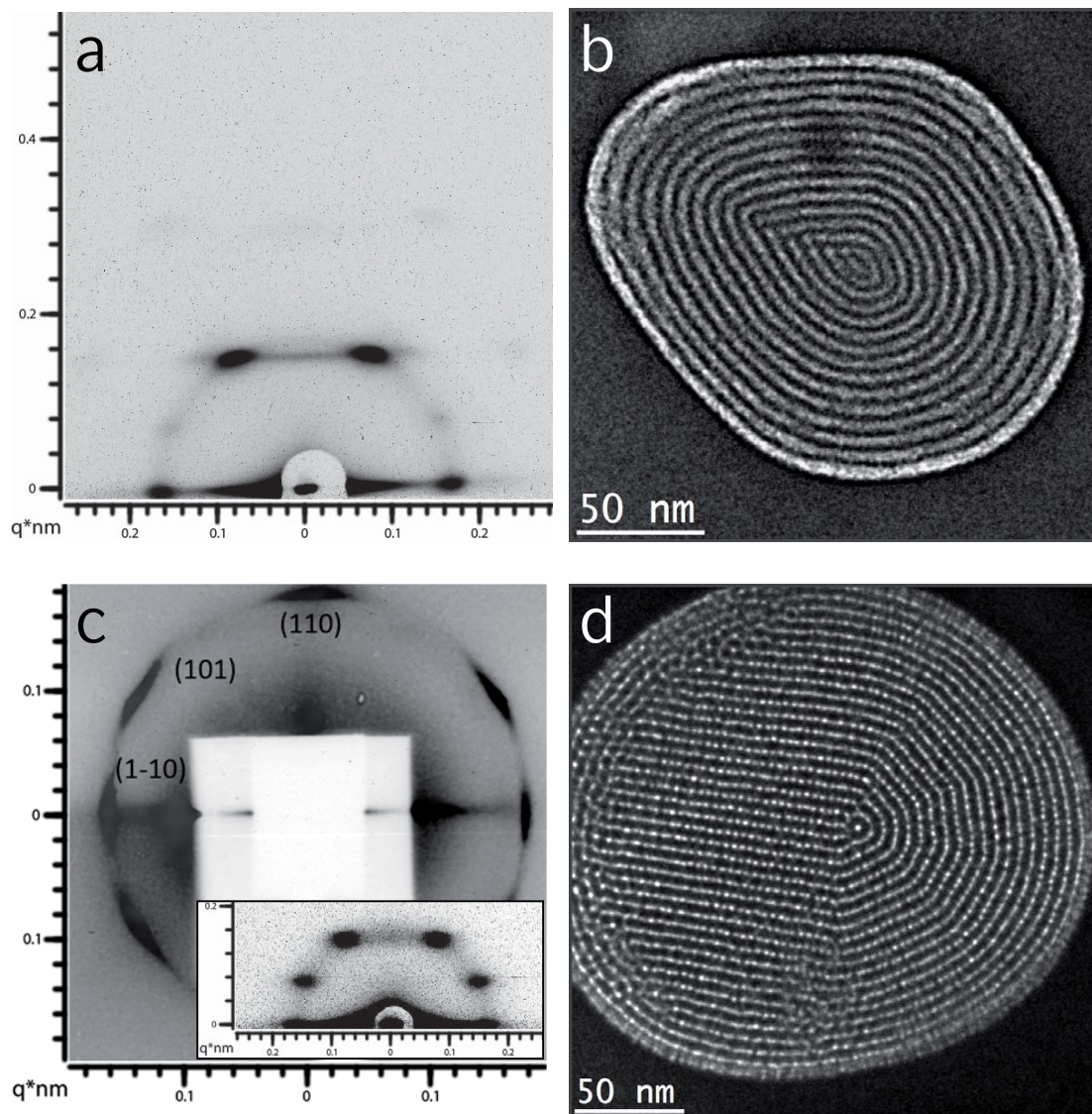


Figure 7.2 — a) 2D SAXS diffraction pattern (obtained from the laboratory SAXS equipment) and b), corresponding TEM micrograph showing the hexagonal circular mesostructure of a calcined sample B2-c. c) SAXS diffraction pattern of the cubic $Im\bar{3}m$ mesophase (sample B1) obtained at the Elettra synchrotron. The inset shows a diffraction pattern of the same phase recorded with our laboratory SAXS machine. d) Corresponding TEM micrograph along the [110] zone axis of an as-synthesized sample.

7.3.3 Removal of the template

The removal of the surfactant template molecules from the mesophases to form open pore systems is a crucial step for possible applications of these hybrid materials. For powdered materials a variety of methods such as extraction, calcination, or surface modification^[243] can generally be used. However, standard extraction techniques (using EtOH/HCl) of the as-synthesized PMO/AAO samples always resulted in a complete loss of structure. Surface modification with silane coupling agents can work well for the removal of surfactants (SDA) from inorganic silica in AAO membranes, but this route fails for PMO materials within AAO, as it cannot completely remove the SDA. The destruction of the mesophase in both cases is tentatively attributed to the low degree of condensation of the silica network and the HCl attacking the alumina. To increase the degree of condensation and thus strengthen the structure, the samples were annealed at 120 °C and subsequently extracted in pure ethanol. For both sample types, X-ray diffraction confirmed the retention of the previously formed mesophase (Figure 7.3).

The nitrogen sorption isotherm of a cubic, template-extracted sample annealed at 120 °C (Fig.7.3 a) gives a BET surface area of 60 m²/g and a pore volume of 0.04 ml/g. This is in accordance with literature data for comparable silica/AAO composites.^[96] As indicated by the shape of the capillary condensation step and the hysteresis in the isotherm, the sample shows a relatively broad pore-size distribution with sizes ranging between 2 and 6 nm and an average of about 4 nm. This is attributed to the incomplete removal of the surfactant molecules during extraction, thus creating pores with different local diameters and some tortuosity. Accordingly, ¹³C-MAS-NMR data of the corresponding sample (Figure 5a) show intensive sig-

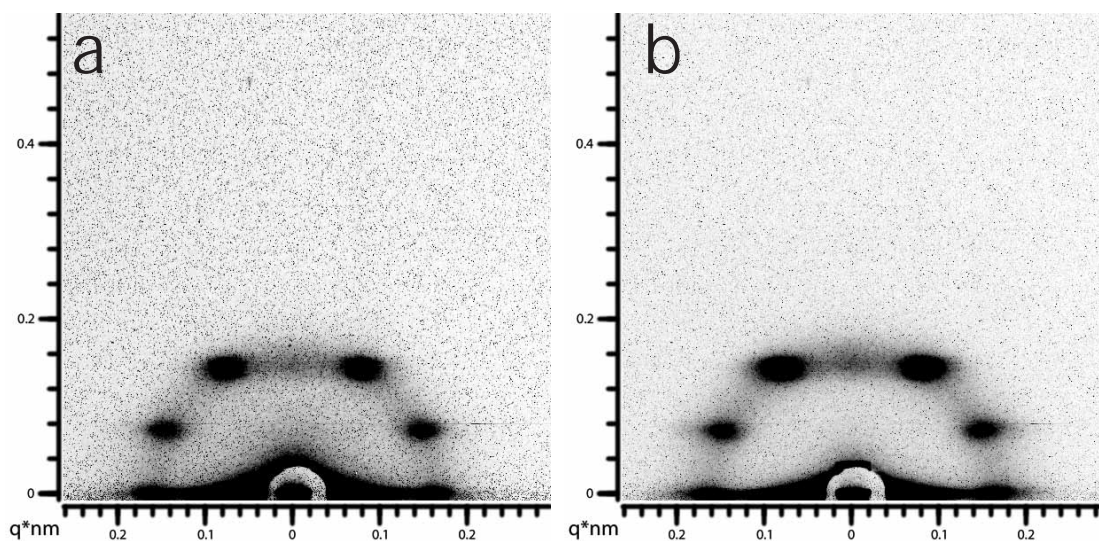


Figure 7.3 — 2D SAXS patterns of a sample B1 annealed at 120 °C. a) Before extraction, b) after extraction with ethanol.

nals representing Brij molecules, indicating that the removal is not yet completed.

At a calcination temperature of 200 °C in air, the decomposition of the SDA is already far advanced and a subsequent extraction with ethanol is no longer needed. The BET surface area of 70 m²/g, calculated from the nitrogen sorption isotherm, is in the expected range for these types of composite systems, but ¹³C MAS NMR measurements indicate that the removal of the Brij molecules from the mesophase is not yet complete (Figure 5a). ²⁹Si NMR of the calcined sample also already exhibits a minor broad signal around -100 ppm, which can be assigned to Q_n sites, indicating the beginning cleavage of the organic linker groups. The X-ray diffraction pattern of a sample calcined at 250 °C yields the strongest reflection intensities, the highest surface area (85 m²/g) and the sharpest pore size distribution. The corresponding ²⁹Si spectrum shows signals for the T-Species at around -60 ppm, indicating that the majority of the Si-C bonds were not oxidized upon calcination. The second signal

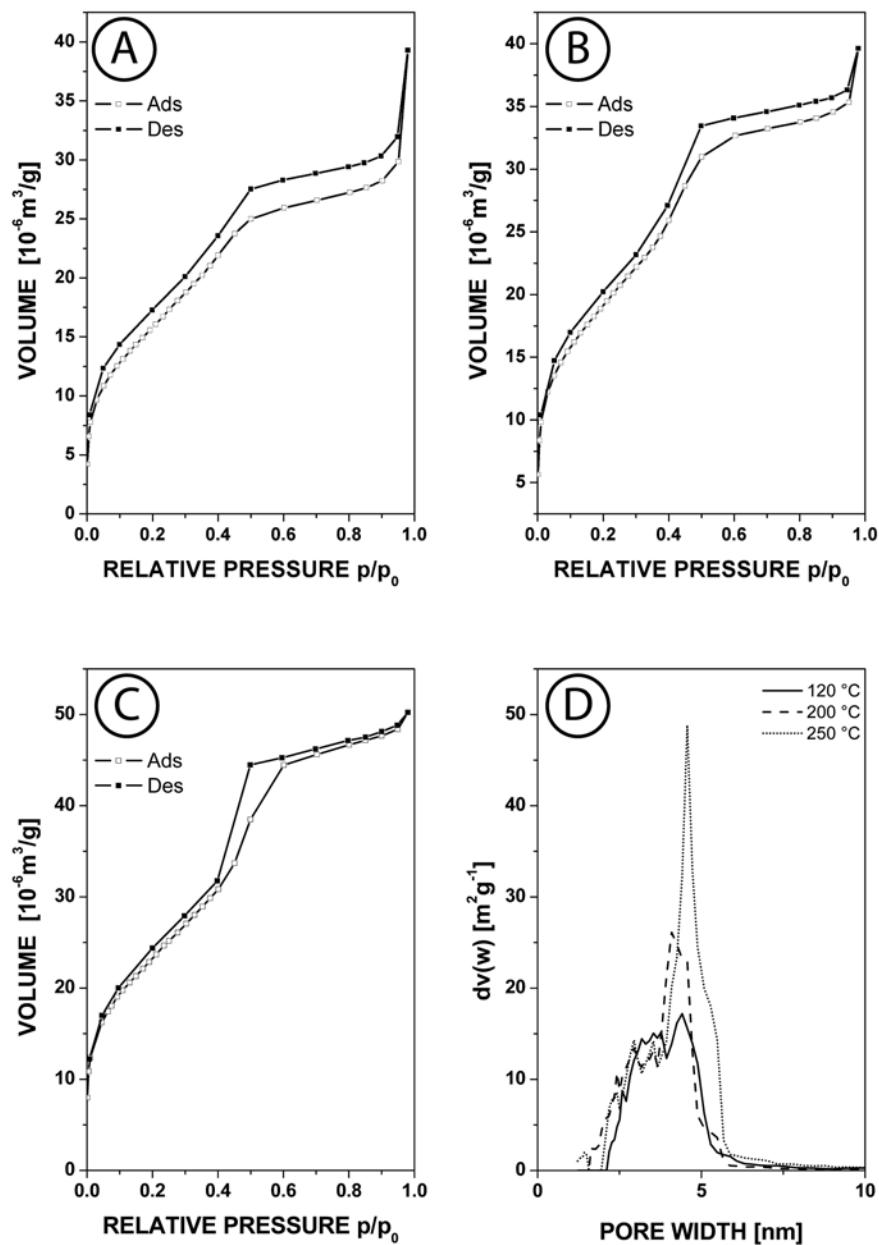


Figure 7.4 — Sorption isotherms of template-removed composites synthesized using Brij 56 as the SDA. a) Sample annealed at 120 °C and subsequently extracted in ethanol, b) and c) correspond to calcined samples, of which the sample in b) has been calcined at 200 °C, and the sample in c) has been calcined at 250 °C. d) shows the corresponding pore size distributions of samples a) to c) (calculated using a DFT model from the adsorption branch).

at around -99 ppm can be assigned to Q_n -sites ($x=1$ to 4). These signals originate from $Si-O_x$ species, so some of the ethylene bridges were cleaved. Heating to even higher calcination temperatures will result in a total cleavage of the organic groups. However, even at a calcination temperature of 500 °C the mesostructure itself stays intact.

7.3.4 Replication of the porous system

Potential applications of these hierarchical systems in nanofiltration and other fields require that the porous system is accessible for ions and molecules over the complete 60 μm length of the pores. In order to evaluate access into the PMO/AAO systems, the pores of a calcined (250 °C, see Experimental section) hexagonal circular sample (B2) were replicated by the electrodeposition of nickel. The general possibility of using silica/AAO composites as nanotemplates has been reported before.^[138] After the electrodeposition, the sample showed some islands of bulk nickel on the membrane surface opposite to the electrode. TEM samples were prepared by grinding and ion-polishing a specimen close to the electrode surface. TEM micrographs (Figure 7.6) reveal the successful replication of the pore geometry by the deposited nickel. Electron diffraction on individual, filled mesopores indicates that the nickel is crystalline. The electrodeposition only took place in some isolated pores with the majority of the pores still empty. This can be attributed to the fact that the pore system is mainly formed by the circular hexagonal phase and only some pores exhibit the helical system (or defects) with access to the gold electrode throughout the whole length of the 60 μm anopores.

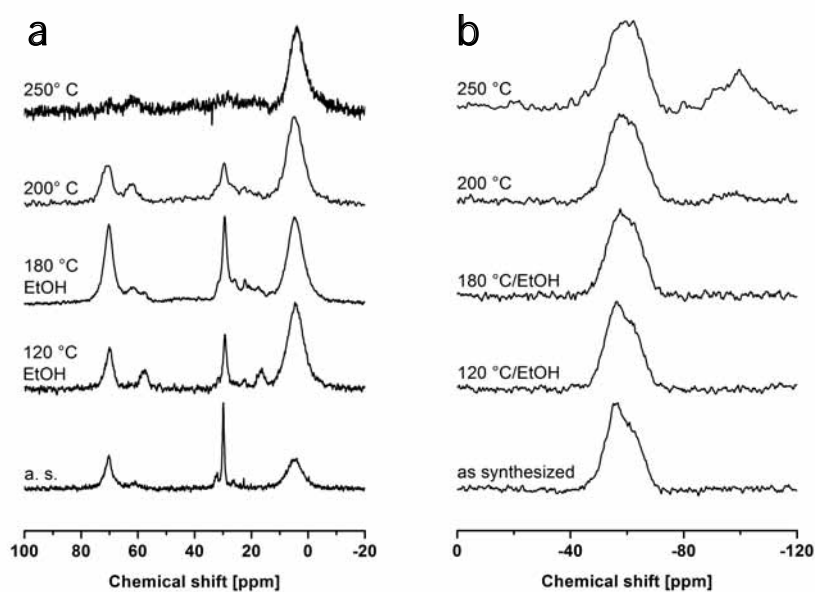


Figure 7.5 — NMR spectra of the PMO/AAO samples treated under different conditions to remove the surfactant. a) ^{13}C -MAS-NMR spectra of cubic samples. Compared to the as-synthesized sample at the bottom, the signals originating from the Brij molecules (at around 30 and 70 ppm, respectively) decrease for the extracted sample and the sample calcined at 200 °C. At a calcination temperature of 250 °C, the surfactant signals can be hardly recognized (all spectra are normalized to the signal of the ethylene bridges at 4.5 ppm; the a.s. spectrum was scaled down by a factor of 3 to fit the graph). b) ^{29}Si spectra of cubic samples before (bottom) and after the different steps of template removal. The signal at -60 ppm corresponds to T-sites, while the broad resonance at -99 ppm corresponds to Q-sites, indicating the beginning decomposition of the ethylene bridges.

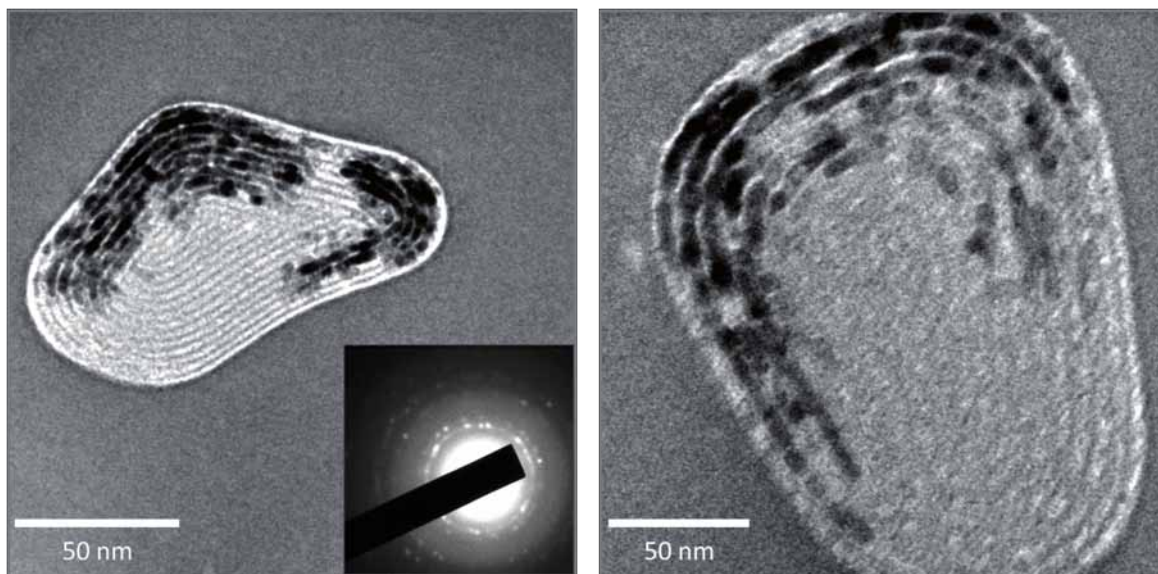


Figure 7.6 — TEM micrograph of PMO mesopores filled with nickel by electrodeposition. The inset in the left micrograph shows an electron diffraction pattern from a few wires.

7.3.5 Additional details

Benzene-bridged PMO. The above discussed results dealt only with the relatively simple ethylene-bridged PMO precursor. However, ordered PMO mesophases within the pores of AAO membranes could also successfully be synthesized using a benzene-bridged precursor, bis(triethoxysilyl)benzene (BTSB). Some of the results presented here will be reported in a following publication.^[244] As already mentioned in the introduction, the use of aromatic precursor allows in principle the generation of “quasi-crystalline” PMO materials. Unfortunately, this is true only for PMO’s synthesized in alkaline media;^[120,245] a synthesis route, that is not applicable for alumina substrates due to their solubility in basic media. The benzene ring in the organosilica framework allows the introduction of diverse chemical moieties by reactions known from organic chemistry. An amination reaction of

benzene-bridged PMO thin films having crystal-like pore walls has recently been demonstrated by the Inagaki research group.^[246] The authors found high conversion rates (ca. 27 %), with the mesopore system and the crystal-like periodicity was retained well. The resulting materials could be used to catalyze a Knöevenagel condensation.



Figure 7.7 — Reaction scheme for the synthesis of bis(triethoxysilyl)benzene (BTSB).

Bis(triethoxysilyl)benzene (BTSB) was synthesized after Burleigh et. al by a Grignard reaction.^[247] A dry three-neck flask was equipped with a reflux condenser, a septum and a dropping funnel was flushed with nitrogen. Magnesium turnings (5.92 g, 244 mmol), THF (120 ml), tetraethoxy silane (178 ml, 800 mmol), and one iodine crystal were added. The solution was heated to reflux. To this, a solution of 1,4-dibromo benzene (18.9 g, 80.1 mmol) in THF (40 ml) was added drop wise within two hours. The solution was left to reflux for another hour. After cooling to room temperature, 200 ml of pentane were added to precipitate remaining MgBr_2 . The precipitate was filtered of and the solvent was evaporated in vacuum. After distillation at reduced pressure, BTSB was obtained in form of a clear, colorless oil (14.6 g, 36.3 mmol).

^{13}C NMR (68 MHz, CDCl_3): $\delta = 134.87, 134.10, 130.39, 77.55, 77.08, 76.61, 59.22, 58.83, 18.25$.

^{29}Si NMR (54 MHz, CDCl_3): $\delta = -57.54$.

The mesophase synthesis described here followed the EISA protocol of the BTSE

mesophases (see Section 7.2, p. 160). The synthesis of CTAB templated composites followed exactly the synthesis steps as described already above for BTSE with the only exemption that BTSE was substituted by corresponding amounts of BTSE. Composites with Brij 56 or Pluronic acting as the SDA were prepared by the following steps: In a small plastic beaker, a solution containing BTSE (0.50 g, 1.25 mmol), 0.2 M HCl (0.75 g, 0.15 mmol of HCl), water (0.48 g, 68 mmol including the water content from the 0.2 M HCl), and absolute ethanol (0.96 g, 21 mmol) were thoroughly mixed. Because of an enhanced hydrolysis rate of the BTSE precursor, the prehydrolysis time at 60 °C was reduced to 10 minutes. If Brij 56 was used as the SDA, a solution containing Brij 56 (0.273 g), water (0.75 g, 42 mmol) and ethanol (3.785 g, 82 mmol) was added to the prehydrolyzed solution. Samples with Pluronic P123 as the surfactant were synthesized by adding various amounts of 5 weight-% solution of P123 in Ethanol to the prehydrolyzed solution. The formation of the circular hexagonal phase was observed after adding 7.33 g of the ethanol/P123 mixture to the solution containing the BTSE precursor. After extensive mixing, 0.75 ml of the respective solutions were cast onto one Anodisc.

The experiments were carried out using either CTAB, Brij 56, or Pluronic P123 as the SDA. In contrast to the experiments with BTSE, no ordered mesophases were obtained with CTAB at similar BTSE/SDA molar ratios. Representative SAXS patterns only revealed the diffuse scattering resulting from the host membrane itself. The synthesis of mesophases templated by Brij 56 more was more successful; in this case disordered (wormlike) phases were found in TEM images of as-synthesized specimens (Fig. 7.8). Corresponding SAXS patterns did not show any distinct reflection spots indicating an ordered mesostructure.

Ordered benzene-bridged PMO mesophase within anodic alumina pores could only

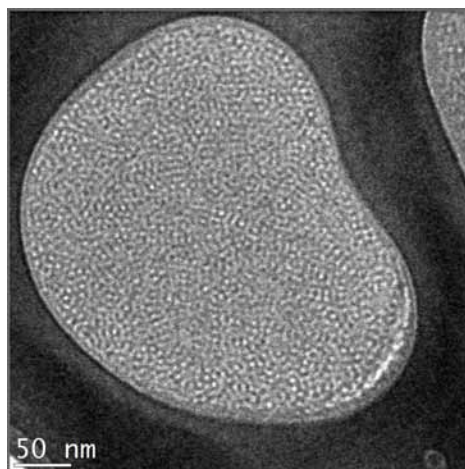


Figure 7.8 — Representative TEM micrograph of the wormlike BSB mesophase templated by Brij 56.

be obtained with Pluronic P123 acting as the SDA. The SDA : Si ratio was varied in the range from 1 : 0.013 to 1 : 0.035. The formation of an ordered, hexagonal circular mesophase was found for ratios above 0.021. TEM micrographs (Fig. 7.9a) indicate good fill rates with the mesostructured material. Also, only a minor shrinkage of the PMO filaments was observed. SAXS experiments showed the characteristic reflections of the hexagonal circular mesophase (Fig. 7.9b).

One possible major advantage of benzene-bridged PMO material over the ethylene-bridged material is its higher thermal stability against decomposition; thus, calcination experiments could be carried out at higher temperatures. Measurements by differential thermal analysis (DTA) showed the decomposition of the benzene-silica wall material starting at temperatures around 300 °C. At this temperature the SDA molecules are already completely decomposed (see above). These findings were also supported by NMR measurements (Fig. 7.9c). Nitrogen sorption data of the calcined samples showed BET surface areas of 49 m²/g.

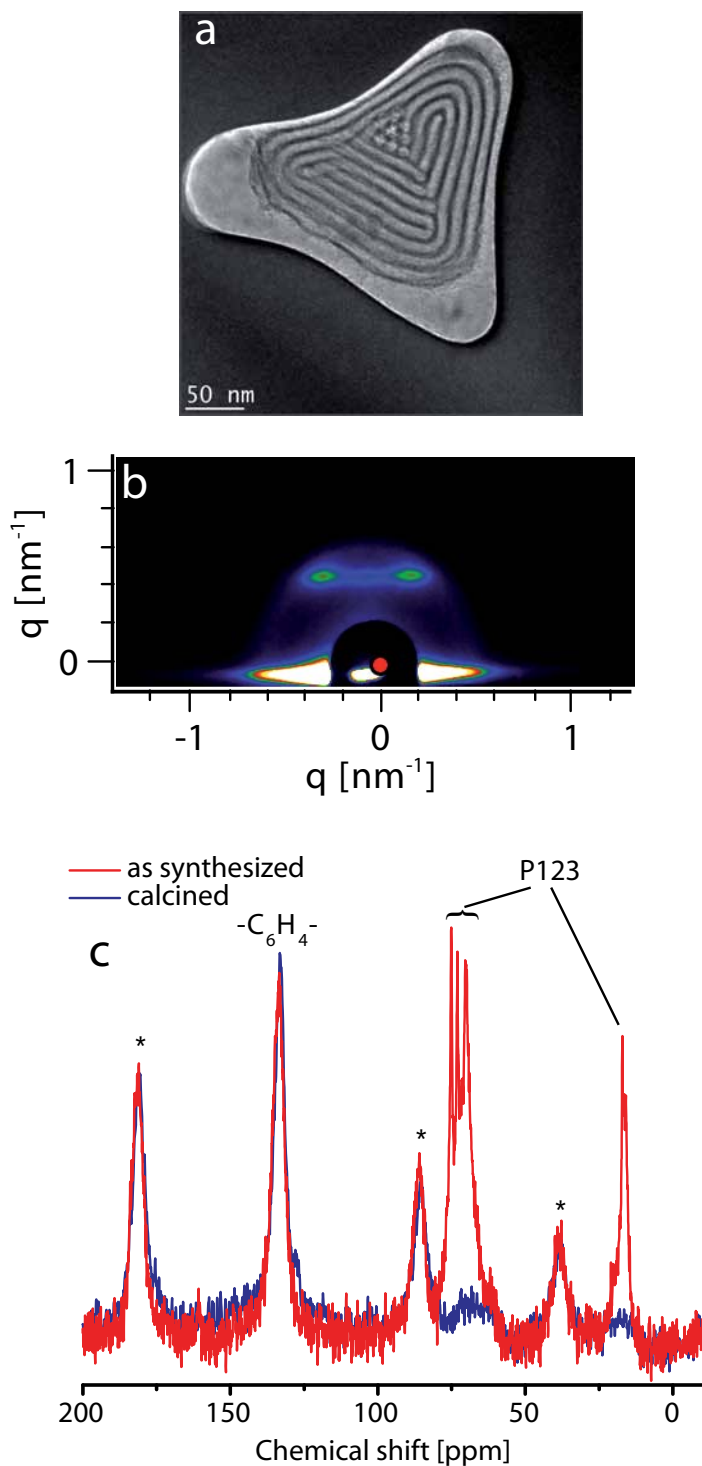


Figure 7.9 — a) TEM micrograph and b) SAXS data of an as-synthesized benzene-bridged PMO. c) ¹³C MAS-NMR data obtained from an as-synthesized benzene-bridged PMO sample and from a sample calcined at 250 °C. Bands marked with an asterisk (*) are rotational side-bands.

Addition of salts. Experiments with purely siliceous mesoporous material within anopores – when using non-ionic surfactants – have shown that the phase formation process can be influenced by the addition of small amounts of inorganic salts.^[103,136] In combination with a precise control of the temperature and the relative humidity during the EISA process, composite membranes with a high fraction of the hexagonal columnar phase can be synthesized. Similar experiments have been carried out for PMO material (with BTSE and BTSB as precursors) in order to synthesize hexagonal columnar PMO mesophases within AAO pores.

Ethylene bridged samples were synthesized from the BTSE precursor in the presence of Pluronic P123 as the SDA at three different humidities (28 %, 55%, and 96 % r.h.). The compositions of the precursor solutions was identical to those discussed already for the BTSB precursor. As expected, SAXS measurements showed the formation of the hexagonal circular mesophase. Nevertheless, the reflex intensity in the SAXS experiment increased strongly with an increase in humidity. This corresponds to the findings obtained from composites synthesized from TEOS and P123.^[136] The calcination of these membranes leads to a broadening of the reflections, indicating an inhomogeneous shrinkage of the porous system. This was supported by corresponding TEM micrographs. By the addition of LiCl (0.04 g) to the respective precursor solutions it was possible to increase the ratio of the hexagonal columnar phase over the hexagonal circular phase, as indicated by TEM micrographs (Fig. 7.10a). These results were qualitatively supported by corresponding SAXS measurements (Fig. 7.10); nevertheless, as it was not possible to synthesize membranes with the columnar phase as the main phase, no numerical evaluation of the patterns (by calculating the oop/ip ratio) was done.

Very similar results were obtained for the BTSB system. The reflection intensity in

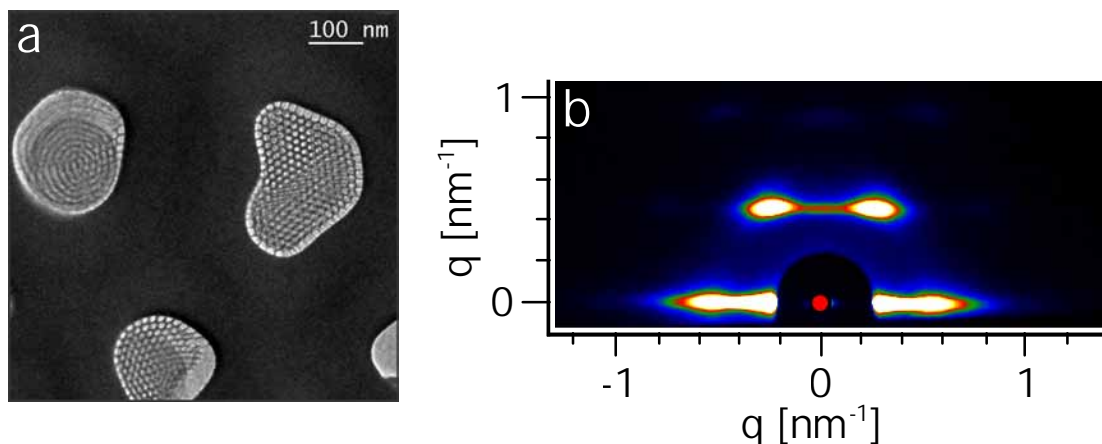


Figure 7.10 — TEM image (a) of a composite membrane synthesized from BTSE as the organosilica precursor in the presence of LiCl. The formation of hexagonal columnar domains is clearly visible. The corresponding SAXS diffractogram (b) shows that there is still a high fraction of the hexagonal circular phase present.

the SAXS experiments increased with increasing humidity; thus, better ordered systems were obtained. Furthermore, the synthesis of partially columnar mesophases by the addition of lithium chloride to the EISA precursor solution was achieved. Nevertheless, it was still not possible to get a pure hexagonal columnar phase.

7.4 Conclusions and perspectives

In summary, PMO mesophases based on the ethylene-bridged silsesquioxane BTSE have been successfully synthesized within the pores of anodic alumina membranes. Depending on the surfactant used, different mesophases were observed. SAXS experiments and TEM measurements carried out on CTAB-based PMO/AAO composites yielded exclusively the diffraction patterns and images characteristic for a hexagonal circular mesophase. This contrasts with purely siliceous, CTAB-tem-

plated AAO composites, where the hexagonal columnar structure is the exclusive phase.

Furthermore, for the first time a cubic $Im\bar{3}m$ phase was found in these confined environments when using Brij 56 as structure directing agent. The existence of this phase was proven by X-ray scattering experiments (SAXS) as well as electron microscopy (TEM). Nitrogen sorption data show that most of the template from these hierarchical systems can be removed by annealing at 120 °C and subsequent acidic ethanol extraction. Furthermore, we were able to calcine the samples using a step-wise calcination protocol while retaining the majority of the organic functionality in the pore walls. ^{13}C -NMR data show that the template was removed completely at a calcination temperature of 250 °C. In addition, ^{29}Si NMR data proved that the majority of the ethylene linker bridges survived this treatment, leading to higher surface areas as compared to the extracted material. The successful template removal from the cubic mesophase makes this kind of composites interesting for applications in nanofiltration or as membranes.

The structure of a hexagonal circular mesophase could be successfully replicated by electrochemically filling the mesopores with nickel. This illustrates that the porous system is accessible for molecules and ions throughout the whole membrane length of 60 microns.

Finally, additional experiments with benzene-bridged PMO/AAO systems showed that it is also possible to synthesize mesoporous PMO/AAO composites with chemically more attractive bridges. Current experiments show that it is even possible to synthesize PMO mesophases with biphenyl bridges.^[244] These kind of composites show promising optical properties.

General Conclusions

In the course of this thesis, metal and semiconductor nanowires have been prepared within porous host systems. For this challenging task, the synthesis and characterization of corresponding host materials was an important part of the project.

Porous anodic alumina substrates are widely used for the synthesis of nanowires of all kinds. The new multicontact horizontal AAO design introduced in Chapter 5 further expands the possibilities of this method. In a first step, several horizontal aluminum finger structures were prepared on silicon wafers using lithography. Each of these fingers could be contacted individually, allowing the directed anodization of each finger. Thus, different anopore morphologies could be obtained on a single chip. These individual anodic alumina finger structures could then be filled in a second step with metals and semiconductors to create nanowire systems. By making it possible to create arrays of differently sized nanowires and/or even nanowires of different materials on a single silicon wafer, a new field of application of such systems in sensing and nanoelectronics is opening up.

The original aim of this thesis, the synthesis and characterization of metal and semiconductor nanowires within composite mesoporous host materials, has been suc-

cessfully demonstrated in Chapter 6. In this process, the synthesis and characterization of suitable hosts proved to be almost as challenging as the preparation, characterization, and final liberation of the nanowires from the host matrix. During the preparation of the mesoporous AAO/silica composites it became apparent that external influences – namely temperature and humidity during the EISA process – are key factors for the successful preparation of continuous, highly columnar mesostructures within the AAO pores. Even at optimized conditions, completely pure mesophases could not be obtained; the systems always showed orientational boundaries within the mesostructure switching from the hex. columnar arrangement to the hexagonal circular arrangement. This switching behavior could be visualized by a TEM study on silica/nanowire filaments dissolved from the alumina matrix. It was further shown, that it is possible to completely dissolve the complete AAO/SiO₂ host material, thus bundled silver nanowires could be obtained. One of the main challenges of this system - the ability to obtain pure, single-phase mesostructures - is addressed in the outlook of Chapter 6. First experiments showed already that it is indeed possible to obtain a pure mesophase by reducing the aspect ratio of the anopore system.

The concept of confining silica mesophases within the pores of anodic alumina was also adopted for the synthesis of periodic mesoporous organosilica mesophases (Chapter 7). Using an ethylene bridged silsesquioxane as the precursor, a variety of mesophases – including a formerly unknown cubic mesophase – could be synthesized within the AAO channel system. The hexagonal and the cubic mesophase were stable against surfactant removal by extraction or a mild calcination process. Sorption measurements of the resulting porous alumina/organosilica hybrids showed high BET surface areas. Finally, these composite membranes could also be

used for the successful preparation of nanowires.

While the aforementioned findings had the character of a “proof of principle”, further studies based on these experiments with chemically more attractive organic bridges have already been conducted in our group and will be continued. AAO/PMO composites with benzene bridges have been prepared, opening up the whole wide field of organic chemistry on aromatic systems. The biphenyl system shows interesting fluorescent properties. Furthermore, it is possible to synthesize mesostructures with a high degree of structural order, which has always been a challenge for these kind of PMO materials when synthesized in the form of thin films. These results will be published shortly in a following publication.^[244]

The chemistry of mesophases within AAO pores is not limited to silicates or oxides. In another upcoming publication,^[248] the synthesis of ordered mesoporous carbons (OMC) within AAO pores will be described. In contrast to OMC thin films, the mesoporous system does not shrink significantly if carbonized at temperatures as high as 1000 °C.

- [1] H. Zhao, Y. Ning, *Gold Bulletin* **2000**, 33, 103–105.
- [2] G. Cao, *Nanostructures and Nanomaterials: Synthesis, Properties, and Applications*, Imperial College Press, **2004**.
- [3] R. P. Feynmann, *Engeneering & Science* **1959**, 22–36, and <http://www.zyvex.com/nanotech/feynman.html>.
- [4] N. Taniguchi, *Proc. Intl. Conf. Prod. London Part II* **1974**, British Society of Precision Engineering.
- [5] A. Sandhu, *Nature Nano* **2006**, 1, 87–87.
- [6] <http://en.wikipedia.org/wiki/Nanotechnology> [Last accessed on 10.02.2010].
- [7] *Springer Handbook of Nanotechnology* (Ed.: B. Bhushan), Springer, Berlin, **2004**.
- [8] N. Petkov, PhD thesis, LMU München, Munich, **2004**.
- [9] M. E. Davis, *Nature* **2002**, 417, 813–821.
- [10] F. Hoffmann, M. Cornelius, J. Morell, M. Fröba, *Angewandte Chemie International Edition* **2006**, 45, 3216–3251.

- [11] G. Kickelbick, *Angewandte Chemie International Edition* **2004**, *43*, 3102–3104.
- [12] S. Polarz, B. Smarsly, *Journal of Nanoscience and Nanotechnology* **2002**, *2*, 581–612.
- [13] K. S. W. Sing, D. H. Everett, R. A. W. Haul, L. Moscou, R. A. Pierotti, J. Rouquerol, T. Siemieniewska, *Pure and Applied Chemistry* **1985**, *57*, 603–619.
- [14] F. Fischer, *Zeitschrift für anorganische Chemie* **1905**, *43*, 341–347.
- [15] G. E. Thompson, *Thin Solid Films* **1997**, *297*, 192–201.
- [16] *Handbook of Porous Solids, Vol. 3* (Eds.: F. Schüth, K. Sing, J. Weitkamp), Wiley-VCH, **2002**.
- [17] S. Shingubara, *Journal of Nanoparticle Research* **2003**, *5*, 17–30.
- [18] J. W. Diggle, T. C. Downie, C. W. Goulding, *Chemical Reviews* **1969**, *69*, 365–405.
- [19] L. Liu, W. Lee, R. Scholz, E. Pippel, U. Gösele, *Angewandte Chemie International Edition* **2008**, *47*, 7004–7008.
- [20] I. Lombardi, A. I. Hochbaum, P. Yang, C. Carraro, R. Maboudian, *Chemistry of Materials* **2006**, *18*, 988–991.
- [21] B. Platschek, A. Keilbach, T. Bein, *submitted*.
- [22] K. Heber, *Electrochimica Acta* **1978**, *23*, 127–133.
- [23] F. Keller, M. S. Hunter, D. L. Robinson, *Journal of The Electrochemical Society* **1953**, *100*, 411–419.
- [24] S. Ono, M. Saito, M. Ishiguro, H. Asoh, *Journal of The Electrochemical Society* **2004**, *151*, B473–B478.
- [25] W. Lee, R. Ji, U. Goesele, K. Nielsch, *Nature Materials* **2006**, *5*, 741–747.

- [26] European Standard EN 2536: Hard Anodizing of Aluminum Alloys, tech. rep., European committee for Standardization, **1995**.
- [27] IUPAC, *Pure and Applied Chemistry* **1972**, *31*, 577–638.
- [28] C. T. Kresge, M. E. Leonowicz, W. J. Roth, J. C. Vartuli, J. S. Beck, *Nature* **1992**, *359*, 710–12.
- [29] C. Li, Y. Wang, Y. Guo, X. Liu, Y. Guo, Z. Zhang, Y. Wang, G. Lu, *Chemistry of Materials* **2007**, *19*, 173–178.
- [30] D. Zhao, J. Feng, Q. Huo, N. Melosh, G. H. Fredrickson, B. F. Chmelka, G. D. Stucky, *Science* **1998**, *279*, 548–552.
- [31] P. T. Tanev, T. J. Pinnavaia, *Science* **1995**, *267*, 865–867.
- [32] N. R. B. Coleman, G. S. Attard, *Microporous and Mesoporous Materials* **2001**, *44-45*, 73–80.
- [33] N. K. Raman, M. T. Anderson, C. J. Brinker, *Chemistry of Materials* **1996**, *8*, 1682–1701.
- [34] Q. Huo, D. I. Margolese, U. Ciesla, D. G. Demuth, P. Feng, T. E. Gier, P. Sieger, A. Firouzi, B. F. Chmelka, F. Schüth, G. D. Stucky, *Chemistry of Materials* **1994**, *6*, 1176–1191.
- [35] D. Zhao, Q. Huo, J. Feng, B. F. Chmelka, G. D. Stucky, *Journal of the American Chemical Society* **1998**, *120*, 6024–6036.
- [36] J. S. Beck, J. C. Vartuli, W. J. Roth, M. E. Leonowicz, C. T. Kresge, K. D. Schmitt, C. T. W. Chu, D. H. Olson, E. W. Sheppard, et al., *Journal of the American Chemical Society* **1992**, *114*, 10834–43.

- [37] Y. Sakamoto, T. W. Kim, R. Ryoo, O. Terasaki, *Angewandte Chemie-International Edition* **2004**, *43*, 5231–5234.
- [38] C. Gao, H. Qiu, W. Zeng, Y. Sakamoto, O. Terasaki, K. Sakamoto, Q. Chen, S. Che, *Chemistry of Materials* **2006**, *18*, 3904–3914.
- [39] P. Yang, D. Zhao, D. I. Margolese, B. F. Chmelka, G. D. Stucky, *Chemistry of Materials* **1999**, *11*, 2813–2826.
- [40] D. Grosso, C. Boissiere, B. Smarsly, T. Brezesinski, N. Pinna, P. A. Albouy, H. Amenitsch, M. Antonietti, C. Sanchez, *Nature Materials* **2004**, *3*, 787–792.
- [41] M. J. MacLachlan, N. Coombs, G. A. Ozin, *Nature* **1999**, *397*, 681–684.
- [42] P. N. Trikalitis, K. K. Rangan, T. Bakas, M. G. Kanatzidis, *Nature* **2001**, *410*, 671–675.
- [43] U. Ciesla, S. Schacht, G. D. Stucky, K. K. Unger, F. Schüth, *Angewandte Chemie International Edition* **1996**, *35*, 541–543.
- [44] D. Sun, A. E. Riley, A. J. Cadby, E. K. Richman, S. D. Korlann, S. H. Tolbert, *Nature* **2006**, *441*, 1126–1130.
- [45] F. Schüth, *Angewandte Chemie International Edition* **2003**, *42*, 3604–3622.
- [46] M. Choi, R. Ryoo, *Nature Materials* **2003**, *2*, 473–476.
- [47] Q. Huo, D. Zhao, J. Feng, K. Weston, S. K. Buratto, G. D. Stucky, S. Schacht, F. Schüth, *Advanced Materials* **1997**, *9*, 974–978.
- [48] D. E. De Vos, M. Dams, B. F. Sels, P. A. Jacobs, *Chemical Reviews* **2002**, *102*, 3615–3640.

- [49] S. J. L. Billinge, E. J. McKimmy, M. Shatnawi, H. Kim, V. Petkov, D. Wermelle, T. J. Pinnavaia, *Journal of the American Chemical Society* **2005**, *127*, 8492–8498.
- [50] V. Rebbin, R. Schmidt, M. Fröba, *Angewandte Chemie International Edition* **2006**, *45*, 5210–5214.
- [51] C.-Y. Lai, B. G. Trewyn, D. M. Jeftinija, K. Jeftinija, S. Xu, S. Jeftinija, V. S. Y. Lin, *Journal of the American Chemical Society* **2003**, *125*, 4451–4459.
- [52] I. Roy, T. Y. Ohulchansky, D. J. Bharali, H. E. Pudavar, R. A. Mistretta, N. Kaur, P. N. Prasad, *Proceedings of the National Academy of Sciences of the United States of America* **2005**, *102*, 279–284.
- [53] B. Hatton, K. Landskron, W. Whitnall, D. Perovic, G. Ozin, *Advanced Functional Materials* **2005**, *15*, 823–829.
- [54] H. K. Baca, C. Ashley, E. Carnes, D. Lopez, J. Flemming, D. Dunphy, S. Singh, Z. Chen, N. Liu, H. Fan, G. P. Lopez, S. M. Brozik, M. Werner-Washburne, C. J. Brinker, *Science* **2006**, *313*, 337–341.
- [55] E. C. Carnes, D. M. Lopez, N. P. Donegan, A. Cheung, H. Gresham, G. S. Timmins, C. J. Brinker, *Nat Chem Biol* **2010**, *6*, 41–45.
- [56] Y. Lu, R. Ganguli, C. A. Drewien, M. T. Anderson, C. J. Brinker, W. Gong, Y. Guo, H. Soye, B. Dunn, M. H. Huang, J. I. Zink, *Nature* **1997**, *389*, 364–368.
- [57] D. Zhao, P. Yang, N. Melosh, J. Feng, B. F. Chmelka, G. D. Stucky, *Advanced Materials* **1998**, *10*, 1380–1385.
- [58] C. J. Brinker, Y. Lu, A. Sellinger, H. Fan, *Advanced Materials* **1999**, *11*, 579–585.
- [59] S. Besson, T. Gacoin, C. Ricolleau, C. Jacquiod, J.-P. Boilot, *Journal of Materials Chemistry* **2003**, *13*, 404–409.

- [60] F. Cagnol, D. Grosso, G. J. d. A. A. Soler-Illia, E. L. Crepaldi, F. Babonneau, H. Amenitsch, C. Sanchez, *Journal of Materials Chemistry* **2003**, *13*, 61–66.
- [61] D. Grosso, F. Cagnol, G. J. D. A. A. Soler-Illia, E. L. Crepaldi, H. Amenitsch, A. Brunet-Bruneau, A. Bourgeois, C. Sanchez, *Advanced Functional Materials* **2004**, *14*, 309–322.
- [62] M. Klotz, P.-A. Albouy, A. Ayrat, C. Menager, D. Grosso, A. Van der Lee, V. Cabuil, F. Babonneau, C. Guizard, *Chemistry of Materials* **2000**, *12*, 1721–1728.
- [63] M. L. Cohen, *Materials Science and Engineering: C* **2001**, *15*, 1–11.
- [64] Y. Xia, P. Yang, Y. Sun, Y. Wu, B. Mayers, B. Gates, Y. Yin, F. Kim, H. Yan, *Advanced Materials* **2003**, *15*, 353–389.
- [65] R. Rice, D. Arnold, M. Shaw, D. Iacopina, A. Quinn, H. Amenitsch, J. Holmes, M. Morris, *Advanced Functional Materials* **2007**, *17*, 133–141.
- [66] M. Trau, N. Yao, E. Kim, Y. Xia, G. M. Whitesides, I. A. Aksay, *Nature* **1997**, *390*, 674–676.
- [67] B. Tian, X. Liu, B. Tu, C. Yu, J. Fan, L. Wang, S. Xie, G. D. Stucky, D. Zhao, *Nature Materials* **2003**, *2*, 159–163.
- [68] K. Kuraoka, Y. Tanaka, M. Yamashita, T. Yazawa, *Chemical Communications* **2004**, 1198–1199.
- [69] A. Firouzi, D. J. Schaefer, S. H. Tolbert, G. D. Stucky, B. F. Chmelka, *Journal of the American Chemical Society* **1997**, *119*, 9466–9477.
- [70] Y. Yamauchi, M. Sawada, T. Noma, H. Ito, S. Furumi, Y. Sakka, K. Kuroda, *Journal of Materials Chemistry* **2005**, *15*, 1137–1140.

- [71] A. Jain, L. M. Hall, C. B. W. Garcia, S. M. Gruner, U. Wiesner, *Macromolecules* **2005**, *38*, 10095–10100.
- [72] H. Miyata, T. Noma, M. Watanabe, K. Kuroda, *Chemistry of Materials* **2002**, *14*, 766–772.
- [73] H. Miyata, T. Suzuki, A. Fukuoka, T. Sawada, M. Watanabe, T. Noma, K. Takada, T. Mukaide, K. Kuroda, *Nature Materials* **2004**, *3*, 651–656.
- [74] C. Liang, K. Hong, G. A. Guiochon, J. W. Mays, S. Dai, *Angewandte Chemie International Edition* **2004**, *43*, 5785–5789.
- [75] V. R. Koganti, S. E. Rankin, *Journal of Physical Chemistry B* **2005**, *109*, 3279–3283.
- [76] V. R. Koganti, D. Dunphy, V. Gowrishankar, M. D. McGehee, X. Li, J. Wang, S. E. Rankin, *Nano Letters* **2006**, *6*, 2567–2570.
- [77] E. M. Freer, L. E. Krupp, W. D. Hinsberg, P. M. Rice, J. L. Hedrick, J. N. Cha, R. D. Miller, H. C. Kim, *Nano Letters* **2005**, *5*, 2014–2018.
- [78] A. Goux, M. Etienne, E. Aubert, C. Lecomte, J. Ghanbaja, A. Walcarius, *Chemistry of Materials* **2009**, *21*, 731–741.
- [79] A. Walcarius, E. Sibottier, M. Etienne, J. Ghanbaja, *Nature Materials* **2007**, *6*, 602–608.
- [80] E. K. Richman, T. Brezesinski, S. H. Tolbert, *Nature Materials* **2008**, *7*, 712–717.
- [81] G. Kickelbick, *Small* **2005**, *1*, 168–170.
- [82] J. Fan, S. W. Boettcher, C. K. Tsung, Q. Shi, M. Schierhorn, G. D. Stucky, *Chemistry of Materials* **2008**, *20*, 909–921.
- [83] G. E. Thompson, G. C. Wood, *Nature* **1981**, *290*, 230–232.

Bibliography

- [84] K. Nielsch, J. Choi, K. Schwirn, R. B. Wehrspohn, U. Gösele, *Nano Letters* **2002**, *2*, 677–680.
- [85] T. Iijima, S. Kato, R. Ikeda, S. Ohki, G. Kido, M. Tansho, T. Shimizu, *Chemistry Letters* **2005**, *34*, 1286–1287.
- [86] Y. Zhang, L. Zhou, D. Li, N. Xue, X. Xu, J. Li, *Chemical Physics Letters* **2003**, *376*, 493–497.
- [87] H. Y. Chen, F. Z. Zhang, S. S. Fu, X. Duan, *Advanced Materials* **2006**, *18*, 3089–3093.
- [88] K. Tang, J. Yu, Y. Zhao, Y. Liu, X. Wang, R. Xu, *Journal of Materials Chemistry* **2006**, *16*, 1741–1745.
- [89] C.-N. Wu, K.-J. Chao, T.-G. Tsai, Y.-H. Chiou, H.-C. Shih, *Advanced Materials* **1996**, *8*, 1008–1012.
- [90] Z. Yang, Z. Niu, X. Cao, Z. Yang, Y. Lu, Z. Hu, C. C. Han, *Angewandte Chemie International Edition* **2003**, *42*, 4201–4203.
- [91] Q. Lu, F. Gao, S. Komarneni, T. E. Mallouk, *Journal of the American Chemical Society* **2004**, *126*, 8650–8651.
- [92] D. Wang, R. Kou, Z. Yang, J. He, Z. Yang, Y. Lu, *Chemical Communications* **2005**, 166–167.
- [93] B. Yao, D. Fleming, M. A. Morris, S. E. Lawrence, *Chemistry of Materials* **2004**, *16*, 4851–4855.
- [94] K. Jin, B. Yao, N. Wang, *Chemical Physics Letters* **2005**, *409*, 172–176.
- [95] Y. Wu, G. Cheng, K. Katsov, S. W. Sides, J. Wang, J. Tang, G. H. Fredrickson, M. Moskovits, G. D. Stucky, *Nature Materials* **2004**, *3*, 816–822.

-
- [96] A. Yamaguchi, F. Uejo, T. Yoda, T. Uchida, Y. Tanamura, T. Yamashita, N. Teramae, *Nature Materials* **2004**, *3*, 337–341.
- [97] A. Y. Ku, S. T. Taylor, S. M. Loureiro, *Journal of the American Chemical Society* **2005**, *127*, 6934–6935.
- [98] A. Y. Ku, S. T. Taylor, W. J. Heward, L. Denault, S. M. Loureiro, *Microporous and Mesoporous Materials* **2006**, *88*, 214–219.
- [99] S. Yoo, D. M. Ford, D. F. Shantz, *Langmuir* **2006**, *22*, 1839–1845.
- [100] B. Platschek, N. Petkov, T. Bein, *Angewandte Chemie International Edition* **2006**, *45*, 1134–1138.
- [101] B. Platschek, R. Koehn, M. Doeblinger, T. Bein, *Langmuir* **2008**, *24*, 5018–5023.
- [102] B. Platschek, R. Köhn, M. Döblinger, T. Bein, *ChemPhysChem* **2008**, *9*, 2059–2067.
- [103] B. Platschek, N. Petkov, D. Himsl, S. Zimdars, Z. Li, R. Köhn, T. Bein, *Journal of the American Chemical Society* **2008**, *130*, 17362–17371.
- [104] K. J. Lee, S. H. Min, J. Jang, *Small* **2008**, *4*, 1945–1949.
- [105] F. Kleitz, F. Marlow, G. D. Stucky, F. Schuth, *Chemistry of Materials* **2001**, *13*, 3587–3595.
- [106] F. Marlow, I. Leike, C. Weidenthaler, C. W. Lehmann, U. Wilczok, *Advanced Materials* **2001**, *13*, 307–310.
- [107] A. Keilbach, M. Döblinger, R. Köhn, H. Amenitsch, T. Bein, *Chemistry-a European Journal* **2009**, *15*, 6645–6650.
- [108] H. Masuda, K. Fukuda, *Science* **1995**, *268*, 1466–1468.

- [109] Y. Wu, T. Livneh, Y. X. Zhang, G. Cheng, J. Wang, J. Tang, M. Moskovits, G. D. Stucky, *Nano Letters* **2004**, *4*, 2337–2342.
- [110] P. Lai, M. Z. Hu, D. Shi, D. Blom, *Chemical Communications* **2008**, 1338–1340.
- [111] V. N. Urade, L. Bollmann, J. D. Kowalski, M. P. Tate, H. W. Hillhouse, *Langmuir* **2007**, *23*, 4268–4278.
- [112] J. Jang, B. Lim, *Angewandte Chemie International Edition* **2003**, *42*, 5600–5603.
- [113] S. Tanaka, N. Nishiyama, Y. Oku, Y. Egashira, K. Ueyama, *Journal of the American Chemical Society* **2004**, *126*, 4854–4858.
- [114] L. Mercier, T. J. Pinnavaia, *Chemistry of Materials* **1999**, *12*, 188–196.
- [115] C. E. Fowler, S. L. Burkett, S. Mann, *Chemical Communications* **1997**, 1769–1770.
- [116] L. Mühlstein, M. Riederer, B. Platschek, T. Bein, *Journal of Materials Chemistry* **2009**, 9195–9203.
- [117] S. Inagaki, S. Guan, Y. Fukushima, T. Ohsuna, O. Terasaki, *Journal of the American Chemical Society* **1999**, *121*, 9611–9614.
- [118] B. J. Melde, B. T. Holland, C. F. Blanford, A. Stein, *Chemistry of Materials* **1999**, *11*, 3302–3308.
- [119] T. Asefa, M. J. MacLachlan, N. Coombs, G. A. Ozin, *Nature* **1999**, *402*, 867–871.
- [120] S. Inagaki, S. Guan, T. Ohsuna, O. Terasaki, *Nature* **2002**, *416*, 304–307.
- [121] Y. Meng, D. Gu, F. Zhang, Y. Shi, L. Cheng, D. Feng, Z. Wu, Z. Chen, Y. Wan, A. Stein, D. Zhao, *Chem. Mater.* **2006**, *18*, 4447–4464.

- [122] C. Liang, Z. Li, S. Dai, *Angewandte Chemie International Edition* **2008**, *47*, 3696–3717.
- [123] C.-G. Wu, T. Bein, *Science* **1994**, *266*, 1013–15.
- [124] R. Ryoo, S. H. Joo, S. Jun, *Journal of Physical Chemistry B* **1999**, *103*, 7743–7746.
- [125] J. Lee, S. Yoon, T. Hyeon, S. M. Oh, K. B. Kim, *Chemical Communications* **1999**, 2177–2178.
- [126] S. Jun, S. H. Joo, R. Ryoo, M. Kruk, M. Jaroniec, Z. Liu, T. Ohsuna, O. Terasaki, *Journal of the American Chemical Society* **2000**, *122*, 10712–10713.
- [127] H. Chang, S. H. Joo, C. Pak, *Journal of Materials Chemistry* **2007**, *17*, 3078–3088.
- [128] I. Moriguchi, A. Ozono, K. Mikuriya, Y. Teraoka, S. Kagawa, M. Kodama, *Chemistry Letters* **1999**, 1171–1172.
- [129] A. T. Rodriguez, M. Chen, Z. Chen, C. J. Brinker, H. Fan, *Journal of the American Chemical Society* **2006**, *128*, 9276–9277.
- [130] M. Zheng, J. Cao, X. Ke, G. Ji, Y. Chen, K. Shen, J. Tao, *Carbon* **2007**, *45*, 1111–1113.
- [131] M. Steinhart, C. Liang, G. W. Lynn, U. Gosele, S. Dai, *Chemistry of Materials* **2007**, *19*, 0897-4756, 2383–2385.
- [132] K. Wang, P. Birjukovs, D. Erts, R. Phelan, M. A. Morris, H. Zhou, J. D. Holmes, *Journal of Materials Chemistry* **2009**, *19*, 1331–1338.
- [133] K. Wang, W. Zhang, R. Phelan, M. A. Morris, J. D. Holmes, *Journal of the American Chemical Society* **2007**, *129*, 13388–13389.
- [134] M. Zheng, G. Ji, Y. Wang, J. Cao, S. Feng, L. Liao, Q. Du, L. Zhang, Z. Ling, J. Liu, T. Yu, J. Cao, J. Tao, *Chemical Communications* **2009**, 5033–5035.

- [135] D. J. Cott, N. Petkov, M. A. Morris, B. Platschek, T. Bein, J. D. Holmes, *Journal of the American Chemical Society* **2006**, *128*, 3920–3921.
- [136] A. Keilbach, J. Moses, R. Köhn, M. Döblinger, T. Bein, *submitted*.
- [137] R. Ryoo, C. H. Ko, M. Kruk, V. Antochshuk, M. Jaroniec, *The Journal of Physical Chemistry B* **2000**, *104*, 11465–11471.
- [138] N. Petkov, B. Platschek, M. A. Morris, J. D. Holmes, T. Bein, *Chemistry of Materials* **2007**, *19*, 1376–1381.
- [139] Y. Sakamoto, A. Fukuoka, T. Higuchi, N. Shimomura, S. Inagaki, M. Ichikawa, *Journal of Physical Chemistry B* **2004**, *108*, 853–858.
- [140] K. M. Ryan, D. Erts, H. Olin, M. A. Morris, J. D. Holmes, *Journal of the American Chemical Society* **2003**, *125*, Times Cited: 54, 6284–6288.
- [141] T. Yamashita, S. Kodama, M. Ohto, E. Nakayama, S. Hasegawa, N. Takayanagi, T. Kemmei, A. Yamaguchi, N. Teramae, Y. Saito, *Analytical Sciences* **2006**, *22*, 1495–1500.
- [142] A. Yamaguchi, J. Watanabe, M. M. Mahmoud, R. Fujiwara, K. Morita, T. Yamashita, Y. Amino, Y. Chen, L. Radhakrishnan, N. Teramae, *Analytica Chimica Acta* **2006**, *556*, 157–163.
- [143] F. Hofmeister, *Arch. Exp. Pathol. Pharmacol.* **1888**, *24*, 247.
- [144] A. Yamaguchi, Y. Amino, K. Shima, S. Suzuki, T. Yamashita, N. Teramae, *The Journal of Physical Chemistry B* **2006**, *110*, doi: 10.1021/jp0564086, 3910–3916.
- [145] V. Antochshuk, M. Jaroniec, *Chemistry of Materials* **2000**, *12*, 2496–2501.
- [146] A. Yamaguchi, T. Yoda, S. Suzuki, K. Morita, N. Teramae, *Analytical Sciences* **2006**, *22*, 1501–1507.

-
- [147] V. Cauda, B. Onida, B. Platschek, L. Mühlstein, T. Bein, *Journal of Materials Chemistry* **2008**, *18*, 10.1039/b805395b, 5888–5899.
- [148] V. Cauda, L. Mühlstein, B. Onida, T. Bein, *Microporous and Mesoporous Materials* **2009**, *118*, doi: DOI: 10.1016/j.micromeso.2008.09.022, 435–442.
- [149] M. Hernández-Vélez, *Thin Solid Films* **2006**, *495*, 51–63.
- [150] V. Schmidt, J. V. Wittemann, S. Senz, U. Gösele, *Advanced Materials* **2009**, *21*, 2681–2702.
- [151] D. Appell, *Nature* **2002**, *419*, 553–555.
- [152] R. Agarwal, C. Lieber, *Applied Physics A: Materials Science & Processing* **2006**, *85*, 209–215.
- [153] A. Singh, A. Ghosh, *The Journal of Physical Chemistry C* **2008**, *112*, 3460–3463.
- [154] S. Y. Ryu, J. Xiao, W. I. Park, K. S. Son, Y. Y. Huang, U. Paik, J. A. Rogers, *Nano Letters* **2009**, *9*, 3214–3219.
- [155] R. S. Wagner, W. C. Ellis, *Applied Physics Letters* **1964**, *4*, 89–90.
- [156] M. Frimmer, MA thesis, Technische Universität München, **2007**.
- [157] Y. Xiang, L. Cao, J. Arbiol, M. L. Brongersma, A. F. i Morral, *Applied Physics Letters* **2009**, *94*, 163101.
- [158] Y. Wang, V. Schmidt, S. Senz, U. Gösele, *Nature Nanotechnology* **2006**, *1*, 186–189.
- [159] D. P. Yu, Z. G. Bai, Y. Ding, Q. L. Hang, H. Z. Zhang, J. J. Wang, Y. H. Zou, W. Qian, G. C. Xiong, H. T. Zhou, S. Q. Feng, *Appl. Phys. Lett.* **1998**, *72*, 3458–3460.

- [160] Y. Xiang, L. Cao, S. Conesa-Boj, S. Estrade, J. Arbiol, F. Peiro, M. Heiss, I Zardo, J. R. Morante, M. L. Brongersma, A. F. i Morral, *Nanotechnology* **2009**, *20*, 245608.
- [161] X. Duan, C. M. Lieber, *Advanced Materials* **2000**, *12*, 298–302.
- [162] J. F. Dayen, A. Rumyantseva, C. Ciornei, T. L. Wade, J. E. Wegrowe, D. Pribat, C. S. Cojocaru, *Applied Physics Letters* **2007**, *90*.
- [163] Y. Xiang, A. Keilbach, L. Moreno Codinachs, K. Nielsch, G. Abstreiter, A. Fontcuberta i Morral, T. Bein, *Nano Letters* **2010**, *10*, 1341–1346.
- [164] Z. W. Pan, Z. R. Dai, Z. L. Wang, *Science* **2001**, *291*, 1947–1949.
- [165] Y. Liu, C. Zheng, W. Wang, C. Yin, G. Wang, *Advanced Materials* **2001**, *13*, 1883–1887.
- [166] W. S. Shi, H. Y. Peng, Y. F. Zheng, N. Wang, N. G. Shang, Z. W. Pan, C. S. Lee, S. T. Lee, *Advanced Materials* **2000**, *12*, 1343–1345.
- [167] N. Petkov, N. Stock, T. Bein, *Journal of Physical Chemistry B* **2005**, *109*, 10737–10743.
- [168] S. J. Limmer, G. Z. Cao, *Advanced Materials* **2003**, *15*, 427–431.
- [169] S. J. Limmer, T. P. Chou, G. Z. Cao, *Journal of Materials Science* **2004**, *39*, 895–901.
- [170] Z. B. Zhang, D. Gekhtman, M. S. Dresselhaus, J. Y. Ying, *Chemistry of Materials* **1999**, *11*, 1659–1665.
- [171] J. Xu, N. Petkov, X. Wu, D. Iacopino, A. J. Quinn, G. Redmond, T. Bein, M. A. Morris, J. D. Holmes **2007**, *8*, 235–240.
- [172] X. Lu, C. Wang, Y. Wei, *Small* **2009**, *5*, 2349–2370.

-
- [173] J. Weber, R. Singhal, S. Zekri, A. Kumar, *International Materials Reviews* **2008**, *53*, 235–255.
- [174] G. Rubio-Bollinger, S. R. Bahn, N. Agraït, K. W. Jacobsen, S. Vieira, *Phys. Rev. Lett.* **2001**, *87*, 026101.
- [175] P. Buffat, J.-P. Borel, *Phys. Rev. A* **1976**, *13*, 2287–2298.
- [176] Y. Wu, P. Yang, *Advanced Materials* **2001**, *13*, 520–523.
- [177] Y. Cui, C. M. Lieber, *Science* **2001**, *291*, 851–853.
- [178] B. Smarsly, M. Antonietti, T. Wolff, *Journal of Chemical Physics* **2002**, *116*, 2618–2627.
- [179] B. Smarsly, A. Gibaud, W. Ruland, D. Sturmayr, C. J. Brinker, *Langmuir* **2005**, *21*, 3858–3866.
- [180] B. Smarsly, M. Groenewolt, M. Antonietti, *Progress in Colloid & Polymer Science* **2005**, *130*, 105–113.
- [181] B. Smarsly, W. Ruland, *Journal of Applied Crystallography* **2005**, *38*, 78–86.
- [182] R. Hilfiker, H. F. Eicke, W. Sager, C. Steeb, U. Hofmeier, R. Gehrke, *Berichte der Bunsen-Gesellschaft* **1990**, *94*, 677–83.
- [183] A. Shioi, M. Harada, M. Tanabe, *Langmuir* **1996**, *12*, 3201–3205.
- [184] B. Deme, M. Dubois, T. Gulik-Krzywicki, T. Zemb, *Langmuir* **2002**, *18*, 997–1004.
- [185] H. Schnablegger, Y. Singh, *A Practical Guide to SAXS*, Anton Paar GmbH, **2006**.

- [186] J. Goldstein, D. E. Newbury, D. C. Joy, P. Echlin, C. E. Lyman, E. Lifshin, L. Sawyer, *Scanning electron microscopy and x-ray microanalysis*, Springer Netherlands, **2003**.
- [187] P. J. Goodhew, J. Humphreys, R. Beanland, *Electron Microscopy and Analysis*, Taylor & Francis, London, 3rd, **2001**.
- [188] <http://barrett-group.mcgill.ca/teaching/nanotechnology/nano02.htm>
[last accessed on 21.04.2010].
- [189] D. B. Williams, B. C. Carter, *Transmission electron microscopy*, Plenum publishing Corporation, **1996**.
- [190] J. I. Goldstein, D. J. Newbury, C. Lyman, P. Echlin, E. Lifshin, L. Sawyer, J. Michael, *Scanning electron microscopy and x-ray analysis*, Kluwer Academic/Plenum Publishers, **2003**.
- [191] J. Rouquerol, D. Avnir, C. W. Fairbridge, D. H. Everett, J. M. Haynes, N. Pernicone, J. D. F. Ramsay, K. S. W. Sing, K. K. Unger, *Pure and Applied Chemistry* **1994**, *66*, 1739–1758.
- [192] J. B. Condon, *Surface Area and Porosity Determinations by Physisorption*, Elsevier Science & Technology, **2006**.
- [193] M. Kruk, M. Jaroniec, *Chemistry of Materials* **2001**, *13*, 3169–3183.
- [194] S. Brunauer, P. H. Emmett, E. Teller, *Journal of the American Chemical Society* **1938**, *60*, 309–319.
- [195] S. Lowell, J. E. Shields, M. A. Thomas, M. Thommes, *Characterization of Porous Solids and Powders: Surface Area, Pore Size and Density*, Kluwer Academic Publishers, **2004**.
- [196] M. Kruk, M. Jaroniec, *Chemistry of Materials* **2000**, *12*, 222–230.

-
- [197] M. Hesse, H. Meier, B. Zeeh, *Spektroskopische Methoden in der organischen Chemie*, Georg Thieme Verlag, Stuttgart, Germany, 6th, **2002**.
- [198] H. Eckert, *Encyclopedia of materials characterization - Surfaces, Interfaces, Thin Films* (Ed.: L. E. Fitzpatrick), Butterworth-Heinemann Ltd, **1992**.
- [199] G. Cao, D. Liu, *Advances in Colloid and Interface Science* **2008**, *136*, 45–64.
- [200] D. K. Ferry, *Science* **2008**, *319*, 579–580.
- [201] W. Lu, C. M. Lieber, *Journal of Physics D: Applied Physics* **2006**, *39*, R387–R406.
- [202] C. M. Lieber, Z. L. Wang, *MRS Bulletin* **2007**, *32*, 99–104.
- [203] Y. Wu, H. Yan, M. Huang, B. Messer, J. H. Song, P. Yang, *Chemistry - A European Journal* **2002**, *8*, 1260–1268.
- [204] M. Nath, B. A. Parkinson, *Advanced Materials* **2006**, *18*, 2504.
- [205] T. L. Wade, X. Hoffer, A. D. Mohammed, J.-F. Dayen, D. Pribat, J.-E. Wegrowe, *Nanotechnology* **2007**, *18*, 125201.
- [206] G. Schmid, *Journal of Materials Chemistry* **2002**, *12*, 1231–1238.
- [207] H. Shang, G. Cao in *Springer Handbook of Nanotechnology (2nd Edition)*, **2007**, pp. 161–178.
- [208] F. Chen, A. H. Kitai, *Journal of Nanoscience and Nanotechnology* **2008**, *8*, 4488–4493.
- [209] A. Azarian, A. Iraj Zad, A. Dolati, S. M. Mahdavi, *Thin Solid Films* **2009**, *517*, 1736–1739.
- [210] Y. Xiang, W. Lee, K. Nielsch, G. Abstreiter, A. F. i. Morral, *Physica Status Solidi RRL Rapid Research Letters* **2008**, *2*, 59–61.

- [211] T. Gao, G. Meng, Y. Wang, S. Sun, L. Zhang, *Journal of Physics: Condensed Matter* **2002**, *14*, 355–363.
- [212] G. E. Thompson, R. C. Furneaux, G. C. Wood, J. A. Richardson, J. S. Goode, *Nature* **1978**, *272*, 433–435.
- [213] R. Krishnan, C. Thompson, *Advanced Materials* **2007**, *19*, 988–992.
- [214] K. Nielsch, F. Müller, A.-P. Li, U. Gösele, *Advanced Materials* **2000**, *12*, 582–586.
- [215] H. Zhang, Z. Chen, T. Li, K. Saito, *Journal of Nanoscience and Nanotechnology* **2005**, *5*, 1745–1748.
- [216] C. S. Cojocaru, J. M. Padovani, T. Wade, C. Mandoli, G. Jaskierowicz, J. E. Wegrowe, A. Fontcuberta i Morral, D. Pribat, *Nano Letters* **2005**, *5*, 675–680.
- [217] Y. Cui, Q. Wei, H. Park, C. M. Lieber, *Science* **2001**, *293*, 1289–1292.
- [218] F. Patolsky, G. Zheng, C. M. Lieber, *Analytical Chemistry* **2006**, *78*, doi: 10.1021/ac069419j, 4260–4269.
- [219] N.-W. Liu, C.-Y. Liu, H.-H. Wang, C.-F. Hsu, M.-Y. Lai, T.-H. Chuang, Y.-L. Wang, *Advanced Materials* **2008**, *20*, 2547–2551.
- [220] R. C. Furneaux, W. R. Rigby, A. P. Davidson, *Nature* **1989**, *337*, 147–9.
- [221] D. AlMawlawi, N. Coombs, M. Moskovits, *Journal of Applied Physics* **1991**, *70*, 4421–4425.
- [222] N. J. Gerein, J. A. Haber, *J. Phys. Chem. B* **2005**, *109*, 17372–17385.
- [223] Q. Wang, D. F. Shantz, *Journal of Solid State Chemistry* **2008**, *181*, 1659–1669.
- [224] B. Tian, T. J. Kempa, C. M. Lieber, *Chemical Society Reviews* **2009**, *38*, 16–24.

- [225] C. K. Chan, H. Peng, G. Liu, K. McIlwrath, X. F. Zhang, R. A. Huggins, Y. Cui, *Nature Nano* **2008**, *3*, 31–35.
- [226] X. Chen, R. Ji, M. Steinhart, A. Milenin, K. Nielsch, U. Gosele, *Chem. Mater.* **2007**, *19*, 3–5.
- [227] Q. Wang, G. Wang, B. Xu, J. Jie, X. Han, G. Li, Q. Li, J. G. Hou, *Materials Letters* **2005**, *59*, 1378–1382.
- [228] W.-L. Wang, C.-C. Wan, Y.-Y. Wang, *Journal of Physical Chemistry B* **2006**, *110*, 12974–12980.
- [229] P. Birjukovs, N. Petkov, J. Xu, J. Svirks, J. J. Boland, J. D. Holmes, D. Erts, *Journal of Physical Chemistry C* **2008**, *112*, 19680–19685.
- [230] J. Bachmann, J. Jing, M. Knez, S. Barth, H. Shen, S. Mathur, U. Gösele, K. Nielsch, *Journal of the American Chemical Society* **2007**, *129*, 9554–9555.
- [231] T. W. Cornelius, J. Broetz, N. Chtanko, D. Dobrev, G. Mieke, R. Neumann, M. E. T. Molaes, *Nanotechnology* **2005**, *16*, –246.
- [232] M. E. T. Molaes, V. Buschmann, D. Dobrev, R. Newmann, R. Scholz, I. U. Schuchert, J. Vetter, *Advanced Materials* **2001**, *13*, 62–65.
- [233] C. Lepiller, P. Cowache, J. F. Guillemoles, N. Gibson, E. Özsan, D. Lincot, *Thin Solid Films* **2000**, *361-362*, 118–122.
- [234] A. Zhao, L. Zhang, Y. Pang, C. Ye, *Applied Physics A: Materials Science & Processing* **2005**, *80*, 1725–1728.
- [235] W. Lee, R. Ji, C. A. Ross, U. Gosele, K. Nielsch, *Small* **2006**, *2*, 978–982.
- [236] A. Gabashvili, D. D. Medina, A. Gedanken, Y. Mastai, *The Journal of Physical Chemistry B* **2007**, *111*, 11105–11110.

- [237] I. I. Slowing, B. . G. Trewyn, S. Giri, V. . S. Y. Lin, *Advanced Functional Materials* **2007**, *17*, 1225–1236.
- [238] G. Xomeritakis, N. G. Liu, Z. Chen, Y. B. Jiang, R. Kohn, P. E. Johnson, C. Y. Tsai, P. B. Shah, S. Khalil, S. Singh, C. J. Brinker, *Journal of Membrane Science* **2007**, *287*, 157–161.
- [239] Y. Yang, A. Sayari, *Chemistry of Materials* **2007**, *19*, 4117–4119.
- [240] E. L. Crepaldi, G. J. d. A. A. Soler-Illia, A. Bouchara, D. Grosso, D. Durand, C. Sanchez, *Angewandte Chemie* **2003**, *115*, 361–365.
- [241] G. J. A. A. Soler-Illia, E. L. Crepaldi, D. Grosso, D. Durand, C. Sanchez, *Chemical Communications* **2002**, 2298–2299.
- [242] T. Brezesinski, A. Fischer, K.-i. Iimura, C. Sanchez, D. Grosso, M. Antonietti, B. M. Smarsly, *Advanced Functional Materials* **2006**, *16*, 1433–1440.
- [243] V. Antochshuk, M. Jaroniec, *Physical Chemistry Chemical Physics* **1999**, 2373–2374.
- [244] Y. Li, A. Keilbach, M. Kienle, Y. Goto, S. Inagaki, P. Knochel, T. Bein, *in preparation*.
- [245] K. Okamoto, Y. Goto, S. Inagaki, *Journal of Materials Chemistry* **2005**, *15*, 4136–4140.
- [246] M. Ohashi, M. P. Kapoor, S. Inagaki, *Chemical Communications* **2008**, 841–843.
- [247] M. C. Burleigh, M. A. Markowitz, S. Jayasundera, M. S. Spector, C. W. Thomas, B. P. Gaber, *The Journal of Physical Chemistry B* **2003**, *107*, 12628–12634.

- [248] J. Schuster, A. Keilbach, R. Köhn, M. Döblinger, H. Amenitsch, T. Bein, *in preparation*.

Appendices

List of abbreviations

AAM	Anodic alumina membrane
AAO	Anodic aluminum oxide
ac	Alternating current
BET	Brunauer-Emmet-Teller
Brij 56	Polyoxyethylene (10) cetyl ether
CMC	Critical micelle concentration
CVD	Chemical vapor deposition
CTAB	Hexadecyltrimethylammonium bromide
dc	direct current
e.g.	Exempli gratia
EDX	Energy-dispersive X-ray spectroscopy
EISA	Evaporation induced self assembly
FIB	Focused ion beam
FTO	Fluorine-doped tin oxide
GISAXS	Grazing incidence X-ray diffraction
hex.	Hexagonal
IR	Infrared
ITO	Indium tin oxide, tin-doped indium oxide
LMU	Ludwig-Maximilian-Universität
MCM	Mobil Composition of Matter
OMC	Ordered mesoporous carbons
PAA	Porous anodic alumina
Pluronic P123	Poly(ethylene oxide) ₂₀ - <i>block</i> -poly(propylene oxide) ₇₀ - <i>block</i> -poly(ethylene oxide) ₂₀
r.t.	Room temperature
SAED	Selected-area electron diffraction
SAXS	Small angle X-ray scattering
SDA	Structure directing agent
SEM	Scanning electron microscopy
STEM	Scanning transmission electron microscopy
TEM	Transmission Electron Microscopy
TEOS	Tetraethylorthosilicate
THF	Tetrahydrofuran
TMS-Cl	Trimethylchlorosilane
UV	Ultraviolet
VLS	Vapor-liquid-solid growth

Curriculum vitae

Persönliche Daten:

Name: *Andreas Keilbach*
Geburtsdatum: *9. Februar 1978*
Geburtsort: *München*
Nationalität: *Deutsch*

Ausbildung:

10.2005 – heute *Promotion an der LMU München, AK Prof. Bein
“Oriented Nanochannels for Nanowire Synthesis”*
03.2005 – 09.2005 *Diplomarbeit an der LMU München, AK Prof. Bein
“Synthesis of Copper Nanowires within Mesoporous Host Materials”*
11.1999 – 09.2005 *Chemiestudium an der LMU München*
1988 – 1998 *Thomas-Mann-Gymnasium, München*
1984 – 1988 *Grundschule an der Sambergerstrasse, München*

Zusatzqualifikationen:

Sprachen *Deutsch (Muttersprache)
Englisch (fließend)
Chinesisch (Mandarin, Anfänger)*
EDV-Kenntnisse *Betriebssysteme: Windows, Linux
Microsoft Office, Adobe Photoshop und Illustrator*

List of publications and presentations

Publications

1. M. Westerhausen, M. W. Oßberger, A. Keilbach, C. Gückel, H. Piotrowski, M. Suter, H. Nöth, "Synthese, Eigenschaften und Molekülstrukturen der 2, 3, 4, 5- Tetraethylphospholide der Alkalimetalle Natrium, Kalium, Rubidium und Caesium sowie die Metathesereaktion des Kalium-Derivates mit Zinn(II)-chlorid und Gallium(III)-chlorid"; *Zeitschrift für anorganische und allgemeine Chemie*, **2003**, 629, 2398.
2. A. Keilbach, M. Döblinger, R. Köhn, H. Amenitsch, T. Bein, "Periodic Mesoporous Organosilica in Confined Environments"; *Chemistry – a European Journal* **2009**, 15, 6645.
3. J. Schuster, R. Köhn, A. Keilbach, M. Döblinger, H. Amenitsch, T. Bein, "Two-Dimensional-Hexagonal Periodic Mesoporous Polymer Resin Thin Films by Soft Templating"; *Chemistry of Materials* **2009**, 21, 5754.
4. A. Keilbach, M. Döblinger, R. Köhn, H. Amenitsch, T. Bein, "Periodic mesoporous organosilicas in confined environments"; *Elettra Highlights 08-09*, **2009**, 38.
5. Y. Xiang, A. Keilbach, L. M. Cordinachs, K. Nielsch, G. Abstreiter, A. Fontcuberta i Morral, T. Bein, "Multiple nanowire species synthesized on a single chip by selectively addressable horizontal nanochannels"; *Nano Letters* **2010**, 10, 1341.
6. A. Keilbach, J. Moses, R. Köhn, M. Döblinger, T. Bein, "Synthesis of Copper and Silver Nanowires by Electrodeposition within Columnar Silica/Alumina Composites"; *Chemistry of Materials* *submitted*.
7. B. Platschek, A. Keilbach, T. Bein, "Mesoporous structures in confined environments"; *submitted*.
8. J. Schuster, A. Keilbach, R. Köhn, M. Döblinger, H. Amenitsch, T. Bein, "Cubic and Hexagonal Mesoporous Carbon in Pores of Anodic Alumina Membranes"; *in preparation*.
9. Y. Li, A. Keilbach, M. Kienle, Y. Goto, S. Inagaki, P. Knochel, T. Bein, "Biphenylene bridged periodic mesoporous organosilica in confined environments"; *in preparation*.

Oral presentations

1. A. Keilbach, T. Bein, "Porous Anodic Alumina"; *TU München*, 12.07.2007.
2. R. Köhn, A. Keilbach, A. Zürner, B. Platschek, M. Döblinger, T. Bein, "Silica mesostructure formation and phase transformation in the confined space of anodic alumina membranes"; *4th FEZA conference*, Paris (France), 02.-06.09.2008.

Poster presentations

1. A. Keilbach, R. Köhn, B. Platschek, T. Bein, "Synthesis of Copper Nanowires within Oriented Host Materials"; 18. *Deutsche Zeolith-Tagung*, Hannover, 01.-03.03.2006.
2. A. Keilbach, R. Köhn, H. Vieyra, S. Hochwarter, H.-A. Krug von Nidda, A. Loidl, T. Bein, "Synthesis of Magnetic Nanowires in Low-Dimensional Alumina Templates"; CeNS Workshop, Venice (Italy), 25.-29.09.2006.
3. A. Keilbach, S. Braunmüller, R. Köhn, T. Bein, "Periodic Mesoporous Organosilicates Confined within an Anodic Alumina Membrane"; *CeNS Winter School*, Burg Mauterndorf (Austria), 12.-16.02.2007.
4. A. Keilbach, S. Braunmüller, R. Köhn, T. Bein, "Synthesis of Periodic Mesoporous Organosilicas within Anodic Alumina Pores"; 19. *Deutsche Zeolith-Tagung*, Leipzig, 07.-09.03.2007.
5. A. Keilbach, M. Döblinger, R. Köhn, T. Bein, "2D SAXS on PMO Materials confined in Anodic Alumina Membranes"; 2nd GISAXS Workshop, HASYLAB, Hamburg, 09.-11.05.2007.
6. A. Keilbach, R. Köhn, T. Bein, "Synthesis of Periodic Mesoporous Organosilicas within Anodic Alumina Pores"; 4th FEZA conference, Paris (France), 02.-06.09.2008.
7. J. Schuster, A. Keilbach, R. Köhn, T. Bein, "Soft-templating method for mesoporous carbon thin films"; 4th FEZA conference, Paris (France), 02.-06.09.2008.
8. A. Keilbach, J. Schuster, B. Platschek, N. Petkov, T. Bein, "TP B8 Ultradünne funktionale Nanodrähte für elektronische und optische Anwendungen"; *Nanoman Summarizing Workshop*, Venice (Italy), 16.-19.09.2009.
9. J. Schuster, A. Keilbach, R. Köhn, T. Bein, "Cubic and Hexagonal Mesoporous Carbon within the Pores of Anodic Alumina Membranes"; 22. *Deutsche Zeolith-Tagung*, München, 03.-05.03.2010.
10. Y. Li, A. Keilbach, S. Inagaki, T. Bein, "Optically active biphenylene bridged periodic mesoporous organosilica in confined environments"; 22. *Deutsche Zeolith-Tagung*, München, 03.-05.03.2010.
11. A. Keilbach, J. Schuster, Y. Li, M. Döblinger, T. Bein, "Periodic mesoporous organosilicas and carbons in confined spaces"; 16th IZC & 7th IMMS, Sorrento (Italy), 04.-09.07.2010.

